JOURNAL OF PETROLOGY | VOLUME 54 | NUMBER 11 | PAGES 2301–2338 | 2013 | doi:10.1093/petrology/egt048

Element Partitioning between Immiscible Carbonatite and Silicate Melts for Dry and H_2O-bearing Systems at 1–3 GPa

LUKAS H. J. MARTIN[1]*, MAX W. SCHMIDT[1], HANNES B. MATTSSON[1] AND DETLEF GUENTHER[2]

[1]DEPARTMENT OF EARTH SCIENCES, INSTITUTE OF GEOCHEMISTRY AND PETROLOGY, ETH, 8092 ZURICH, SWITZERLAND

[2]DEPARTMENT OF CHEMISTRY AND APPLIED BIOSCIENCES, LABORATORY OF INORGANIC CHEMISTRY, ETH, 8093 ZURICH, SWITZERLAND

RECEIVED AUGUST 17, 2012; ACCEPTED AUGUST 13, 2013
ADVANCE ACCESS PUBLICATION SEPTEMBER 26, 2013

Carbonatite and silicate rocks occurring within a single magmatic complex may originate through liquid immiscibility. We thus experimentally determined carbonatite/silicate melt partition coefficients ($D^{carbonate\ melt/silicate\ melt}$*, hereafter* D*) for 45 elements to understand their systematics as a function of melt composition and to provide a tool for identifying the possible conjugate nature of silicate and carbonatite magmas. Static and, when necessary, centrifuging piston cylinder experiments were performed at 1–3 GPa, 1150–1260°C such that two well-separated melts resulted. Bulk compositions had* $Na \gg K$, $Na \sim K$, *and* $Na \ll K$*; for the latter we also varied bulk* H_2O *(0–4 wt %) and* SiO_2 *contents. Oxygen fugacities were between iron–wüstite and slightly below hematite–magnetite and were not found to exert significant control on partitioning. Under dry conditions alkali and alkaline earth elements partition into the carbonatite melt, as did Mo and P (*$D^{Mo} > 8$, $D^{P} = 1{\cdot}6$–$3{\cdot}3$*). High field strength elements (HFSE) prefer the silicate melt, most strongly Hf (*$D^{Hf} = 0{\cdot}04$*). The REE have partition coefficients around unity with* $D^{La/Lu} = 1{\cdot}6$–$2{\cdot}3$*. Transition metals have* $D < 1$ *except for Cu and V (*$D^{Cu} \sim 1{\cdot}3$, $D^{V} = 0{\cdot}95$–2*). The small variability of the partition coefficients in all dry experiments can be explained by a comparable width of the miscibility gap, which appears to be flat-topped in our dry bulk compositions. For all carbonatite and silicate melts, Nb/Ta and Zr/Hf fractionate by factors of 1·3–3·0, in most cases much more strongly than in silicate–oxide systems. With the exception of the alkalis, partition coefficients for the* H_2O*-bearing systems are similar to those for the anhydrous ones, but are shifted in favour of the carbonatite melt by up to an order of magnitude. An increase of bulk silica and thus* SiO_2 *in the silicate melt (from 35 to 69 wt %) has a similar effect. Two types of trace element partitioning with changing melt composition can be observed. The magnitude of the partition coefficients increases for the alkalis and alkaline earths with the width of the miscibility gap, whereas partition coefficients for the REE shift by almost two orders of magnitude from partitioning into the silicate melt (*$D^{La} = 0{\cdot}47$*) to strongly partitioning into the carbonatite melt (*$D^{La} = 38$*), whereas* D^{La}/D^{Lu} *varies by only a factor of three. The partitioning behavior can be rationalized as a function of ionic potential (*Z/r*). Alkali and alkaline earth elements follow a trend, the slope of which depends on the K/Na ratio and* H_2O *content. Contrasting the sodic and potassic systems, alkalis have a positive correlation in* D *vs* Z/r *space in the potassic case and Cs to K partition into the silicate melt in the presence of* H_2O*. For the divalent third row transition metals on the one hand and for the tri- and tetravalent REE and HFSE on the other, two trends of negative correlation of* D *vs* Z/r *can be defined. Nevertheless, the highest ionic strength network-modifying cations (V, Nb, Ta, Ti and Mo) do not follow any trend; understanding their behavior would require knowledge of their bonding environment in the carbonatite melt. Strong partitioning of REE into the carbonatite melt (*$D_{REE} = 5{\cdot}8$–$38{\cdot}0$*) occurs only in* H_2O*-rich compositions for which carbonatites unmix from evolved alkaline melts with the conjugate silicate melt being siliceous. We thus speculate that upon hydrous carbonatite crystallization, the*

---

*Corresponding author. E-mail: Lukas.martin@alumni.ethz.ch

consequent saturation in fluids may lead to hydrothermal systems concentrating REE in secondary deposits.

KEY WORDS: *carbonatite; liquid immiscibility; trace element partitioning; ionic potential*

INTRODUCTION

Carbonatites are well known as an economic source for commodities such as the rare earth elements (REE), Nb and U, but the mechanism of trace element enrichment is not well understood. Although more than 500 alleged carbonatite occurrences have been identified on Earth (Woolley & Kjarsgaard, 2008), the petrogenesis of carbonatite magmas remains debated. Three main mechanisms are envisaged for the formation of carbonatite melts: (1) derivation as primary liquids by low-degree partial melting of a carbonate-bearing peridotite or eclogite (Wallace & Green, 1988; Dalton & Wood, 1993; Harmer & Gittins, 1998; Brey *et al.*, 2008; Dasgupta *et al.*, 2009; Hammouda *et al.*, 2009); (2) formation as evolved melts through extensive fractional crystallization from a CO_2-rich silicate parent melt as proposed, for example, for Group II kimberlites (Watkinson & Wyllie, 1971; Nielsen & Veksler, 2002; Ulmer & Sweeney, 2002); (3) separation of a carbonatite from a silicate melt by liquid immiscibility (Lee & Wyllie, 1997; Veksler *et al.*, 1998, 2012; Brooker & Kjarsgaard, 2011).

The intimate association of carbonatites with alkali-rich silicate magmas [e.g. on Brava island, Cape Verde (Mourão *et al.*, 2010), at San Venanzo in the Intra-Apennine magmatic province in Italy (Stoppa & Cundari, 1998), or at Oldoinyo Lengai and Kerimasi, Tanzania (Kjarsgaard *et al.*, 1995; Guzmics *et al.*, 2009, 2012)] led to the suggestion that these carbonatites originated by liquid immiscibility. This hypothesis could be tested based on partition coefficients (D^i) determined in experiments between immiscible silicate and carbonatite melts and compared with suspected conjugate liquids in nature. Such an application of partition coefficients was presented by Veksler *et al.* (2012) for liquid immiscibility at Oldoinyo Lengai and by Martin *et al.* (2012) for the mantle-derived kamafugite–carbonatite suite from central Italy. This study investigates the systematics of element partitioning between immiscible carbonatite and silicate melts to understand what governs the partitioning.

Partition coefficients between coexisting carbonatite and silicate melts were determined in static experiments by Wendlandt & Harrison (1979), Hamilton *et al.* (1989) and Jones *et al.* (1995). The analysis of static experiments can be problematic owing to insufficient physical separation of the carbonatite and silicate melts. Therefore, in the next generation of experiments, immiscible melts were physically separated by centrifugation to avoid cross-contamination (Veksler *et al.*, 1998, 2012). The experiments of Veksler and co-workers utilized a small, internally heated, pressure vessel mounted into a biological centrifuge at pressures ≤0·1 GPa. These are suitable pressures for studying liquid immiscibility in shallow subvolcanic magmatic plumbing systems, such as at Oldoinyo Lengai. However, the presence of xenolithic mantle material in carbonatites, as well as the primitive character of the associated silicate magmas, suggests a deeper, possibly mantle origin for many carbonatites (Stoppa & Cundari, 1998; Rosatelli *et al.*, 2010). With increasing pressure, the solubility of volatiles in silicate melts rises (Brooker *et al.*, 2001; Papale *et al.*, 2006), which should affect the width of the miscibility gap (Brooker, 1998). The width of the carbonatite–silicate melt miscibility gap increases clearly with pressure from 0·1 to 0·8 GPa (Freestone & Hamilton, 1980), and to a lesser extent also to 1·5–2·0 GPa (Brooker, 1998; Brooker & Kjarsgaard, 2011). Comparing the miscibility gap width at 1·0 and 2·5 GPa, Lee & Wyllie (1997) indicated that the gap width decreases in this pressure range. Nevertheless, temperature, pressure, volatile saturation, and melt compositions co-vary in most studies, and bulk compositions are different between studies. It is thus not an easy task to isolate the effect of a single parameter (other than temperature), and the exact variation of the miscibility gap width remains a subject for discussion (e.g. Brooker, 1998; Brooker & Kjarsgaard, 2011). For melts of natural carbonated pelites, the miscibility gap width seems to remain invariant with pressure to 5 GPa (Thomsen & Schmidt, 2008). Above 5 GPa, carbonatite–silicate melt immiscibility appears to vanish within a short pressure interval (Grassi & Schmidt, 2011*b*) and although systematic studies have not been reported, melting experiments on carbonated lithologies document a continuous increase in SiO_2 content with degree of melting (e.g. Brey *et al.*, 2008, 2011; Grassi & Schmidt, 2011*a*, 2011*b*). At the same time, pressure has a profound effect on the stability of alkali and alkaline earth carbonate melts: whereas Na_2CO_3 and K_2CO_3 melt at ambient pressure, alkaline earth carbonates decarbonate at low pressure and melt only at ≥2·7 GPa for calcite (Huang & Wyllie, 1974), >2·2 GPa for dolomite and ≥3·5 GPa for magnesite (Falloon & Green, 1989).

This study investigates the systematics of partition coefficient behaviour for conjugate silicate and carbonatite melts at high pressures (1–3 GPa) for anhydrous and H_2O-bearing systems. We present data for three anhydrous, silica-undersaturated systems: a sodic one, largely after Lee & Wyllie (1997), a potassic one, relevant for the Italian carbonatite–kamafugite suites, and an alkalic system with equal molar amounts of sodium and potassium in the bulk composition. These sets of partition coefficients are complemented by data from a haplogranite–carbonatite system and from an analogue system to Oldoinyo Lengai (Veksler *et al.*, 1998, 2012). We further present data for H_2O-bearing bulk compositions (2–4 wt %) with variable silica contents. Taken together, the chemical variations in the combined datasets allow a deeper understanding of the factors that control element partitioning between carbonatite and silicate melts.

METHODS

Strategy

First, we produced liquid immiscibility between silicate and carbonatite melts in different bulk composition systems in static piston cylinder experiments at 1–3 GPa. Once this was obtained, the compositions of the melts, which typically coexisted with several minerals, were analysed. From this, new starting materials, with compositions representing mixtures of the two immiscible melts, were synthesized and spiked with a trace element mix. The new starting materials were run at pressure–temperature conditions identical to the original experiments for 40–86 h to attain chemical equilibrium. The physical separation of immiscible melts in static experiments on H_2O-bearing bulk compositions was sufficient to analyze the melt compositions by electron microprobe for major elements and by laser ablation inductively coupled plasma mass spectrometry (LA-ICP-MS) for trace elements. The immiscible melts of the anhydrous bulk compositions were insufficiently separated after the static experiments. Therefore, capsules were recovered after static chemical equilibration and reloaded into a single-stage piston cylinder mounted into a centrifuge (Schmidt *et al.*, 2006). The experiment was then continued at the same pressure–temperature conditions but with an additional centrifugal acceleration of 712 *g* applied to gravitationally segregate the two liquids. After centrifugation, the melts were perfectly separated for analysis, with coexisting crystals segregated to the gravitational bottom of the capsule.

Synthesis of the starting materials

Starting materials (Table 1) were mixed from MgO, Al_2O_3, TiO_2, Fe_2O_3, Cr_2O_3, SiO_2 (all dried in a furnace at 800°C), synthetic wollastonite, albite, K-feldspar, and $CaCO_3$, natural dolomite (dried at 400°C), Na_2CO_3, K_2CO_3 and hydroxy-apatite (dried at 220°C), as well as synthetic fayalite and $Al(OH)_3$ (dried at 110°C). A combination of different K-, Na- and Ca-silicates and carbonates was necessary to achieve the desired CO_2 contents in the starting materials. Fe_2O_3 and synthetic fayalite were mixed in appropriate proportions to obtain the desired Fe^{2+}/Fe^{3+} ratios; $Al(OH)_3$ was the principal source of H_2O in the starting materials.

Each mix was ground in an agate mortar with acetone for 20–30 min, dried, and stored in a furnace at 220°C for the anhydrous systems and 110°C for the H_2O-bearing ones. Despite taking the greatest care, absorption of traces of water in the starting material remains inevitable. The addition of hydroxyapatite to the starting materials Mix1-D, KF4, KF7 and Alk added <0·02 wt % H_2O to the sodic and alkalic ($Na \sim K$) systems and $\leq$0·04 wt % H_2O to the potassic system.

Trace elements were added as a pre-prepared spike made from oxide components and solutions (U, Th). The spike consists of Li, Na, K, Rb, Cs, Be, Mg, Ca, Sr, Ba, Al, Sc, Y, La, Sm, Dy, Yb, Lu, Ti, Zr, Hf, V, Nb, Ta, Mo, W, U, Th, Fe, Co, Cr, Zn, Cd, Ga, Si, Ge, Pb, and P. To achieve bulk trace element concentrations of 20–100 ppm, about 5‰ of spike were added.

Dry starting materials

More than 100 experiments were performed during this study to obtain liquid immiscibility for different bulk composition systems. The experiments that resulted in immiscible liquids and allowed measurement of partitioning data are reported in Table 2; other experiments with melt compositions pertinent to this study are given in Table 3. For the anhydrous systems, we investigated three types of silica-undersaturated bulk compositions (Table 1): sodic, potassic and alkalic.

The sodic system

The sodic system (K_2O/Na_2O wt-ratio = 0·03–0·04) is an adaptation of a composition originally investigated by Lee & Wyllie (1997; their Mix#3), initially consisting of 50 wt % primitive magnesian nephelinite from Hawaii (No. 68KEE-1; Clague & Frey, 1982), 25 wt % Na_2CO_3 and 25 wt % dolomite. Lee & Wyllie (1997) obtained olivine coexisting with carbonatite and silicate melts. We thus subtracted this olivine by mass balance to obtain silicate and carbonatite melts only (starting material Mix1-B). In this starting material all iron was added as fayalite. For Mix1-C, Cr_2O_3 was added and Mix1-D contains a molar ratio of $Fe^{3+}/Fe^{tot} = 0{\cdot}28$, resulting in a slightly higher f_{O2}, and 0·45 wt % P_2O_5 added as hydroxy-apatite yielding H_2O contents of $\leq$0·02 wt %. The introduction of Fe^{3+} was intended to test if variable Fe^{2+}/Fe^{3+} ratios have an effect on element partitioning.

The potassic system

The potassic systems (KF4 and KF7) were designed to investigate the ultrapotassic kamafugite–carbonatite suite from the Intra-Apennine Magmatic Province in Italy (Stoppa & Cundari, 1998). Kamafugites are primitive, mantle-derived, silica-undersaturated melts with K_2O/Na_2O wt-ratios >5 and represent extremely potassic alkaline rocks. Details of the experimental procedure to obtain liquid immiscibility at 1·7 GPa and the application of the partition coefficients to the Italian ultrapotassic suite have been presented by Martin *et al.* (2012). Here, the experiments serve to understand the systematics and factors controlling trace element partitioning between conjugate carbonatite and silicate melts. Starting material KF4

Table 1: Starting materials

System:	Sodic			Ultrapotassic		Alkalic	Potassic			Phonolite			Trachyte	Basaltic eclogite			CMASC
Starting material:	Mix1-B	Mix1-C	Mix1-D	KF4	KF7	Alk	KF5	KF6	KF8	ThS1	ThS-2	ThS3B	ThS4	DS-1	DS-2	DS-3	SH-1
Spike*	0·6	0·7	0·6	0·5	0·9	0·8	0·8	0·8	1·7	6·1	0·7	0·9	1·0	0·6	0·9	0·9	1·8
SiO_2	18·9	18·8	17·8	21·9	20·9	17·0	21·1	21·1	21·5	27·0	31·2	29·1	39·7	20·6	22·7	20·1	21·0
TiO_2	1·9	1·8	1·8	1·5	1·5	1·7	1·4	3·6	2·0	0·0	0·0	0·0	0·1	7·0	4·5	2·8	–
Cr_2O_3	–	0·5	–	0·1	–	–	–	–	–	0·0	0·4	–	–	–	–	–	–
Al_2O_3	4·7	7·5	7·4	7·9	7·5	7·1	7·3	7·4	8·0	10·1	11·3	11·8	7·4	3·0	3·8	3·7	5·3
Fe_2O_3	–	–	0·9	2·0	–	0·8	1·7	1·8	–	–	0·0	–	–	2·8	–	–	–
FeO	3·0	2·9	2·1	1·1	5·2	2·0	1·1	1·2	2·5	4·6	5·9	4·2	3·9	13·7	15·8	12·3	–
MnO	–	–	–	–	–	–	–	–	–	–	–	–	0·1	0·6	0·4	0·4	–
MgO	8·1	7·8	7·9	9·0	11·6	7·6	8·6	8·5	8·5	3·6	1·7	1·3	1·4	9·3	8·6	9·2	16·6
CaO	17·6	16·7	17·4	17·7	17·3	16·4	17·3	17·0	17·0	14·2	13·2	12·0	10·4	18·8	20·6	22·4	29·9
Na_2O	21·6	20·8	20·7	2·0	1·2	10·1	2·0	1·9	1·9	5·2	3·4	4·1	5·2	4·0	4·3	5·9	–
K_2O	0·7	0·7	0·8	11·6	10·4	15·4	11·0	11·2	10·7	5·5	10·0	14·2	10·6	0·4	0·5	0·8	–
P_2O_5	–	–	0·4	1·0	0·1	0·3	0·9	1·1	0·1	0·0	0·0	0·1	0·0	–	–	–	–
H_2O	–	–	0·0	0·0	0·0	0·0	3·9	1·9	3·8	2·3	2·1	2·0	2·0	–	–	–	–
CO_2	23·0	21·9	22·0	23·7	23·2	20·8	22·8	22·6	22·3	21·3	20·2	20·2	18·3	19·2	17·8	21·5	25·4
Total	100·0	100·0	100·0	100·0	100·0	100·0	100·0	100·0	100·0	100·0	100·0	100·0	100·0	100·0	100·0	100·0	100·0
X_{Mg}†	0·83	0·83	0·87	0·93	0·80	0·87	0·93	0·93	0·86	0·58	0·34	0·35	0·39	0·55	0·49	0·57	1·00
FeO total (wt %)	3·0	2·9	2·9	2·9	5·2	2·7	2·6	2·8	2·5	4·6	5·9	4·2	3·6	16·2	15·8	12·3	0·0
Fe^{3+}/Fe^{tot} (mol % ratio)	0·00	0·00	0·28	0·62	0·00	0·26	0·58	0·59	0·00	0·00	0·00	0·00	0·00	0·09	0·00	0·00	0·00
K_2O/Na_2O (wt % ratio)	0·03	0·03	0·04	5·83	8·93	1·53	5·60	5·89	5·66	1·05	2·93	3·45	2·03	0·11	0·12	0·14	–

*Weight fraction of added trace element spike. Composition of the spike is provided in Table 7.
†X_{Mg} calculated with $Fe^{2+} = Fe^{tot}$.

was modified to KF7 by lowering the alkali content by 10%, doubling FeO, and increasing MgO by 30% to produce melts saturated in olivine of approximate mantle composition. In starting material KF7 all iron was added as Fe^{2+}, resulting in a more reducing f_{O2}.

The alkalic system

The alkalic system (Alk; Table 1) is an adaptation of Mix1-D from the sodic system, in which half of the Na_2O was replaced by an equal molar amount of K_2O. All experiments were performed at 1 GPa for this system. Iron was added such that the Fe^{3+}/Fe^{tot} molar ratio was 0·26. Owing to addition of hydroxy-apatite, this starting material contains ≤0·015 wt % H_2O.

H_2O-bearing starting materials

To investigate whether addition of H_2O to the bulk system affects the partition coefficients, we first prepared H_2O-bearing starting materials otherwise identical to the anhydrous starting materials. H_2O lowers the liquidus and melting temperatures of minerals, and thus allows liquid immiscibility to persist to lower temperatures. Consequently, we also prepared increasingly Si-rich, H_2O-bearing bulk compositions.

The H_2O-bearing silica-undersaturated potassic systems

The composition of starting material KF4 was modified into bulk compositions containing 2 wt % H_2O (KF6) and 3·8–3·9 wt % H_2O (KF5 and KF8; Table 1). KF5 and KF6 have an elevated Fe^{3+}/Fe^{tot} molar fraction of 0·58–0·59, whereas starting material KF8 contains all iron as Fe^{2+}. The experiments in these systems were performed at 1·7 GPa to remain directly comparable with the results from the anhydrous experiments.

The H_2O-bearing silica-rich potassic systems

Thomsen & Schmidt (2008) reported carbonate–silicate liquid immiscibility during the melting of a carbonated pelite at 3·7–5·0 GPa, 1100°C. Based on their two melt compositions we prepared starting materials ThS1 and ThS2 (details are given in the Electronic Appendix, available for downloading at http://www.petrology.oxfordjournals.org) with all Fe as Fe^{2+} and 2 wt % H_2O, which did not yield liquid immiscibility. We therefore approximately doubled the alkali content (ThS3B, Table 1), which resulted in two coexisting melts, but not in quartz + kyanite saturation as in the study by Thomsen & Schmidt (2008). The composition of ThS4 was then obtained by running an experiment (LM78; Table 2) with ThS3B + quartz + kyanite crystals. All kyanite was consumed in LM78; nevertheless,

Table 2: Run table of experiments with immiscible melts measured for trace elements

Experiment	Starting material	*P* (GPa)	*T* (°C)	Duration static (h)	Duration centrifuge (h)	Acceleration (*g*)	Capsule material	Resulting phases LS	LC	Spinel	Others	V
Anhydrous												
LM22	Mix1-B	1·0	1240	47	5	712	$Au_{50}Pd_{50}$–C	0·43	0·56	<0·01*		
LM36	Mix1-B	1·0	1240	66	5	712	$Au_{50}Pd_{50}$	0·53	0·46	<0·01*		
LM52	Mix1-C	1·0	1240	47·5	4·25	712	$Au_{50}Pd_{50}$	0·52	0·47	<0·01*		
LM58	Mix1-C	1·7	1260	85·7	6	712	$Au_{80}Pd_{20}$–C	0·47	0·52	<0·01*		
LM51	Mix1-D	1·0	1240	44	4·5	712	$Au_{50}Pd_{50}$	0·48	0·52			+
LM45	KF4	1·7	1220	45	4	712	$Au_{50}Pd_{50}$	0·41	0·58	<0·01*		+
LM54	KF4	1·7	1220	40	5	712	$Au_{50}Pd_{50}$	0·45	0·55	<0·01*		+
LM108	KF7	1·7	1220	40			$Au_{50}Pd_{50}$	0·40	0·54	<0·01	0·03 cpx, 0·02 olivine	+
LM59	Alk	1·0	1240	50	5	712	$Au_{50}Pd_{50}$–C	0·44	0·49		0·07 kalsilite	
H_2O-bearing												
LM82	KF6	1·7	1200	40			$Au_{80}Pd_{20}$	0·37	0·61		0·02 phlogopite*	+
LM75	KF5	1·7	1150	50·3			$Au_{80}Pd_{20}$	0·33	0·67			
LM113	KF8	1·7	1150	46·2			$Au_{80}Pd_{20}$	0·3	0·59		0·11 phlogopite	+
LM63	KF5	1·7	1150	45			$Au_{80}Pd_{20}$	0·28	0·59		0·13 phlogopite	
LM73	ThS3B	3·0	1160	43·3			$Au_{80}Pd_{20}$	0·56	0·44			+
LM83	ThS4	3·0	1160	66			$Au_{80}Pd_{20}$	0·62	0·38			+
LM101	ThS4	3·0	1160	66			$Au_{80}Pd_{20}$	0·63	0·37			+

P, pressure; *T*, temperature; C, graphite; LS, silicate glass; LC, quenched carbonatite melt; cpx, clinopyroxene; V, vapour.
*estimated by area proportion.

quartz remained stable, yielding two silica-saturated melts (+K-feldspar + calcite). The melt compositions of LM78 are similar to those of Thomson & Schmidt (2008), the silicate melts corresponding to trachytic compositions.

Capsule material and oxygen fugacity

Starting materials were filled into 2·3, 3·0 or 4·0 mm outer diameter $Au_{50}Pd_{50}$ capsules for the anhydrous compositions, and into $Au_{80}Pd_{20}$ capsules for the H_2O-bearing ones. Using graphite capsules failed as the carbonatite melts vanished from the center of the charge into the pore space and fractures of the graphite capsule. The same problem was reported by Jones *et al.* (1995), who concluded that graphite is by no means an inert container for carbonatite liquids.

As an alternative to using graphite containers we attempted to buffer oxygen fugacity to ~CCO (C-CO-CO_2) by adding graphite powder (LM22) or a single piece of graphite to the charge (LM58 and LM59, Table 2; Fig. 1b). The price to pay for providing a redox partner for Fe^{2+} was near completion of the reaction $FeO_{melt} + C = Fe^0_{metal} + CO_2$ and an almost complete loss of Fe to the capsule wall.

To calculate approximate oxygen fugacities we employed the approach of Kress & Carmichael (1991). We recognize that the melts forming the basis of their model do not contain CO_2 and that our silica-undersaturated alkali-rich compositions are outside their compositional melt array. Furthermore, we have no choice other than to assume equipartitioning for Fe^{2+} and Fe^{3+} between the silicate and carbonatite melt to estimate the Fe^{3+}/Fe^{tot} fraction in the silicate melt. Nevertheless, for graphite-containing experiments, we calculate an f_{O2} of iron–wüstite (IW) ± 0·5, after Kress & Carmichael (1991). In the graphite-free experiments we did not buffer oxygen fugacity and also in these some Fe was lost to the capsule walls. In the absence of a redox partner, only the reaction $FeO = Fe^0_{capsule} + Fe_2O_3$ can account for such a loss. The Fe^{3+}/Fe^{tot} fraction is thus calculated from the deficit of Fe in the bulk composition and result is 0·1–0·3 for experiments with all Fe as Fe^{2+} in the starting material. The calculated f_{O2} values for this series yield quartz–fayalite–magnetite (QFM) + 1 to QFM – 2 (Kress & Carmichael, 1991). The starting materials with elevated Fe^{3+}/Fe^{tot} ratios of 0·25–0·6 resulted, through Fe loss, in bulk Fe^{3+}/Fe^{tot} fractions of 0·6–0·8. Calculated f_{O2} values are slightly below hematite–magnetite (HM).

In the following, we distinguish three groups of experiments: (1) those containing graphite with an f_{O2} around

Table 3: Run table of other experiments not analyzed for trace elements

No.	Starting material	P	T	Duration	Capsule	Phases												
		(GPa)	(°C)	static (h)	material	LS	LC	cpx	qtz	K-fsp	ks	leuc	merw	mel	mtc	Oxides	<5%	V
Anhydrous																		
LM1	Mix1-B	1·0	1240	48	Pt–C	xxxxx	xxxx											
LM16	KF1	1·7	1250	47	$Au_{50}Pd_{50}$	xxxxx		xx					xx			x		+
LM41	KF4	1·7	1220	62	$Au_{50}Pd_{50}$	0·44	0·56			x								+
LM42	KF4	1·7	1220	68	$Au_{80}Pd_{20}$	xxxxx						xx						
LM57	Alk	1·0	1240	21·5	$Au_{50}Pd_{50}$	xxxxx	xxxx										phlog	
LM114	KF7	1·7	1220	47	$Au_{50}Pd_{50}$	xx		xx			xxx		xxx		xxx		sp	
H_2O-bearing																		
LM112	KF5	1·7	1235	65	$Au_{50}Pd_{50}$	xx	xx	xxx		xxx							ol	
LM62	ThS1	3·2	1100	50	$Au_{50}Pd_{50}$	xxx*		xx			xxxx			x				
LM61	ThS1	3·2	1150	24	$Au_{50}Pd_{50}$	xxx*		xx			xxxx			xx				
LM66	ThS2	3·2	1150	66	$Au_{50}Pd_{50}$	x	xxxx	xxx		xx							grt	
LM69	ThS3	3·2	1160	49	$Au_{80}Pd_{20}$	xxx	xxxx			xx								
LM78	ThS3B + qtz + ky	3·0	1160	43·3	$Au_{80}Pd_{20}$	xxx	xxx		xxx	xxx							cc	
LM103	ThS4	3·0	1160	54	$Au_{80}Pd_{20}$	x	xxx			xxx								
Basaltic eclogite model system																		
LM53	DS-1	3·0	1280	46	$Au_{50}Pd_{50}$	xxx*		xxx								xx		
LM56	DS-1	3·0	1320	47	$Au_{50}Pd_{50}$	xx		xxx					xxxx			xxx	ol	
LM72	DS-2	3·0	1280	42	$Au_{50}Pd_{50}$	xxx*		xxxx					xxxx			xx		
LM80	DS-2	3·0	1295	30	$Au_{50}Pd_{50}$	xxx*		xxx								x		
LM74	DS-2	3·0	1310	53	$Au_{50}Pd_{50}$	xxxx							xxx			xx		
LM76	DS-2	3·0	1340	52	$Au_{50}Pd_{50}$	xxxxx							xx		xx			
LM88	DS-3	3·0	1300	65	$Au_{50}Pd_{50}$	xxxxx												
CaO–MgO–Al_2O_3–SiO_2–CO_2 peridotite model system																		
LM111	SH-1	2·4	1430	24	Pt	xxxxx												+

cc, calcite; cpx, clinopyroxene; grt, garnet; K-fsp, potassium feldspar; ks, kalsilite; LC, quenched carbonatite melt; leuc, leucite; LS, silicate melt; merw, merwinite; mel, melilite; mtc, monticellite; ol, olivine; phlog, phlogopite; V, vugs interpreted as fluid estimated abundences: x, ≤5%; xx, 5–20%; xxx ≥20–40%; xxxx, ≥40–60%; xxxxx, ≥60%.
*Single melt but textures did not allow for microprobe analysis of the melt.

IW; (2) those with all Fe added as Fe^{2+} but that do not have graphite; these yield an f_{O2} around QFM; (3) the series of experiments with Fe^{3+}/Fe^{tot} ~0·25–0·6 in the starting material, resulting in f_{O2} values close to HM or ~QFM + 4.

Static piston cylinder experiments

Static experiments (Tables 2 and 3) were performed in an end-loaded piston cylinder with a 14 mm diameter Teflon foil–talc–Pyrex–graphite–MgO assembly. On top of the assembly, a steel plug surrounded by pyrophyllite was inserted to hold the thermocouple in position and prevent extrusion of the assembly. B-type thermocouples ($Pt_{94}Rh_6$–$Pt_{70}Rh_{30}$) were used, and the mullite thermocouple ceramics and the capsule were inserted into the inner MgO rods. The assembly was calibrated against coesite–quartz (Bose & Gangluy, 1995) as well as fayalite + quartz = ferrosilite (Bohlen *et al.*, 1980), resulting in a friction correction of 10% to the nominal pressure. No pressure correction was applied to the thermocouple e.m.f. Experiments were quenched by switching off power, with the initial quench rate being >200°C s^{-1}.

Centrifuge experiments

To physically separate the carbonatite and silicate melts in the anhydrous systems (Table 2), capsules were recovered from the static equilibration experiments and reloaded into the centrifuging piston cylinder, run at identical pressure and temperature, but with an additionally applied centrifugal acceleration of 712 *g*. The centrifuge itself consists of a rotating table of 1·38 m diameter and 850 kg [for details see Schmidt *et al.* (2006)]. The table has two apertures, one of them accommodating a single-stage piston cylinder module, the other a counterweight with similar weight distribution. The centrifuging piston cylinder has a 14 mm diameter assembly identical to that of the static end-loaded piston cylinder. Within this arrangement, the experimental charge sits at a radius of 32 cm; centrifuging at 1400 rev. min^{-1} thus yields 712 *g*. Oil pressure in the hydraulic ram of the piston cylinder cannot be varied while the centrifuge rotates; on the other hand, heating is not advisable when the centrifuge does not rotate, as the current transmitting slip rings would burn out if remaining in a fixed position. Therefore, cold pressure was set to a higher value than the desired run pressure, such that during powering-up of the centrifuge and heating, oil pressure drops to the desired run pressure.

Sample preparation

Alkalis in quenched carbonatites are (at least partly) dissolved and lost if any water, ethanol or acetone is used during sample preparation. Thus, samples were embedded into epoxy, and dry polished with alumina paper until the capsule was slightly opened. The sample was then impregnated under vacuum with a low-viscosity Laromin epoxy to achieve better mechanical coherence of the sample. For further polishing to a level close to the symmetry axis of the capsule, first alumina paper and then diamond paste were used. To remove the diamond paste, pentane, hexane or kerosene were tested, hexane or pentane yielding better results than kerosene, the latter not being able to remove all the diamond paste.

Electron microprobe analysis and calculation of volatile contents

Sample textures and phase identities were determined using a scanning electron microscope (JEOL 6390 LA) with attached energy-dispersive spectrometer (EDS). In the successful experiments (Table 2), quenched liquid compositions (Tables 4–6) and minerals were analyzed using a JEOL 8200 electron microprobe with five wavelength-dispersive spectrometers (WDS). The employed standards were wollastonite, rutile, corundum, fayalite, periclase, albite, jadeite, potassium feldspar, and apatite. Measurement times were 10 and 20 s on peak and background, respectively. Owing to the instability and high diffusivity of alkalis in the silicate glasses and in the quench of the carbonatites, low beam currents and large beam diameters were necessary. For silicate glasses, these were ≤4 nA and 10–20 μm beam diameter, for quenched carbonatites ≤2 nA and ≥20 μm diameter. To compensate for the resulting relatively low counts, large numbers of analyses were acquired. CO_2 in the silicate melt was calculated by difference to 100% total for the anhydrous systems (Table 4). For the water-bearing ones, this was not possible owing to the unknown H_2O partitioning and thus H_2O concentrations within the coexisting melts. In the carbonatite melts, we calculated CO_2 contents by difference from 100% for the anhydrous systems and alternatively as stoichiometric carbonate for all mono- and divalent cations (Tables 4 and 5). These two methods resulted in differences in CO_2 contents of up to 15% relative, except for one sample that had a difference of 27% relative (Table 4). In the experiments with initial molar Fe^{3+}/Fe^{tot} ratios of 0·26–0·62, the carbonatite melt may contain significant Fe^{3+}, introducing a systematic error in the calculation of CO_2 contents by both methods. However, because FeO^{tot} contents are ≤2·9 wt % this error remains at ≤0·3 wt % CO_2 for the difference-to-100 method and at ≤1·8 wt % CO_2 for the stoichiometric method, depending on whether Fe^{3+} forms a carbonate or an oxide component in the carbonatite melt.

LA-ICP-MS

LA-ICP-MS analyses were performed at the Laboratory of Inorganic Chemistry at ETH Zürich. The analyses were carried out using a 193 nm ArF excimer laser ablation system (Lambda Physik, Göttingen Germany) coupled to an ICP-MS system (DRC II +, Perkin Elmer, Norwalk, USA). The samples were ablated for 40 s at 10 Hz repetition rate with 40–80 μm crater diameters; the ablation energy was 17 J cm^{-2}. The reference material NIST 610 was used as an external calibration standard, and Ca was used as internal standard for all melt analyses except for the silicate melts of experiments LM73, LM83, LM101 and LM113, where Al was used because of CaO concentrations ≤1·5 wt %. Data reduction and concentration calculations were carried out using the protocol described by Longerich *et al.* (1996). The analyzed trace elements of this study were Li, Rb, Cs, Be, Sr, Ba, Ca, Mg, Sc, Y, La, Ce, Pr, Nd, Sm, Eu, Gd, Tb, Dy, Er, Yb, Lu, Zr, Hf, V, Mn, Nb, Ta, Mo, U, Th, Co, Cu, Cr, Zn, Ga, Si, Ge, Pb, and P.

RESULTS

Major element compositions of the anhydrous melts

The sodic system

We performed six experiments yielding immiscible melts with starting materials from the sodic system (Table 1). Experiment LM1 was run in a Pt–graphite double capsule at 1 GPa, 1240°C; however, large amounts of the carbonatite melt disappeared into the graphite capsule. Additionally, emulsified carbonatite and silicate melts resulted (Fig. 1a), rendering precise analysis of the melt compositions impossible.

Experiment LM22 was run at the same pressure–temperature conditions as LM1 but in a $Au_{50}Pd_{50}$ capsule with a large piece of graphite added. Centrifuging for 5 h at 712 *g* resulted in perfect separation of the two melts. As expected, the carbonatite melt segregated towards the centre of the centrifuge and the silicate melt and a few spinel crystals towards the outward-directed gravitational

Table 4: Average melt compositions of anhydrous experiments used for trace element partitioning, analyzed by EPMA

Experiment:	LM22*		LM36*		LM52*		LM58*		LM51*		LM45*		LM54*		LM108*		LM59*	
Starting material:	Mix1-B		Mix1-B		Mix1-C		Mix1-C		Mix1-D		KF4		KF4		KF7		Alk1	
P (GPa)/*T* (°C):	1/1240		1/1240		1/1240		1·7/1260		1/1240		1·7/1220		1·7/1220		1·7/1220		1/1240	
Silicate melt†																		
No. of analyses	19		16		13		31		14		22		22		18		26	
SiO_2 (wt %)	33·4(5)	35·6	35·2(7)	36·4	37·5(15)	38·5	36·4(8)	38·2	35·6(11)	37·2	38·2(14)	40·4	38·0(11)	40·3	37·0(7)	42·0	33·3(14)	35·4
TiO_2 (wt %)	3·7(0)	3·9	3·5(1)	3·7	3·2(1)	3·2	3·2(1)	3·4	2·8(2)	2·9	2·4(1)	2·5	2·2(1)	2·4	2·6(1)	3·0	3·5(1)	3·8
Al_2O_3 (wt %)	14·3(3)	15·3	14·2(3)	14·7	14·2(6)	14·5	14·1(1)	14·8	14·1(9)	14·8	12·9(5)	13·6	13·8(8)	14·7	13·0(4)	14·7	12·3(7)	13·0
FeO (wt %)	0·0(0)	0·0	2·4(1)	2·5	3·3(1)	3·4	0·1(0)	0·1	2·8(2)	3·0	2·9(1)	3·1	3·3(1)	3·5	5·1(2)	5·7	0·1(0)	0·1
MgO (wt %)	11·7(2)	12·4	11·9(2)	12·3	9·0(2)	9·2	10·4(2)	10·9	9·2(6)	9·6	9·8(3)	10·4	9·2(4)	9·8	7·8(2)	8·8	12·2(4)	10·9
CaO (wt %)	17·1(3)	18·3	15·6(4)	16·2	14·5(10)	14·9	15·2(4)	15·9	14·6(4)	15·3	14·8(3)	15·7	13·7(4)	14·5	9·8(4)	11·2	17·0(5)	18·0
Na_2O (wt %)	13·2(3)	14·1	13·4(12)	13·9	15·6(13)	16·0	15·6(11)	16·4	15·8(3)	16·5	2·0(1)	2·1	2·0(2)	2·1	1·2(2)	1·4	7·8(2)	8·2
K_2O (wt %)	0·3(0)	0·4	0·4(0)	0·4	0·3(0)	0·3	0·4(0)	0·4	0·6(0)	0·6	10·9(1)	11·5	11·2(5)	11·9	11·6(2)	13·1	9·9(1)	10·5
P_2O_5 (wt %)	0·0097(2)‡	0·0	0·0097(4)‡	0·0	0·0093(4)‡	0·0	0·0120(4)‡	b.d.	0·3(1)	0·3	0·7(1)	0·7	0·7(2)	0·7	0·1(1)	0·1	0·1(1)	0·1
Total	93·7	100·0	96·6	100·0	97·4	100·0	95·3	100·0	95·7	100·0	94·6	100·0	94·1	100·0	88·2	100·0	94·1	100·0
CO_2§ (wt %)	6·3		3·4		2·6		4·7		4·3		5·4		5·9		11·8		5·9	
K_2O/Na_2O (wt% ratio)	0·02(0)		0·03(0)		0·02(0)		0·02(0)		0·04(0)		5·53(35)		5·6(7)		9·7(16)		1·27(4)	
X_{Mg} (all Fe as FeO) (molar)	1·00(2)		0·90(2)		0·83(2)		1·00(3)		0·85(8)		0·86(3)		0·83(4)		0·73(2)		1·00(5)	
Ca/ (Ca + Mg + Fe) (molar ratio)	0·51(1)		0·46(1)		0·49(4)		0·51(2)		0·49(2)		0·48(1)		0·47(2)		0·40(2)		0·54(2)	
(Si + Ti + Al)/ (Si + Ti + Al + Fe + Mg + Ca + Na + K) (molar ratio)	0·48(1)		0·48(2)		0·51(3)		0·50(2)		0·49(2)		0·53(3)		0·54(2)		0·79		0·48(3)	
NBO/T	1·49		1·52		1·37		1·40		1·42		1·20		1·11		1·00		1·58	

(continued)

Table 4: Continued

Experiment:	LM22*	LM36*	LM52*	LM58*	LM51*	LM45*	LM54*	LM108*	LM59*
Starting material:	Mix1-B	Mix1-B	Mix1-C	Mix1-C	Mix1-D	KF4	KF4	KF7	Alk1
P (GPa)/*T* (°C):	1/1240	1/1240	1/1240	1·7/1260	1/1240	1·7/1220	1·7/1220	1·7/1220	1/1240
Carbonatite melt									
No. of analyses†	41	30	24	36	20	37	30	26	29
SiO_2 (wt %)	5·5(32)	4·1(18)	1·8(11)	3·3(19)	3·0(14)	9·6(3)	8·3(15)	7·6(8)	1·5(1·2)
TiO_2 (wt %)	0·9(5)	0·6(3)	0·3(2)	0·6(3)	0·5(2)	1·5(5)	1·0(1)	1·2(2)	0·4(0·2)
Al_2O_3 (wt %)	0·8(7)	0·5(3)	0·1(1)	0·3(02)	0·3(2)	1·5(1)	1·5(5)	1·5(2)	0·1(1)
FeO (wt %)	0·0(0)	0·5(2)	0·5(2)	b.d.	0·6(2)	1·9(6)	2·0(2)	3·4(3)	b.d.
MgO (wt %)	7·4(14)	8·2(9)	5·8(16)	7·6(14)	6·4(1)	11·3(11)	10·1(10)	11·3(4)	5·0(2)
CaO (wt %)	22·4(13)	21·7(11)	19·1(22)	22·1(12)	21·8(9)	27·4(18)	26·4(29)	23·8(27)	20·4(22)
Na_2O (wt %)	21·6(29)	24·1(19)	25·3(17)	25·1(11)	25·4(9)	2·6(13)	2·6(5)	1·6(4)	12·4(7)
K_2O (wt %)	0·7(1)	0·8(1)	0·6(1)	0·6(0)	1·0(1)	12·3(11)	12·3(6)	11·5(23)	18·4(5)
P_2O_5 (wt %)	0·015(1)‡	0·0185(3)‡	0·0165(4)‡	0·020(2)‡	0·4(1)	1·4(1)	0·9(2)	0·2(1)	0·4(1)
Total	59·6	60·5	53·4	59·6	59·4	69·5	65·1	62·3	58·6
CO_2§ (wt %)	40·4	39·5	46·6	40·4	40·6	30·5	34·9	38·0	41·4
CO_2¶ (wt %)	41·4	43·8	39·8	43·8	42·9	42·6	40·6	39·6	38·9
K_2O/Na_2O (wt % ratio)	0·03(1)	0·03(0)	0·02(0)	0·03(0)	0·04(0)	4·68(24)	4·74(10)	7·2(23)	1·49(10)
X_{Mg} (all Fe as FeO) (molar)	1·00(27)	0·96(15)	0·95(37)	1·00(26)	0·95(21)	0·92(13)	0·90(13)	0·86(4)	1·00(55)
Ca/(Ca + Mg + Fe) (molar ratio)	0·69(6)	0·65(5)	0·69(11)	0·68(6)	0·70(5)	0·62(5)	0·63(8)	0·56(7)	0·75(12)
(Si + Ti + Al)/ (Si + Ti + Al + Fe + Mg + Ca + Na + K) (molar ratio)	0·11(8)	0·08(4)	0·04(3)	0·06(5)	0·06(3)	0·16(2)	0·15(4)	0·15(2)	0·03(2)

*Compositions of right hand columns normalized to a volatile-free basis.
†Number of averaged analyses. Numbers in parentheses are 1σ errors.
‡From LA-ICP-MS analyses.
§CO_2 calculated by difference to 100.
¶CO_2 calculated by stoichiometry.
NBO/T calculated with all Fe as Fe^{2+} on a volatile-free basis.

Table 5: Average melt compositions of H_2O-bearing experiments used for trace element partitioning, analyzed by EPMA

Experiment:	LM82*		LM75*		LM113*		LM63*		LM73*		LM83*		LM101*	
Starting material:	KF6		KF5		KF8		KF5		ThS3B		ThS4		ThS4	
P (GPa)/*T* (°C):	1·7/1200		1·7/1150		1·7/1150		1·7/1150		3/1160		3/1160		3/1160	
Silicate melt														
No. of analyses†	12		14		20		11		23		17		22	
SiO_2 (wt %)	38·0(1)	42·8	43·0(2)	48·6	42·4(3)	48·4	49·0(2)	53·6	50·5(2)	55·4	63·1(6)	68·6	62·0(3)	67·6
TiO_2 (wt %)	5·1(0)	5·7	1·6(0)	1·8	1·9(1)	2·2	1·0(3)	1·1	0·1(0)	0·1	0·2(0)	0·2	0·2(0)	0·2
Al_2O_3 (wt %)	14·0(1)	15·8	15·5(1)	17·7	16·1(3)	18·4	17·6(4)	19·3	19·2(2)	21·1	10·7(1)	11·7	11·1(2)	12·1
MnO (wt %)	b.d.	b.d.	b.d.	b.d.	b.d.	0·0	b.d.	b.d.	b.d.	b.d.	0·0	0·1	0·0	0·0
FeO (wt %)	2·6(0)	2·9	1·7(0)	1·9	1·7(1)	2·0	1·4(5)	1·6	1·7(1)	1·9	2·1(1)	2·3	2·3(1)	2·6
MgO (wt %)	5·8(1)	6·6	4·5(1)	5·1	3·7(1)	4·2	2·3(6)	2·6	0·3(0)	0·3	0·5(0)	0·6	0·5(0)	0·6
CaO (wt %)	8·8(1)	10·0	6·7(1)	7·6	6·5(2)	7·4	3·5(4)	3·8	1·5(1)	1·6	1·1(0)	1·2	1·3(1)	1·4
Na_2O (wt %)	1·9(1)	2·1	1·9(1)	2·2	2·0(2)	2·2	1·9(4)	2·1	3·1(2)	3·4	3·6(1)	3·9	3·5(2)	3·8
K_2O (wt %)	12·4(1)	14·0	13·2(2)	14·9	13·2(3)	15·0	14·5(2)	15·9	14·8(3)	16·2	10·6(1)	11·5	10·8(2)	11·8
P_2O_5 (wt %)	0·0096(3)‡	0·0	0·3(2)	0·3	0·1(1)	0·1	0·2(0)	0·2	0·0396(5)‡	0·0	0·0077(9)‡	0·0	0·0068(5)‡	0·0
Total	88·6	100·0	88·5	100·0	87·6	100·0	91·4	100·0	91·1	100·0	92·1	100·0	91·8	100·0
K_2O/Na_2O (wt%-ratio)	6·7(2)		6·9(4)		6·6(7)		7·6(15)		4·7(3)		2·96(10)		3·07(17)	
X_{Mg} (all Fe as FeO) (molar)	0·80(1)		0·82(2)		0·80(3)		0·74(26)		0·21(4)		0·30(2)		0·28(3)	
Ca/ (Ca + Mg + Fe) (molar ratio)	0·47(1)		0·47(1)		0·50(2)		0·44(8)		0·47(3)		0·32(1)		0·34(2)	
(Si + Ti + Al)/ (Si + Ti + Al + Fe + Mg + Ca + Na + K) (molar ratio)	0·62(0)		0·68(1)		0·69(1)		0·76(2)		0·80(1)		0·83(1)		0·83(1)	
NBO/T	0·75		0·51		0·46		0·25		0·12		0·20		0·21	
Carbonatite melt														
No. of analyses*	28		29		20		19		26		27		32	
SiO_2 (wt %)	9·9(9)		11·9(16)		10·0(20)		5·7(12)		1·4(8)		1·8(5)		2·5(10)	
TiO_2 (wt %)	3·1(5)		1·4(2)		1·7(4)		0·8(2)		0·1(0)		0·1(0)		0·1(0)	
Al_2O_3 (wt %)	2·6(2)		3·2(4)		2·6(6)		1·3(3)		1·5(4)		0·2(1)		0·3(1)	
MnO (wt %)	b.d.		b.d.		b.d.		b.d.		b.d.		0·2(1)		0·2(1)	
FeO (wt %)	2·5(3)		2·4(2)		2·4(4)		2·2(2)		6·4(4)		5·3(4)		5·3(7)	
MgO (wt %)	9·8(4)		10·3(6)		9·4(9)		9·6(7)		2·7(3)		3·1(2)		3·1(3)	
CaO (wt %)	22·3(14)		23·9(22)		26·8(35)		28·2(21)		25·4(37)		26·6(17)		27·1(26)	
Na_2O (wt %)	2·5(3)		2·7(5)		2·4(7)		2·1(5)		6·5(12)		9·6(8)		8·3(15)	
K_2O (wt %)	11·5(11)		8·1(9)		7·6(35)		8·9(12)		12·1(25)		8·7(9)		8·5(14)	
P_2O_5 (wt %)	0·0113(8)‡		1·5(3)		0·3(1)		1·5(3)		0·264(7)‡		0·0142(9)‡		0·0084(4)‡	
Total	64·2		65·4		66·3		60·3		56·0		55·6		55·5	
CO_2§ (wt %)	36·8		37·2		39·4		39·6		37·0		38·4		37·8	
K_2O/Na_2O (wt%-ratio)	4·70(73)		3·02(62)		3·17(173)		4·2(11)		1·86(52)		0·90(12)		1·02(25)	
X_{Mg} (all Fe as FeO) (molar)	0·88(5)		0·88(7)		0·87(11)		0·89(9)		0·43(5)		0·51(4)		0·51(6)	
Ca/ (Ca + Mg + Fe) (molar ratio)	0·59(4)		0·60(7)		0·64(10)		0·65(6)		0·74(13)		0·76(6)		0·76(9)	
(Si + Ti + Al)/ (Si + Ti + Al + Fe + Mg + Ca + Na + K) (molar ratio)	0·21(3)		0·23(4)		0·20(5)		0·12(3)		0·04(2)		0·04(2)		0·05(3)	

*Compositions of right hand columns normalized to a volatile-free basis.
†Number of averaged analyses. Numbers in parentheses are 1σ errors.
‡From LA-ICP-MS analysis.
§CO_2 calculated by stoichiometry.
NBO/T calculated with all Fe as Fe^{2+} on a volatile-free basis.

Table 6: Electron microprobe analyses of further melt compositions

Experiment:	LM111*		LM56*		LM74*		LM76*		LM88*		LM42*		LM42*	
Starting material:	SH-1		DS1		DS2		DS2		DS3		KF4		KF4	
P (GPa)/*T* (°C):	2·4/1430		3/1340		3/1310		3/1340		3/1300		1·7/1220		1·7/1220	
No. of analyses:†	20		5		20		22		14		16		16	
Melt:	LS		LS		LS		LS		LS		LS		LC	
SiO_2	22·1(3)	29·7	31·6(4)	33·9	32·4(3)	34·6	25·5(23)	31·7	21·7(4)	29·2	30·9(15)	36·1	6·3(17)	9·3
TiO_2	–	–	5·0(1)	5·3	4·4(1)	4·7	4·7(3)	5·8	2·9(1)	3·9	2·4(0)	2·8	0·9(3)	1·4
Al_2O_3	5·2(2)	7·0	3·2(2)	3·4	4·7(1)	5·0	4·0(4)	5·0	3·8(1)	5·2	9·5(7)	11·1	0·7(5)	1·1
FeO	–	–	12·3(2)	13·1	10·9(3)	11·6	4·4(3)	5·5	7·9(2)	10·6	3·2(1)	3·8	1·9(4)	2·8
MnO	–	–	0·7(1)	0·8	0·6(1)	0·7	0·3(1)	0·4	0·3(1)	0·5	–	–	–	–
MgO	15·7(3)	21·1	11·2(2)	12·0	11·1(2)	11·9	14·9(13)	18·5	9·6(2)	13·0	10·1(3)	11·8	12·0(35)	17·8
CaO	31·1(4)	42·2	23·3(5)	24·9	21·3(5)	22·8	21·5(16)	26·8	22·7(3)	30·6	17·1(8)	20·0	28·3(79)	42·2
Na_2O	–	–	5·6(7)	6·0	7·4(2)	7·9	4·5(4)	5·6	4·6(2)	6·2	2·2(1)	2·5	3·3(12)	5·0
K_2O	–	–	0·5(1)	0·5	0·8(0)	0·9	0·5(0)	0·6	0·6(0)	0·8	9·5(1)	11·1	11·9(46)	17·7
P_2O_5	–	–	–	–	–	–	–	–	–	–	0·7(1)	0·8	1·7(8)	2·6
Total	74·4	100·0	93·3	100·0	93·6	100·0	80·3	100·0	74·3	100·0	85·6	100·0	67·2	100·0
CO_2‡	25·6		6·7		6·4		19·7		25·7		14·4		32·8	
X_{Mg}	1		0·62		0·646		0·875		0·685		0·848		0·92	

Experiment	LM112*		LM112*		LM114*		LM103*		LM103*		LM69*		LM69*		LM16*	
Starting material	KF7		KF7		KF5		ThS4		ThS4		ThS3		ThS3		KF1	
P (GPa)/*T* (°C):	1·7/1235		1·7/1235		1·7/1220		3/1160		3/1160		3·2/1160		3·2/1160		1·7/1250	
No. of analyses:	15		8		21		14		20		15		15		20	
Melt:	LS		LC		LS		LS		LC		LS		LC		LS	
SiO_2	26·3(27)	31·3	5·5(33)	8·4	25·6(4)	31·4	64·1(14)	69·0	1·4(7)	2·3	51·7(57)	58·0	0·4(2)	0·7	32·1(3)	35·9
TiO_2	2·7(3)	3·2	0·6(4)	0·9	2·0(1)	2·4	0·5(1)	0·5	0·1(1)	0·2	0·0(0)	0·1	0·1(1)	0·2	0·7(0)	0·8
Al_2O_3	3·3(6)	3·9	0·6(5)	0·9	4·5(1)	5·5	7·5(10)	8·1	0·1(1)	0·1	18·2(11)	20·4	2·0(12)	3·5	6·3(2)	7·0
FeO	4·4(3)	5·3	1·3(6)	2·0	1·4(1)	1·7	3·3(3)	3·6	5·4(7)	9·1	1·1(5)	1·2	8·0(18)	14·3	4·5(2)	5·0
MnO	–	–	–	–	–	–	–	–	–	–	–	–	–	–	–	–
MgO	10·3(37)	12·3	5·4(7)	8·1	8·7(2)	10·7	1·0(1)	1·1	3·8(3)	6·3	0·2(1)	0·2	2·8(6)	5·0	9·1(3)	10·1
CaO	25·6(23)	30·5	32·5(15)	49·3	27·5(5)	33·7	2·0(3)	2·1	28·6(14)	48·6	1·0(4)	1·1	23·2(107)	41·3	31·4(4)	35·1
Na_2O	1·7(2)	2·0	2·8(6)	4·2	3·1(1)	3·8	4·2(5)	4·5	10·2(10)	17·1	2·9(10)	3·3	6·9(41)	12·2	0·9(1)	1·0
K_2O	9·4(13)	11·2	16·9(17)	25·6	8·5(2)	10·4	10·3(6)	11·1	9·6(8)	16·2	14·0(14)	15·7	12·5(60)	22·2	4·0(1)	4·4
P_2O_5	0·2(1)	0·3	0·4(1)	0·6	0·2(0)	0·3	–	–	–	–	–	–	–	0·4	0·6(1)	0·7
Total	84·0	100·0	66·0	100·0	81·6	100·0	92·9	100·0	59·4	100·0	89·1	100·0	56·1	100·0	89·5	100·0
CO_2‡	16·0		34·0		18·4		7·1		40·6		10·9		43·9		10·5	
X_{Mg}	0·806		0·881		0·918		0·351		0·555		0·238		0·386		0·784	

*Compositions of right hand columns normalized to a volatile-free basis.
†Number of averaged analyses. Numbers in parentheses are 1σ errors.
‡CO_2 calculated by difference to 100.
LC, quenched carbonatite melt; LS, silicate melt.

bottom of the capsule. In this experiment almost all Fe was lost to the capsule. Experiment LM36 was run at the same conditions but without graphite added. The melt compositions in experiments LM22 and LM36 are almost identical, with the exception that 2·5 and 0·5 wt % FeO are present in the silicate and carbonatite melts of experiment LM36. Experiment LM52 was performed at the same conditions as the previous experiments but with starting material Mix1-C containing 0·5 wt % Cr_2O_3. The silicate melts (Table 4) of experiments LM22, LM36 and LM52 contain 35·6–38·5 wt % SiO_2 and 14·9–18·3 wt % CaO, and alkali contents amount to 14·1–16·0 wt % Na_2O and 0·3–0·4 wt % K_2O. Oxide concentrations of silicate melts are always given on a volatile-free basis whereas

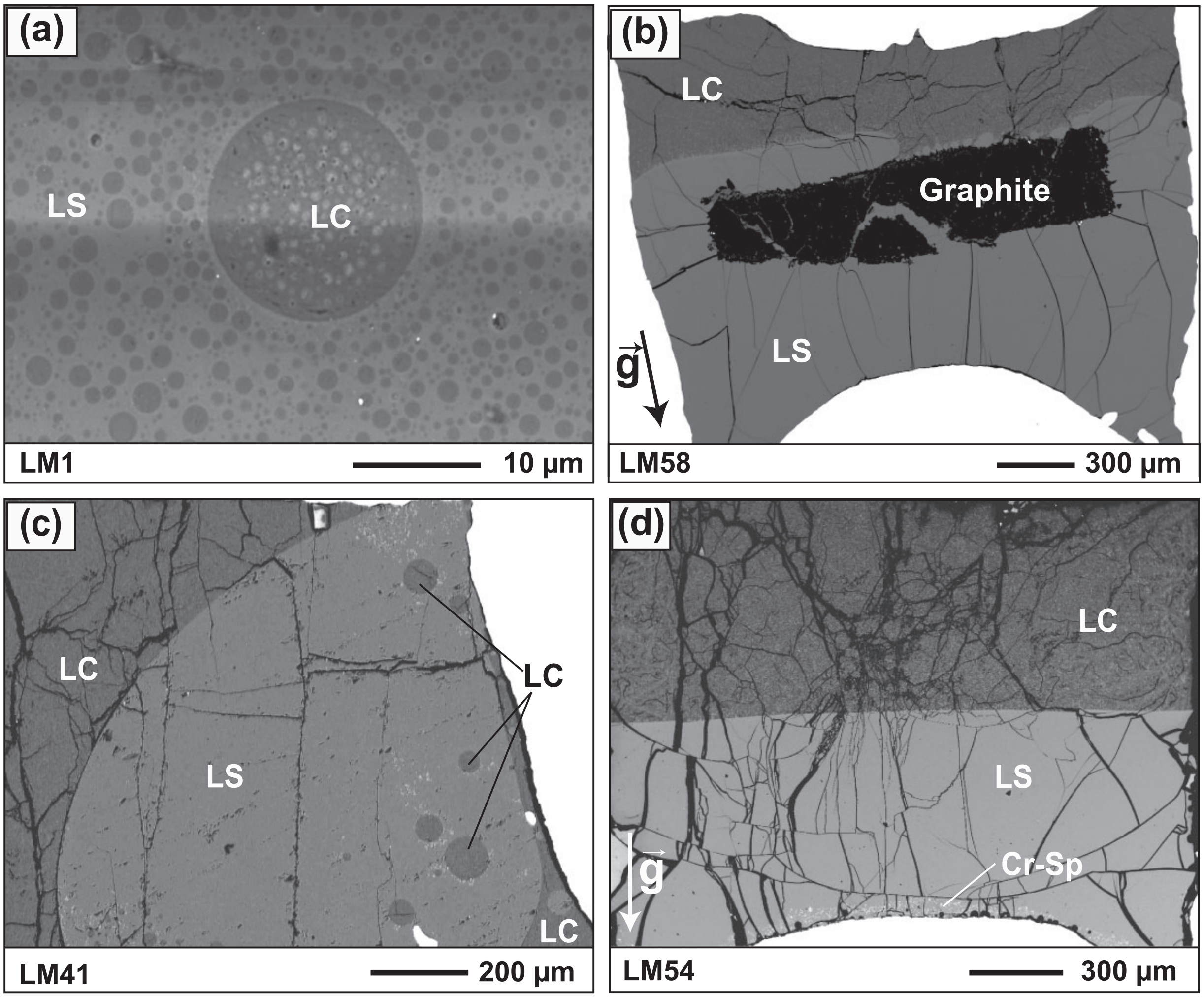

Fig. 1. Backscattered electron images of experiments from the anhydrous systems. (a) In static experiments, poor physical separation of quenched carbonatite melt dispersed in the silicate glass and vice versa, rendered analysis impossible (LM1, 1·0 GPa, 1240°C). (b) Centrifuge experiment LM58 (1·7 GPa, 1260°C) yielded separated quenched carbonatite melt and silicate glass, additionally containing a single piece of graphite to buffer f_{O2}. (c) Experiment LM41 (1·7 GPa, 1220°C) yielded, in quenched carbonatite, a large silicate glass blob containing minor dispersed Cr-spinel, a few larger quenched carbonatite globules and fine dispersed carbonatite melt droplets. These inclusions impede large area laser-ablation analysis. (d) Centrifuged experiment LM54 (1·7 GPa, 1220°C) resulted in a perfect separation of the two melts and Cr-spinel crystals segregated to the gravitational bottom of the capsule. LC, quenched carbonatite melt; LS, silicate glass; *g*, direction of centrifuge acceleration.

those of carbonatite melts correspond to the values measured by electron microprobe analysis (EPMA). These melt compositions, albeit with a less extreme Na/K ratio, resemble the foidites and haüynophyres from Monte Vulture, Italy (Beccaluva *et al.*, 2002; D'Orazio *et al.*, 2007; see also compilation by Peccerillo, 2005), where a strongly silica-undersaturated alkaline series is associated with the eruption of carbonatites (Stoppa & Principe, 1997; D'Orazio *et al.*, 2007). The carbonatite melts contain 1·8–5·5 wt % SiO_2, 19·1–22·4 wt % CaO, 21·6–25·3 wt % Na_2O and 0·6–0·8 wt % K_2O. Chromium had no effect on melt compositions; experiment LM52 had almost all the Cr segregated in Cr-spinel at the bottom of the capsule. The X_{Mg} of the silicate melts (0·90 and 0·83 in LM36 and LM52) are lower than in the carbonatite melts (0·96 and 0·95, respectively) which is true for all the experiments of this study (Tables 4–6).

Experiment LM51 was run with starting material Mix1-D; that is, with an increased Fe^{3+}/Fe^{tot} and with P_2O_5. The experiment yielded silicate and carbonatite melts similar to those of LM52 (Table 4), indicating that at the low FeO contents of this series oxidation state has little influence on the major element compositions of the conjugate melts. Experiment LM58 was run with Mix1-D at higher pressure (1·7 GPa) than LM51 (1·0 GPa) to evaluate the effect of pressure. Additionally, with the intention to buffer

f_{O_2} to CCO, a piece of graphite was added to the charge (Fig. 1b). Resulting melt compositions are within error of experiment LM52, except for FeO contents <0·1 wt %. The narrow variation in the melt compositions of experiments LM51 and LM22 indicates that a pressure increase from 1·0 to 1·7 GPa has little effect on the miscibility gap (Fig. 2). The addition of graphite allowed for a reduction of Fe^{2+} to Fe^0, and its subsequent loss to the metal capsule.

The compositional gaps between conjugate silicate and carbonatite melts are visualized in ($SiO_2 + TiO_2 +$

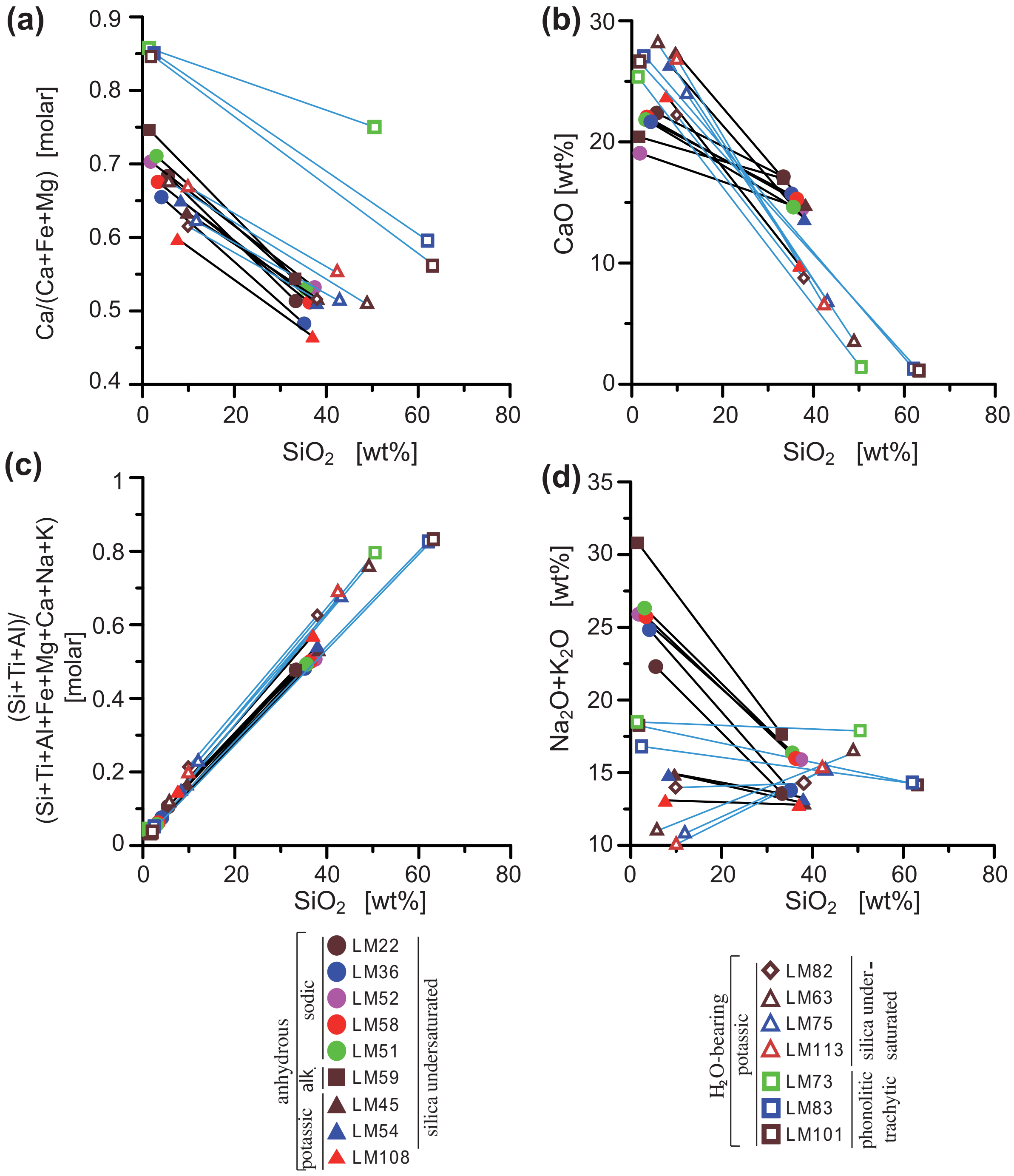

Fig. 2. Graphic illustration of the miscibility gap width of anhydrous (black lines) and H_2O-bearing systems (blue lines) in terms of SiO_2 vs (a) molar Ca/(Ca + Fe + Mg), (b) CaO (in wt %), (c) molar (Si + Ti + Al)/(Si + Ti + Al + Fe + Mg + Ca + Na + K) and (d) total alkali contents (in wt %).

Al_2O_3)–(Ca,Mg,Fe)O–$(Na,K)_2O$ space projected from CO_2 (+ H_2O) (Fig. 3a) and in SiO_2 vs CaO, Ca/(Ca + Fe + Mg), or the mol fraction of network forming cations (Fig. 2a–c). In the sodic system the miscibility gap extends from 35·6 to 5·5 wt % SiO_2, 0·51 to 0·65 molar Ca/(Ca + Mg + Fe), and amounts to a ΔCaO of 4·6–7·4 wt %. The CaO concentrations in the conjugate melts almost overlap; the highest CaO of the silicate melts is 17·1 wt %, whereas the lowest CaO in the carbonatite melts is 19·1 wt %. Neither the pressure difference of 0·7 GPa nor the amount and oxidation state of Fe has much influence on the miscibility gap width. It is worth noting that Na_2O and K_2O are partitioned into the carbonatite melt, resulting in a negative slope of the two-melt tielines in total alkalis vs SiO_2 space (Fig. 2d).

The potassic system

Two starting materials, KF4 with $Fe^{3+}/Fe^{tot} = 0{\cdot}62$ and KF7 with all Fe as Fe^{2+}, were employed (Table 1). Experiment LM41 (starting material KF4) run statically at 1·7 GPa, 1220°C yielded one large silicate melt blob contained in quenched carbonatite melt. The silicate melt

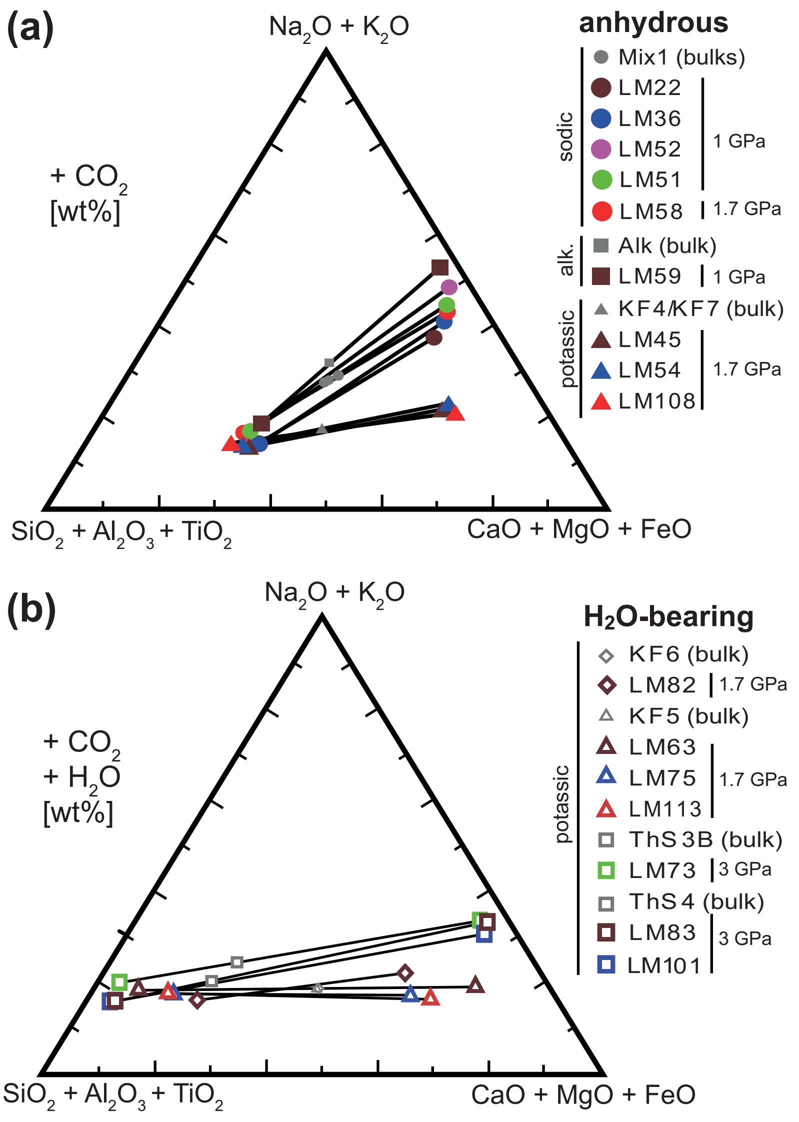

Fig. 3. Compositional gaps between immiscible silicate and carbonatite melts visualized in ($SiO_2 + Al_2O_3 + TiO_2$)–(Ca,Mg,Fe)O–$(Na,K)_2O$ space projected from CO_2 (+H_2O) in wt % for (a) anhydrous compositions and (b) H_2O-bearing compositions (projection following Hamilton *et al.*, 1979; Lee & Wyllie, 1997). The tie-lines between the conjugate melts have strongly positive slopes for the anhydrous sodic compositions and slightly positive ones for the anhydrous potassic systems. In the H_2O-bearing systems, subhorizontal tie-lines for the silica-undersaturated compositions are replaced by slightly positive tie-lines for the Si-rich bulk compositions. It should be noted that pressure co-varies with the compositional groups but that the apparent effect of pressure would be opposing in (a) and (b), indicating that the compositional effects are dominant. The grey symbols indicate experimental bulk compositions.

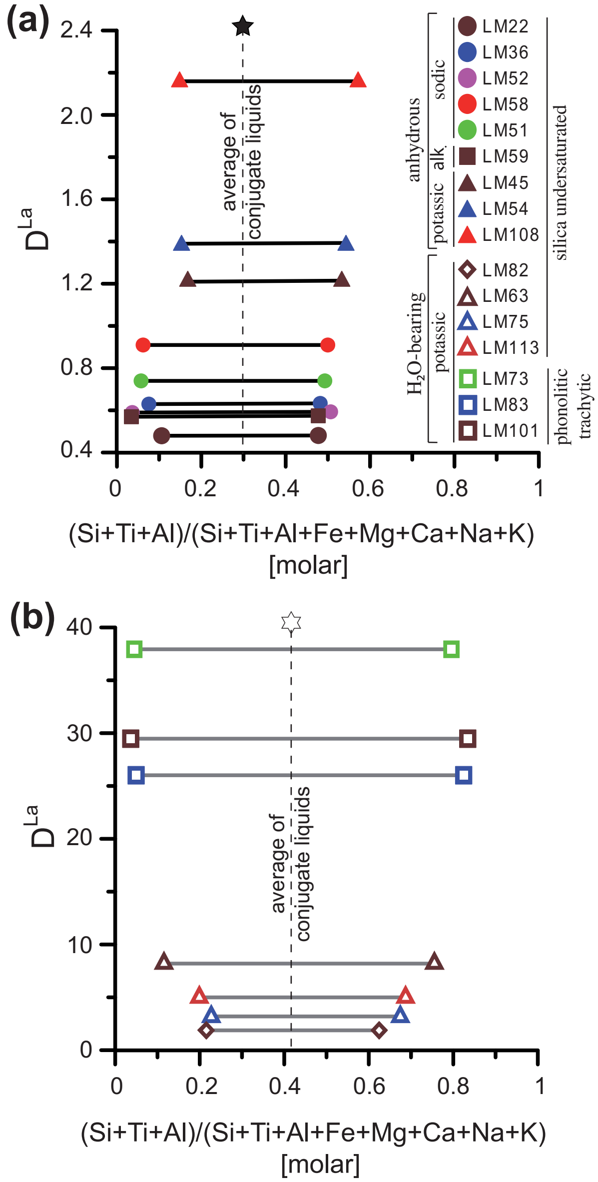

Fig. 4. D^{La} vs molar $(Si+Ti+Al)/(Si+Ti+Al+Fe+Mg+Ca+Na+K)$ for (a) the anhydrous and (b) the H_2O-bearing systems. The vertical lines indicate the average of the conjugate liquids taken as an approximation for the composition of the consolute point of the miscibility gap (see Fig. 10a and b).

contains minor Cr-spinel (Fig. 1c) and carbonatite melt droplets, impeding large area laser ablation measurements.

Conjugate melt pairs were therefore separated by centrifugation (experiments LM45 and LM54, Fig. 1d; Table 4), small Cr-spinels collecting at the gravitational bottom of the capsules. These two experiments were run with identical starting materials, capsules and run conditions to verify the reproducibility of our experimental strategy. Immiscible melt compositions are plotted in Figs 2–4. The silicate melts of LM45 and LM54 (Table 4) contain about 40·4 wt % SiO_2, 14·5–15·7 wt % CaO, 2·1 wt % Na_2O and ~11·7 wt % K_2O, giving K_2O/Na_2O wt-ratios of ~5·5. These two silicate melts compare well with the natural San Venanzo kamafugites from Central Italy (Martin *et al.*, 2012). The carbonatite melts contain 8·3–9·6 wt % SiO_2, 26·4–27·4 wt % CaO, 2·6 wt % Na_2O and 12·3 wt % K_2O, giving $K_2O/Na_2O = 4·7$.

Experiment LM108, run at 1·7 GPa, 1220°C with all Fe as Fe^{2+} in the starting material KF7, resulted in ~50 vol. % carbonatite melt and ~40 vol. % silicate melt; the latter contained in part quenched cpx and bubbles. At the bottom of the capsule, leucite, clinopyroxene, olivine and spinel accumulated. The silicate melt contains 42·0 wt % SiO_2, 11·2 wt % CaO, 1·4 wt % Na_2O and 13·1 wt % K_2O, somewhat richer in Si and poorer in Mg and Ca than in experiments LM45 and LM54. The carbonatite melt is slightly poorer in Ca, but richer in alkalis and iron than for LM45.

The miscibility gaps in the potassic system (Fig. 2) range from 40·3 to 9·6 wt % SiO_2, 14·8 to 23·8 wt % CaO, and 0·48 to 0·56 molar $Ca/(Ca+Mg+Fe)$. The dry carbonatite melts contain 8–10 wt % SiO_2 in the potassic system, compared with 2–5 wt % SiO_2 in the sodic system. Similarly, the silicate melts have ~5 wt % higher SiO_2 in the potassic system, in which the separation in CaO content is also much clearer than in the sodic system. Although the total alkali contents of the silicate melts overlap for the potassic and sodic systems ($Na_2O+K_2O =$ 13·6–14·5 and 14·1–17·1 wt %, respectively), the total alkali contents of the potassic carbonatites ($Na_2O+K_2O = $ 13·1–14·9 wt %) are lower than for the sodic ones ($Na_2O+K_2O = $ 22·3–26·4 wt %). This reflects in part the higher bulk alkali contents and in part a stronger partitioning of the alkalis into the carbonatite melt in the sodic system.

The alkalic system

The starting material Alk-1 (Table 1) is identical to Mix1 of the sodic system except that half of the Na_2O was replaced by a molar equal amount of K_2O. The static experiment LM57 yielded immiscible melts and kalsilite crystals at 1 GPa, 1240°C. The centrifuged experiment LM59, also with Alk-1, had graphite added and resulted in the same phase assemblage as LM57 (Tables 2 and 3). The silicate melt of LM59 contains 35·4 wt % SiO_2, 18·0 wt % CaO, 8·2 wt % Na_2O and 10·5 wt % K_2O, giving $K_2O/Na_2O = 1·3$. The carbonatite melt contains 1·5 wt % SiO_2, 20·4 wt % CaO, 12·4 wt % Na_2O and 18·4 wt % K_2O, giving $K_2O/Na_2O = 1·49$. Compared with the sodic and potassic systems, this results in the highest total alkali content (32·4 wt %, Figs 2d and 3a). The compositional gap between the two conjugate melts has a similar width to that in experiment LM22 in the sodic system; it is located at 35·4–1·5 wt % SiO_2, 18·0–20·4 wt % CaO, and 0·54–0·75 molar $Ca/(Ca+Mg+Fe)$ (Figs 2a–c and 3a).

Liquid immiscibility in alkali-poor, silica-deficient systems

Dasgupta *et al.* (2006) investigated the partial melting of carbonated silica-deficient basaltic eclogites. Two different liquids with carbonatite and silicate melt compositions were postulated to coexist and their quench was measured at 3 GPa at temperatures of 1225–1375°C. The Na contents measured in the quenched melts and in clinopyroxene indicate a 30% Na deficit with respect to the bulk composition (e.g. their experiment A413). Thus, Dasgupta *et al.* (2006) provided a calculated Na content for their carbonatite melt that is nine times the measured Na concentration. We synthesized this relatively low alkali composition in a 50:50 mixture of the silicate and the corrected carbonatite melts (Table 1, DS-1, 4·0 and 0·4 wt % bulk Na_2O and K_2O, their experiment A413) to determine partition coefficients (for details see the Electronic Appendix). Unfortunately, we did not obtain liquid immiscibility for this bulk composition at 3 GPa, 1280°C. In a subsequent step, we recalculated phase abundances from mass balance, not employing Na or K [phase analyses from tables 3–7 of Dasgupta *et al.* (2006)]. From the phase abundances we recalculated the bulk Na and K contents of the melt(s) to 4·3 wt % Na_2O and 0·5 wt % K_2O (Table 1, starting material DS-2). As we still did not obtain immiscibility, we arbitrarily increased the bulk alkali contents by ~40% to 5·9 wt % Na_2O and 0·8 wt % K_2O (Table 1, starting material DS-3), but still did not obtain liquid immiscibility (Table 3) but a single melt. These melt compositions vary in the range 29–34 wt % SiO_2 and calculated 6–26 wt % CO_2 (Table 6) and generally fall into the center of the proposed miscibility gap. Apparently, at the reported conditions and compositions, corrected or uncorrected for alkali losses, liquid immiscibility is not achieved. Instead, we only obtained a single melt when using the highest alkali content (LM88, Table 3) or a single melt and 2–4 crystal phases (clinopyroxene, merwinite, monticellite, olivine and oxides).

Similarly, we attempted to reproduce liquid immiscibility in the $CaO-MgO-Al_2O_3-SiO_2-CO_2$ system as reported by Novella & Keshav (2010) at 2·4 GPa. Running a bulk composition (Table 1, SH-1) that corresponds to a 50:50 mixture of the two melts in the middle of the alleged miscibility gap (1430°C) resulted in a homogeneous liquid (Table 3). Back-scattered electron images of these and the above experiments are provided in the Electronic Appendix.

We note that for both studies, evidence of liquid immiscibility is circumstantial; that is, a carbonate-rich quench between crystals in the crystal-rich portion of the capsule is interpreted to represent a carbonatite melt, whereas the silicate melt is well separated into a crystal-poor portion of the capsule. The interpretation of such a texture as being indicative of two coexisting melts will be discussed below.

Major element compositions of the H_2O-bearing melts

Melt compositions for experiments in the H_2O-bearing systems are given in Table 5 and plotted in Figs 2, 3b and 4b. In this series, a single or a few large silicate melt blobs formed within the carbonatite melt (Fig. 5a–e). As phase separation in the H_2O-bearing experiments was complete, homogeneous conjugate melts could be analyzed by large area laser ablation without centrifugation. Additionally, several experiments contain large spherical voids, interpreted as bubbles of $CO_2 + H_2O$-fluids coexisting with the two melts (Figs 5a, d and e).

The silica-undersaturated potassic H_2O-bearing systems

We performed four successful experiments (Table 2) with starting materials KF6 containing 2 wt % H_2O and KF5 and KF8 containing 4 wt % H_2O (Table 1). Experiment LM82, run with KF6 in $Au_{80}Pd_{20}$ at 1·7 GPa, 1200°C, produced silicate and carbonatite liquids, vapor bubbles, and small phlogopite crystals at the bottom of the charge (Fig. 5a). The compositional gap between the conjugate melts of experiment LM82 (Fig. 2) ranges from 42·8 to 9·9 wt % SiO_2, 10·0 to 22·3 wt % CaO, and 0·47 to 0·59 Ca/(Ca + Mg + Fe), respectively. The silicate melt has 2·1 wt % Na_2O and 14·0 wt % K_2O, whereas the carbonatite melt has alkali contents of 2·5 wt % Na_2O and 11·5 wt % K_2O. This miscibility gap is slightly wider than for anhydrous experiments LM45 and LM54, indicating that H_2O enlargens the miscibility gap (Fig. 4b). The SiO_2 and Al_2O_3 contents of the carbonatites in the H_2O-bearing systems are slightly higher than in the anhydrous potassic system.

Experiment LM75 (Fig. 5b), with 4 wt % H_2O, $Fe^{3+}/Fe^{tot} = 0·58$ (starting material KF5; Table 1), was run in $Au_{80}Pd_{20}$ at 1·7 GPa, 1150°C and yielded two conjugate melts. Experiment LM113, with all Fe as Fe^{2+} (starting material KF8), run at the same run conditions, additionally yielded large bubbles and phlogopite. The silicate melt compositions of these experiments (Table 5) compare well and have ~48 wt % SiO_2, ~7·5 wt % CaO, and alkali contents of 2·2 wt % Na_2O and ~15 wt % K_2O. These melts are more Si- and Al-rich than those of the 2 wt % H_2O experiment (LM82; Fig. 5a), but are poorer in Ca, Mg and Fe. The 4 wt % bulk H_2O carbonatite melts have slightly more Si, Al and Ca than those of the 2 wt % bulk H_2O and the dry experiments (LM82, LM45 and LM54), and contain ~11 wt % SiO_2, ~25 wt % CaO, ~2·5 wt % Na_2O and ~7·9 wt % K_2O. The result is a wider miscibility gap in SiO_2 from 48·4 to 11·9 wt %, in CaO from 6·7 to 23·9 wt %, and from 0·50 to 0·60 molar Ca/(Ca + Mg + Fe) (Figs 2, 3b and 4b). Although experiments LM75 and LM113 had different initial Fe^{3+}/Fe^{tot} ratios, the iron contents of the conjugate melts show little variation.

Table 7: Average trace element melt compositions (in ppm, apart from spike, in wt %) measured by LA-ICP-MS

Experiment:	Spike	LM22	LM22	LM36	LM36	LM52	LM52	LM58	LM58	LM51	LM51	LM45	LM45	LM54	LM54	LM108	LM108
No. of analyses:*		6	7	5	5	6	5	6	7	5	6	6	7	6	7	6	6
Melt:		LS	LC	LS	LC	LS	LC	LS	LC	LS	LC	LS	LC	LS	LC	LS	LC
Cs	0·72	34·3(10)	77(3)	27·2(11)	80·6(22)	63·1(4)	143(6)	57·7(4)	136(12)	59·5(5)	147(7)	39·9(6)	40·7(24)	66·8(11)	79(3)	116·2(17)	110(6)
Rb	0·22	6·6(1)	11·6(3)	6·5(1)	15·2(3)	10·1(2)	17·9(5)	12·0(2)	19·5(16)	147·2(2)	19·5(4)	9·4(2)	9·3(4)	11·5(3)	12·8(5)	22·4(3)	20·7(12)
Li	0·59	18·2(7)	21·5(6)	12·8(4)	20·1(4)	29·2(4)	39·3(28)	28·6(4)	38(4)	28·2(11)	41·9(17)	26·3(7)	31·8(21)	24·1(6)	34·8(17)	37·8(10)	63(4)
Ba	1·20	40·9(6)	58·5(21)	26·1(5)	48·9(11)	56·5(10)	92(5)	45·9(8)	92(7)	52·0(5)	92(4)	45·8(9)	71·0(22)	42·0(9)	73·7(21)	69·5(24)	161(9)
Sr	1·17	39·0(4)	53·9(11)	31·0(2)	57·0(7)	48·6(6)	78·0(14)	48·7(7)	78(6)	46·6(5)	84·6(9)	51·3(9)	87·7(14)	45·7(4)	89·6(14)	69·2(29)	186(5)
Be	1·17	84 (4)	11·2(29)	74(4)	9·0(26)	130(4)	14(3)	132(4)	24(6)	109(4)	19(5)	93·1(21)	32·3(15)	81·4(23)	29·7(13)	187(7)	79(4)
Pb	0·22	0·04(1)	0·02(1)	0·10(4)	0·03(1)	0·87(4)	0·39(3)	0·10(3)	0·03(1)	0·61(5)	0·32(1)	1·17(5)	0·80(4)	1·18(6)	0·96(4)	0·47(5)	0·45(2)
P		42·1(8)	65·1(22)	424·4(19)	80·7(13)	40·6(18)	72·1(16)	52·5(17)	85(8)	933(48)	3099(77)	2432(52)	6379(403)	2100(530)	7420(461)	327(20)	1067(23)
Th	0·22	19·3(10)	1·8(4)	15·9(13)	1·5(6)	24·8(14)	2·1(7)	22·0(5)	4·8(1)	24·0(12)	3·5(9)	19·1(2)	8·0(1)	15·0(1)	7·1(1)	35·6(12)	21·1(8)
U	0·22	16·2(6)	3·4(5)	11·9(7)	4·4(6)	20·5(11)	6·3(7)	18·7(3)	7·1(11)	17·4(7)	7·5(9)	17·0(4)	10·5(4)	13·9(2)	10·6(3)	29·0(9)	23·7(9)
Hf	1·16	82·1(22)	4·3(12)	73(5)	3·1(15)	116(3)	4·8(22)	101(3)	10·3(28)	105(6)	7·5(28)	93·7(14)	19·0(6)	79·0(16)	17·0(7)	201(5)	40·2(12)
Zr	1·18	95(4)	6·7(18)	82(6)	4·7(22)	126(3)	7(3)	132(4)	15(4)	109(6)	10(3)	100·4(11)	25·8(8)	80·7(10)	22·2(9)	206(7)	53·8(17)
Nb	1·17	118(7)	46(4)	127(8)	56(7)	175(9)	65(7)	185·5(24)	92(12)	148(4)	77(9)	130(17)	82·0(26)	113·0(11)	82·3(17)	292(11)	195(9)
Ta	1·36	0·15(3)	0·03(1)	0·15(2)	0·03(1)	0·12(1)	0·020(4)	0·13(1)	0·03(1)	0·22(2)	0·06(1)	0·69(2)	0·28(2)	0·57(2)	0·26(2)	0·07(2)	b.d.
Mo	1·18	11·2(5)	65(5)	7·3(7)	62(3)	17·3(4)	117(7)	23·2(6)	119(8)	28·4(24)	167(11)	23·1(4)	86(6)	19·2(5)	90(5)	44·2(24)	214(118)
La	1·23	52·3(23)	24·6(13)	47·0(21)	29·3(18)	72·0(19)	42·0(17)	60·5(5)	54(5)	63·5(9)	46·6(29)	44·3(15)	53·4(12)	38·3(5)	52·9(8)	53(3)	114(6)
Ce	0·49	50·0(20)	20·0(13)	45·0(17)	23·1(16)	67·6(20)	32·5(18)	56·8(6)	45(5)	57·6(10)	36·1(26)	41·3(4)	44·7(10)	36·0(2)	44·6(6)	53·8(27)	100(4)
Pr	0·49	42·4(20)	16·6(10)	38·4(18)	19·2(14)	58·2(19)	27·3(16)	49·9(4)	38(4)	50·2(7)	30·8(24)	36·0(4)	38·3(7)	30·3(5)	37·2(8)	47·3(28)	88(3)
Nd	0·49	47·5(28)	18·3(11)	44·2(28)	21·7(15)	67·2(21)	31·2(20)	57·6(11)	43(4)	57·7(9)	35·2(25)	39·4(9)	41·6(8)	35·2(5)	41·9(9)	50·6(25)	90(4)
Sm	1·15	60·0(24)	20·9(17)	55·3(29)	24·4(21)	83·7(24)	35·4(24)	71·3(10)	50(5)	71·7(18)	40(3)	51·1(9)	49·9(12)	45·6(7)	51·1(14)	66·7(29)	110(5)
Eu	0·50	51·8(19)	22·8(12)	49·3(25)	20·8(20)	76·1(23)	31·0(24)	60·6(7)	49(5)	65·1(13)	35·6(29)	46·6(6)	45·1(9)	40·6(5)	44·5(8)	59·5(28)	96(3)
Gd	0·50	51·2(24)	17·9(16)	46·7(23)	19·9(19)	71·1(14)	29·5(25)	61·5(6)	41(4)	62·5(17)	34·0(29)	44·2(18)	42·8(10)	39·8(4)	43·8(12)	63·4(25)	101(4)
Tb	0·50	52·5(19)	16·6(16)	43·6(25)	16·7(19)	67·5(19)	25·2(22)	59·3(11)	36(4)	59·1(10)	29·5(27)	44·5(8)	40·7(7)	37·1(3)	38·9(8)	58(3)	89(4)
Dy	1·17	66·1(24)	20·0(20)	59(3)	20·9(24)	90·2(19)	32·0(30)	78·0(20)	46(5)	79·7(14)	38(4)	57·7(6)	50·7(14)	50·4(5)	50·6(12)	79(5)	114(5)
Er	0·50	58·2(23)	16·3(18)	48·5(28)	15·4(21)	76·6(13)	24·5(27)	65·6(15)	35(4)	69·8(16)	30(3)	49·3(6)	41·1(14)	43·7(6)	41·0(7)	73(4)	97(4)
Yb	1·20	79·0(20)	18·5(25)	65(4)	17·4(29)	103·9(29)	28(4)	89·8(21)	42(5)	92·8(20)	34(4)	67·3(14)	50·2(11)	59·7(8)	50·3(10)	94(5)	110(5)
Lu	1·17	69·7(16)	16·4(22)	55(4)	14·2(25)	88·7(21)	23(4)	78·0)18)	35(5)	79·4(18)	29(4)	61·8(11)	45·3(10)	51·0(4)	42·8(7)	88(4)	104(4)
Y	1·00	66·4(23)	21·4(20)	54(3)	20·2(24)	81·8(17)	30·4(29)	83·3(17)	42(4)	72·6(17)	36(3)	50·5(5)	46·5(15)	44·8(5)	46·1(8)	69(4)	104(4)
Sc	1·15	76·5(28)	10·9(22)	71(6)	9·7(28)	109(3)	15(4)	114·0(18)	28(5)	96(4)	20(4)	73·0(14)	35·5(8)	65·5(9)	34·6(6)	96(5)	63·7(18)
V	1·17	41·5(18)	46·8(17)	25·7(19)	52·6(23)	52·0(17)	85(5)	70·7(8)	68(6)	48·3(9)	84(5)	49·1(7)	607(33)	44·1(6)	65·6(27)	84(3)	125(5)
Cr	1·16	13·4(14)	3·9(5)	5·7(24)	1·3(2)	229(12)	28(9)	540(8)	170(31)	25·7(18)	5·4(12)	205(5)	96·1(14)	188(4)	96·1(21)	6·9(12)	4·8(7)
Mn	0·89	13·2(4)	4·8(3)	80(3)	35·1(27)	58·3(16)	23·8(16)	4·6(1)	2·5(2)	55·1(16)	29·5(25)	54·4(11)	44·1(14)	49·8(4)	45·6(14)	65·9(23)	74·3(17)
Co	1·20	n.a.	n.a.	21·4(12)	6·7(9)	43·4(11)	12·9(14)	0·7(1)	0·33(2)	29·0(8)	11·7(11)	35·4(8)	22·9(9)	41·6(3)	30·9(7)	62·2(27)	54·1(21)
Cu	–	0·39(4)	0·12(3)	2·0(1)	3·0(1)	2·5(1)	3·0(2)	1·9(1)	2·7(2)	2·1(1)	3·2(2)	n.a.	n.a.	0·7(1)	0·63(4)	0·4(1)	0·3(0)
Zn	1·19	1·2(3)	0·2(1)	25·3(18)	4·3(8)	52·3(23)	7·8(2·5)	1·9(2)	0·5(2)	35·1(24)	7·1(8)	38·3(12)	16·8(9)	59·9(26)	31·1(21)	48·8(25)	29·2(8)
Ga	1·15	1·7(1)	0·6(0)	29·7(28)	1·7(5)	90·7(46)	4·1(14)	1·9(1)	0·9(1)	72(6)	6·0(18)	57·1(7)	10·6(3)	68·6(10)	13·4(6)	103·7(16)	18·6(8)
Ge	1·17	2·9(3)	1·1(2)	17·4(16)	3·0(5)	85·5(13)	11·4(22)	2·8(3)	1·8(2)	64·6(28)	14·1(24)	31·2(13)	11·2(2)	45·9(14)	15·9(7)	36·6(24)	13·6(8)

(continued)

Table 7: Continued

Experiment:	LM59	LM59	LM82	LM82	LM75	LM75	LM113	LM113	LM63	LM63	LM73	LM73	LM83	LM83	LM101	LM101
No. of analyses:*	6	7	6	7	6	7	5	5	6	7	6	7	7	8	7	7
Melt:	LS	LC	LS	LC	LS	LC	LS	LC	LS	LC	LS	LC	LS	LC	LS	LC
Cs	57·8(14)	177(6)	154·0(30)	100(9)	194(4)	102(8)	381(9)	234(18)	250(10)	48(5)	166(5)	84(4)	146(39)	71(8)	177(5)	64(4)
Rb	10·5(3)	23·5(4)	22·7(6)	15·6(10)	27·5(6)	16·3(5)	44·9(7)	28·7(17)	30·2(10)	12·5(6)	23·8(6)	14·2(5)	22·5(12)	13·3(9)	23·6(4)	13·2(11)
Li	36·9(9)	52·3(13)	32·2(9)	46(5)	31·7(13)	48·4(26)	54·8(16)	130(19)	26·1(25)	56(4)	20·5(13)	67(4)	15·5(17)	83(12)	20·5(13)	82(4)
Ba	68·0(20)	105·8(22)	57·6(10)	103(6)	49·1(6)	114(6)	81·4(14)	256(5)	31·6(6)	127(4)	22·2(4)	179(5)	16(5)	239(10)	18·4(3)	241(5)
Sr	63·9(17)	97·4(14)	61·7(10)	132·0(16)	42·0(4)	120·0(16)	64·9(8)	272(4)	24·1(3)	146·6(22)	12·7(1)	186·7(25)	9·3(15)	246(4)	11·5(2)	250(4)
Be	147(5)	27(6)	128(5)	59(6)	117(5)	72(4)	245(8)	178(17)	149(7)	75(4)	95(4)	83(5)	111(21)	43·2(18)	131(4)	46(3)
Pb	0·04(1)	0·018(4)	1·84(12)	1·9(2)	0·76(6)	1·02(6)	2·09(4)	3·80(7)	0·49(3)	0·83(13)	2·19(19)	9·9(3)	0·48(14)	1·30(5)	1·14(7)	4·4(4)
P	734(23)	2302(131)	42·0(12)	49(3)	1245(25)	6201(447)	176(4)	1192(52)	579(24)	7791(322)	172·7(24)	1153(32)	34(4)	62(4)	29·6(21)	36·7(16)
Th	33·8(6)	4·8(14)	23·3(4)	16·5(16)	18·1(2)	19·6(26)	34·0(8)	46(11)	17·2(2)	24·1(8)	5·5(1)	36·6(12)	13·1(24)	28·1(19)	15·5(4)	28·3(27)
U	26·4(4)	8·1(14)	22·1(7)	18·3(15)	16·9(2)	18(4)	30·8(3)	33(13)	17·3(6)	22·6(9)	8·5(3)	28·8(10)	16·6(26)	20·6(11)	19·5(4)	20·5(16)
Hf	147·8(23)	12(4)	141(4)	36·4(13)	160·0(24)	54·0(20)	315(7)	99(5)	222·7(23)	37·4(9)	111·8(19)	36·6(12)	120(26)	7·2(3)	137·7(3)	8·5(1)
Zr	158·2(25)	18(6)	141(4)	46·1(18)	137·5(18)	60(3)	290(6)	120(8)	190·7(8)	49·4(10)	103·8(18)	58·4(21)	113(25)	14·0(4)	129·2(26)	15·8(2)
Nb	195(5)	120(13)	195·3(20)	137·6(14)	170·7(18)	172·0	332(4)	385(26)	174(4)	177(5)	177(4)	190(7)	191(38)	117(5)	231(6)	117(5)
Ta	0·20(2)	0·06(2)	0·43(4)	0·18(2)	0·34(2)	0·18(1)	0·03(1)	0·011(3)	0·41(4)	0·17(1)	0·03(1)	0·012(6)	0·03(1)	b.d.	0·028(4)	b.d.
Mo	22·0(6)	190(11)	44·8(14)	143·1(215)	29·6(11)	120(18)	47·4(3)	308(55)	14·9(9)	117(6)	19·2(7)	170(7)	32(6)	189(23)	32·7(12)	185(27)
La	93·7(16)	53(4)	40·8(6)	82(2)	28·1(4)	95·2(24)	45·1(10)	230(3)	13·6(1)	112·4(13)	4·2(1)	160(3)	6·5(5)	191·1(29)	8·0(1)	209(2)
Ce	84·9(12)	42(4)	40·5(8)	73·4(15)	27·2(5)	81·4(25)	44·8(6)	203(4)	14·0(3)	97·7(12)	4·5(1)	136·9(25)	7·2(4)	177(4)	8·8(2)	177·1(20)
Pr	73·7(12)	35(3)	36·1(3)	65·0(14)	24·4(2)	70·9(19)	39·8(6)	181·0(29)	12·6(2)	85·6(7)	4·1(1)	128·0(26)	6·6(4)	151·8(18)	8·3(1)	163·7(25)
Nd	84·1(13)	40(4)	38·3(4)	66·2(13)	25·7(4)	72·7(15)	44·0(6)	180·2(28)	13·4(4)	86·6(12)	4·4(2)	127·3(17)	7·1(3)	147·5(14)	9·1(3)	159·0(19)
Sm	107·3(15)	48(5)	51·4(10)	83·6(16)	34·8(4)	91·4(16)	61·1(9)	230·2(30)	19·2(1)	109·4(10)	6·1(2)	161·1(18)	10·8(8)	185·8(21)	13·8(4)	198·6(26)
Eu	87·3(12)	51(4)	45·7(7)	72·2(18)	31·2(4)	79·1(13)	53·9(11)	202(4)	17·5(3)	95·6(11)	5·8(1)	142·4(24)	10·2(7)	163·6(18)	13·1(3)	174·7(26)
Gd	93·9(19)	40(4)	49·1(14)	78·2(18)	33·0(4)	83·9(11)	56·8(12)	208(4)	18·6(3)	102·0(14)	5·9(2)	151·3(11)	11·4(10)	170·8(23)	14·3(3)	185·1(20)
Tb	90·2(16)	36(4)	45·6(8)	70·2(16)	31·1(4)	76·2(12)	54·2(15)	198(3)	18·2(2)	92·9(8)	5·9(4)	144·6(22)	11·4(10)	162·0(13)	14·6(3)	175·6(15)
Dy	119·0(13)	46(6)	61·0(17)	89·5(24)	42·7(6)	98·2(16)	76·3(15)	248(5)	25·8(4)	117·9(15)	8·3(3)	177·3(26)	17·0(18)	200·0(25)	21·3(7)	211·1(25)
Er	110·6(13)	36(5)	58·6(15)	78·4(18)	39·9(5)	85·1(17)	70·7(24)	208(5)	25·2(5)	102·6(5)	8·4(2)	157·1(22)	17·4(22)	167·5(22)	22·7(5)	180·7(24)
Yb	134·7(23)	42(7)	71·8(19)	88·3(25)	51·4(9)	97·6(25)	94·0(26)	236(9)	35·7(10)	119·4(14)	11·8(2)	179·3(21)	26(3)	187·3(24)	33·1(9)	196·3(14)
Lu	118·7(20)	16(6)	67·4(23)	82·2(21)	47·6(5)	89·9(24)	91·0(20)	231(12)	33·2(2)	111·9(13)	11·6(2)	179(3)	26(4)	188·3(20)	32·3(9)	188·6(19)
Y	104·0(18)	41(5)	51·2(13)	76·6(16)	38·0(4)	86·6(17)	66·8(16)	221(4)	23·6(2)	110·0(13)	7·3(1)	162·6(25)	14·8(18)	177·3(24)	19·1(4)	190·7(24)
Sc	134·0(15)	27(6)	90·9(14)	68·2(16)	76·0(6)	83·5(26)	141·2(22)	182(10)	67·5(14)	89·7(19)	30·3(2)	151·3(14)	58(10)	111·3(18)	73·1(9)	117·7(25)
V	64·0(12)	94·2(23)	74·3(17)	86·6(24)	65·7(12)	92(4)	104·6(15)	181(12)	46·9(12)	79·4(28)	47·2(12)	128(3)	64(10)	111(6)	78·1(20)	114(6)
Cr	38·8(12)	11·6(27)	58·6(28)	41·0(12)	56·7(18)	69(4)	21·4(9)	25·3(10)	8·3(6)	10·8(8)	36·3(7)	154·0(24)	59(9)	118(5)	75·5(29)	127·7(26)
Mn	3·7(1)	1·7(1)	60·7(13)	70·8(24)	42·2(6)	70·7(22)	62·2(12)	136·4(27)	29·0(6)	76·7(15)	14·5(3)	105·6(17)	205(28)	1643(26)	306(5)	1689(21)
Co	0·58(3)	0·19(4)	47·9(13)	46·0(11)	33·2(3)	45·7(16)	64·9(4)	110·8(18)	18·5(6)	36·3(10)	22·2(7)	126·3(26)	19·2(29)	94(5)	33·4(12)	118·9(28)
Cu	1·1(1)	1·6(1)	0·49(9)	0·36(3)	0·30(8)	0·26(3)	0·4(1)	0·4(1)	0·28(8)	0·26(2)	0·31(7)	0·44(3)	0·73(8)	0·48(6)	0·3(1)	0·5(0)
Zn	1·8(3)	0·5(1)	37·2(7)	27·9(25)	25·1(6)	26·2(15)	42·5(10)	53·3(21)	34·8(10)	39·2(17)	31·7(7)	85·7(131)	12·8(24)	28·4(23)	36·3(11)	55(5)
Ga	2·7(2)	1·0(1)	124·8(19)	29·6(7)	120·5(15)	39(11)	256·8(26)	68·6(18)	113(5)	17·7(8)	124(3)	25·0(9)	111(7)	10·6(4)	129(3)	12·4(3)
Ge	3·8(2)	1·8(1)	68·8(19)	23·8(9)	29·0(15)	13·6(8)	104·4(11)	46·5(6)	18·3(12)	8·2(3)	106(3)	15·6(5)	13(8)	9·0(7)	28·2(13)	11·1(6)

LC, quenched carbonatite melt, LS, silicate melt. Partition coefficients D^i calculated on a weight-basis; errors are 1σ errors; n.a., not analyzed; b.d., below detection limit.
*Number of averaged analyses. Weight fraction of added trace element spike is in Table 1.

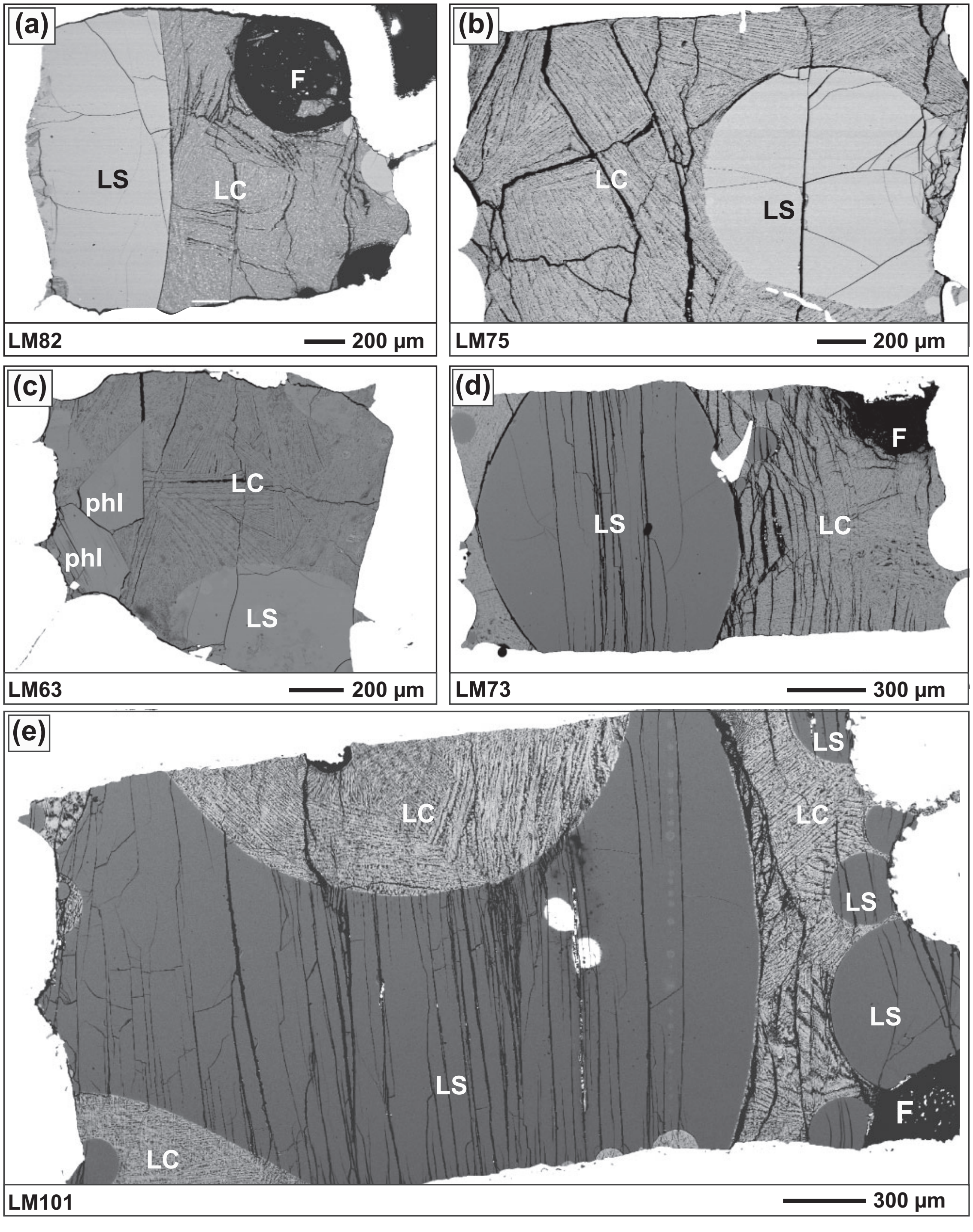

Fig. 5. Backscattered electron images of experiments from the H_2O-bearing systems, which resulted in a near-perfect phase separation in static experiments. (a) Perfectly separated silicate glass and carbonatite melt quench with small phlogopite crystals. The larger spherical voids are interpreted as equilibrium bubbles of a $CO_2 + H_2O$ fluid. Texturally these large bubbles are distinct from micron-sized quench bubbles in the silicate glass (LM82, 1·7 GPa, 1150°C, 1·9 wt % H_2O). (b) Large silicate melt glass blob within quenched carbonatite melt (LM75, 1·7 GPa, 1150°C, 3·9 wt % H_2O). (c) A large silicate glass blob within quenched carbonatite melt containing additional phlogopite crystals (LM63, 1·7 GPa, 1150°C, 3·9 wt % H_2O). (d) Large phonolitic glass blob within quenched carbonatite melt with a bubble interpreted as a coexisting fluid (LM73, 3 GPa, 1160°C, 2 wt % H_2O). The bright spot within the charge is a fragment of the capsule alloy. (e) Experiment LM101 (3 GPa, 1160°C, 2 wt % H_2O) with several large silicate melt droplets within the carbonatite melt and carbonatite droplets attached to the capsule wall within the silicate melt. The two bright spots in the silicate melt are an artefact of electrical charging. It should be noted that in the Si-rich bulk compositions (c) and (e), the silicate glasses have a lower backscatter brightness than the carbonatite melt quench. LC, quenched carbonatite melt; LS, quenched silicate glass; phl, phlogopite crystals; F, fluid.

Experiment LM63 (Fig. 5c), which had the same nominal conditions and starting material (KF5) as LM75, contains large phlogopite crystals, which may indicate a slightly lower run temperature for LM63 than LM75. The crystallization of phlogopite resulted in higher Si and Al contents in the silicate melt (53·6 wt % SiO_2), and in lower CaO (3·8 wt %). Alkali contents are 2·1 wt % Na_2O and 15·9 wt % K_2O for the silicate melt. The carbonatite melt has the lowest silica and alumina content of the H_2O-bearing series, but the highest CaO content with 5·7 wt % SiO_2, 28·2 wt % CaO, and alkali contents of 2·1 wt % Na_2O and 8·9 wt % K_2O. In this series, LM63 yields the widest miscibiity gap in SiO_2 (from 53·6 to 5·7 wt %), Al_2O_3, and CaO (3·8 to 28·2 wt %), and Ca/(Ca + Mg + Fe) of 0·44–0·65 (Figs 2 and 4b). With increasing width of the miscibility gap, the silicate melt becomes richer in SiO_2 and Al_2O_3, but poorer in CaO and MgO, resulting in increased polymerization of the silicate melt in terms of Non-bridging oxygen per tetrahedra (NBO/T) (Table 5; see also Hamilton *et al.*, 1989).

The H_2O-bearing phonolitic system

A bulk composition representing a 50:50 mixture of the conjugate phonolite and carbonatite melts (Table 1, ThS-1) of Thomsen & Schmidt (2008), obtained from the melting of a quartz + kyanite-saturated carbonated pelite at 3·7 GPa, did not yield liquid immiscibility at 3·0 GPa, 1100°C (experiment LM62; Table 3; back-scattered electron images in the Electronic Appendix). The Thomsen & Schmidt (2008) immiscible melts yield a bulk K_2O of 5·9 wt % for a 50:50 weight mixture. We had to increase the bulk K_2O content to 14 wt % to obtain liquid immiscibility (Tables 2 and 3), and to lower the SiO_2 content of the silicate melt (55·4 wt % compared with ~60 wt % SiO_2 in the original study). The bulk water content of this system was set to 2 wt %, a concentration derived from the bulk H_2O and melt fraction of Thomsen & Schmidt (2008).

The phonolite system starting material (ThS3B, Table 1) has significantly higher bulk SiO_2 (30 wt %) and Al_2O_3 (11·8 wt %) contents than the silica-undersaturated systems. Experiment LM73 was run at 3 GPa, 1160°C, resulting in immiscible silicate and carbonatite melts and large bubbles interpreted as a coexisting fluid (Fig. 5d). The silicate melt contains 55·4 wt % SiO_2, 1·6 wt % CaO, 3·4 wt % Na_2O and 16·2 wt % K_2O. The carbonatite melt contains ~1·5 wt % SiO_2, 25·4 wt % CaO, 6·5 wt % Na_2O and 12·1 wt % K_2O. The miscibility gap has one of the largest spans, in Al_2O_3 from 21·1 to 1·5 wt %, 1·6 to 25·4 CaO, and 0·47 to 0·74 molar Ca/(Ca + Mg + Fe) (Figs 2 and 3b). Coesite + kyanite saturation was not reached and therefore our melt compositions differ from those of Thomsen & Schmidt (2008).

The H_2O-bearing trachytic system

The starting material ThS4 (Table 1) was designed to produce silica-rich immiscible melts closer to those of Thomsen & Schmidt (2008). Together with the silica-undersaturated potassic system, this approach allows isolation of the effect of silica and silicate melt polymerization on partition coefficients. Thus, composition ThS4 contained ~10 wt % SiO_2 more than that of the phonolite system (ThS3B). Experiments LM83 and LM101 were run at 3 GPa, 1160°C, yielding silicate and carbonatite melts as well as bubbles. The silicate melts contain ~68 wt % SiO_2, ~1·3 wt % CaO, ~3·9 wt % Na_2O and ~11·7 wt % K_2O. These melts are comparable with the kyanite + coesite-saturated immiscible melts from Thomsen & Schmidt (2008), except that their silicate melts had 20 wt % Al_2O_3 in contrast to 11 wt % in our kyanite-undersaturated melts (Table 4). Owing to their low Al contents, these melts have NBO/T of 0·2, which is higher than the NBO/T of 0·12 for the silica-poorer phonolitic melt of LM73 (Table 4). The carbonatite melts of LM83 and LM101 contain ~2 wt % SiO_2, ~27 wt % CaO, ~9 wt % Na_2O and ~8·6 wt % K_2O. The calcium–sodium–potassium carbonatite melt is slightly richer in silica, poorer in alumina and contains significantly more alkalis than that of Thomsen & Schmidt (2008), with 2·6–4 wt % Na_2O and 0·7 wt % K_2O. As detailed above, we suggest that alkalis and H_2O were lost from the small carbonatite blobs of Thomsen & Schmidt (2008) during sample preparation. This trachytic system yields the largest miscible gap of this study, from 67·6 to 2·5 wt % SiO_2, 1·4 to 26·6 wt % CaO, and 0·34 to 0·76 molar Ca/(Ca + Mg + Fe) (Figs 2 and 3b).

Summary of the melt composition of the conjugate melts

The compositions of the conjugate melts and the width of the miscibility gap in the anhydrous systems are largely comparable (Tables 3 and 5; Figs 2a, 3 and 4a), with the exception of K_2O and Na_2O contents and ratios. Carbonatite melts in the potassic system contain up to 10 wt % SiO_2 at conditions that allow only ~5 wt % SiO_2 in the sodic system. Na_2O and K_2O partition into the carbonatite melt for all dry systems.

In the H_2O-bearing systems, increasing amounts of H_2O result in an increase of the miscibility gap width (Tables 4 and 5, Fig. 3b) for the strongly silica-undersaturated systems. Similar, increasing bulk SiO_2 from the strongly silica-undersaturated compositions to those with phonolitic and trachytic silicate melts (at 2 wt % bulk H_2O) leads to an increased miscibility gap width and, as shown below, to an increase in trace element partition coefficients. Whereas Na_2O still partitions into the carbonatite melt, K_2O partitions into the silicate melt in all H_2O-bearing potassic systems, leading to a net partitioning of total alkalis into the silicate melt in the potassic silica-undersaturated H_2O-bearing systems. In all systems, X_{Mg} in the carbonatite melt is >0·06 higher than in the silicate melt, similar to carbonate minerals, which tend to have a higher X_{Mg} than coexisting silicates.

Large voids interpreted as previously fluid-filled bubbles were detected in many anhydrous and H_2O-bearing experiments (Tables 2 and 3, Fig. 5); however, their absence could also result from them being present at a different level than exposed. An absence of fluid bubbles would reflect fluid undersaturation and we have no means to quantify the activities of CO_2 (and H_2O) in the melts. The influence of fluid saturation on the width of the miscibility gap (e.g. Brooker & Kjarsgaard, 2011) can thus not be constrained here; however, the systematics of the major and trace element partitioning indicates that fluid saturation was a minor variable in this study.

Trace element partition coefficients in the anhydrous systems

Major and trace element concentrations for the melts in the anhydrous systems are given in Tables 4, 6 and 7. The partition coefficients (Table 8) are Nernst partition coefficients $D^i = C^{\text{carbonatite}}/C^{\text{silicate melt}}$ calculated from weight concentrations. In Fig. 6, partition coefficients are plotted chemically grouped into alkali, alkaline earth, high field strength elements (HFSE), the rare earth elements (REE), which include Sc and Y, the third row transition metals V to Zn (TM) and network formers (Al, Ga, Si, Ge). As a first-order observation, the partition coefficients patterns of all anhydrous systems are similar (Fig. 6a), except for the alkali elements, Cu and Ga. Second, most partition coefficients are within a factor of five of unity, except for Mo, which partitions more strongly into the carbonatite melt, and for Be, some HFSE, Sc and the network formers, which partition more strongly into the silicate melt (Fig. 6a).

To understand the systematics of partition coefficients, D values are plotted (Fig. 7) against ionic potential (charge/ionic radius; Z/r), a proxy for the strength of ionic bonding or electrostatic repulsion between network modifying cations in melts (Hudon & Baker, 2002).

For the sodic and alkalic systems (Fig. 7a and b), the carbonatite/silicate melt partition coefficients for the alkalis and alkaline earths Ba–Ca decrease with increasing ionic potential from D ~3 for Cs to near unity for Ca. Somewhat contrasting, the alkali and alkaline earth D values of the potassic systems (Fig. 7c) increase with increasing bond strength from near unity to 2–2·5 for Ca. Interestingly, the carbonatite/silicate melt partition coefficients determined by Veksler *et al.* (2012) for a system reproducing an Mg-poor Oldingyo Lengai composition with $K_2O/Na_2O = 0{\cdot}4$ are consistent with our potassic system, but not with the alkaline or sodic system (Fig. 6c).

The high field strength elements P and Mo (Fig. 8c) partition most strongly into the carbonatite melt ($D^{P} = 1{\cdot}5$–$3{\cdot}5$, $D^{Mo} = 3{\cdot}7$–$8{\cdot}7$), similar to the observation of Veksler *et al.* (2012). The other high field strength elements Th, U, Hf, Zr, Ti, Nb, Ta and Sc partition into the silicate melt (Fig. 7), Zr and Hf having the lowest partition coefficients ($D^{Zr} = 0{\cdot}06$–$0{\cdot}28$, $D^{Hf} = 0{\cdot}04$–$0{\cdot}22$). Fractionation of geochemical pairs such as Zr/Hf and Nb/Ta is generally strong, with $D^{Nb/Ta} = 1{\cdot}6$–$2{\cdot}8$ and $D^{Zr/Hf}$ between 1·3 and 1·5 (Table 8). As the dry experiments resulted in comparable miscibility gap widths (Figs 3a and 4a), no systematic trends occur; for example, for $D^{Zr/Hf}$ of the anhydrous systems as a function of the molar $(Si + Ti + Al)/(Si + Ti + Al + Fe + Mg + Ca + Na + K)$ ratio of the silicate melt.

Surprisingly, the REE do not generally favour the carbonatite melt, as one would expect from the fact that some carbonatites are exploited as REE deposits. Instead, the REE have very modest partition coefficients, decreasing from La to Lu ($D^{La} = 0{\cdot}5$–$0{\cdot}9$ and $D^{Lu} = 0{\cdot}2$–$0{\cdot}4$ for the sodic and alkalic systems; $D^{La} = 1{\cdot}4$–$2{\cdot}2$ and $D^{Lu} = 0{\cdot}7$–$1{\cdot}2$ for the potassic system), with $D^{La/Lu} = 1{\cdot}6$–$2{\cdot}5$. The REE form linear trends (Figs 7 and 8a, b) only in the reducing experiments with graphite (LM22, LM58, LM59), with an estimated f_{O2} of IW ± 0·5. D^{Eu} forms a positive anomaly (Fig. 6a), indicating a more reduced valence state for Eu in these experiments.

The third row transition metals Cr, Mn, Fe, Co, Cu and Zn partition into the silicate melt with D values ranging from 0·2 to 0·9, except for Cu in the sodic and alkalic systems with $D^{Cu} = 1{\cdot}2$–$1{\cdot}5$. V partitions into the carbonatite melt in all anhydrous systems ($D^{V} = 1$–2). Surprisingly, although experiment LM108 was performed at a lower f_{O2} than experiments LM45 and LM54, no difference in the behaviour of the third row transition metals can be observed, indicating that variations in oxygen fugacity have little influence on the partition coefficients for anhydrous systems.

The amphoteric elements Be, Zn, Pb, Al, Ga, Si and Ge all preferentially partition into the silicate melt (Fig. 6). The network formers, and in particular the major element Al, have low distribution coefficients ($D^{Al} = 0{\cdot}03$–$0{\cdot}12$), followed by Ga ($D^{Ga} = 0{\cdot}05$–$0{\cdot}38$) and Si ($D^{Si} = 0{\cdot}09$–$0{\cdot}25$).

Trace element partition coefficients in the H_2O-bearing potassic systems

Major and trace element concentrations in the H_2O-bearing melts are listed in Tables 5 and 7, and calculated partition coefficients in Table 9. The partition coefficients in the H_2O-bearing potassic systems show similar patterns to those of the anhydrous potassic systems (Figs 6b and 7d) but have higher magnitudes; that is, a D^{La}/D^{Hf} of 7·7–490 (with $D^{Hf} = 0{\cdot}06$–$0{\cdot}34$ and $D^{La} = 2{\cdot}0$–$38{\cdot}0$) in comparison with the anhydrous system with $D^{La}/D^{Hf} = 6$–11 ($D^{Hf} = 0{\cdot}04$–$0{\cdot}22$; $D^{La} = 1{\cdot}47$–$1{\cdot}38$). Also, the patterns are generally shifted in favour of the carbonatite melts (Fig. 6b).

Table 8: Partition coefficients for the anhydrous systems

Experiment:	LM22	LM36	LM52	LM58	LM51	LM45	LM54	LM108	LM59
Starting material:	Mix1-B	Mix1-B	Mix1-E	Mix1-C	Mix1-D	KF4	KF4	KF7	Alk1
P (GPa)/*T* (°C):	1/1240	1/1240	1/1240	1·7/1260	1/1240	1·7/1220	1·7/1220	1·7/1220	1/1240
Major elements									
SiO_2	0·10(2)	0·12(5)	0·09(2)	0·10(6)	0·11(6)	0·25(6)	0·22(4)	0·20(2)	0·15(3)
TiO_2	0·18(3)	0·17(4)	0·17(4)	0·20(11)	0·25(5)	0·48(7)	0·48(1)	0·50(2)	0·27(5)
Al_2O_3	0·04(1)	0·04(1)	0·03(2)	0·07(2)	0·06(2)	0·12(6)	0·11(4)	0·12(2)	0·06(2)
FeO	0·30(2)	0·21(7)	0·18(8)	0·45(6)	0·30(4)	0·63(7)	0·59(7)	0·66(6)	0·36(4)
MgO	0·50(3)	0·72(9)	0·58(3)	0·76(15)	0·74(5)	0·97(4)	1·09(16)	1·45(6)	0·63(3)
CaO	1·31(8)	1·44(10)	1·30(16)	1·44(11)	1·47(14)	1·85(23)	1·9(4)	2·41(29)	1·17(15)
Na_2O	1·63(22)	1·8(4)	1·6(4)	1·6(4)	1·68(4)	1·33(24)	1·3(4)	1·3(4)	1·54(30)
K_2O	1·98(21)	2·06(21)	1·9(3)	1·70(18)	1·88(4)	1·11(16)	1·09(30)	0·99(20)	1·83(21)
P_2O_5	1·54(6)	1·90(9)	1·77(8)	1·63(17)	3·32(19)	2·62(18)	3·53(24)	3·26(21)	3·14(20)
Trace elements									
Cs	2·26(11)	2·96(15)	2·26(9)	2·36(20)	2·47(12)	1·02(6)	1·19(5)	0·94(5)	3·05(12)
Rb	1·76(5)	2·35(6)	1·77(6)	1·63(14)	2·01(6)	0·98(4)	1·11(5)	0·93(5)	2·23(7)
Li	1·19(6)	1·57(6)	1·35(10)	1·34(13)	1·49(9)	1·21(8)	1·45(8)	1·66(10)	1·42(5)
Ba	1·43(6)	1·88(6)	1·62(9)	2·01(16)	1·77(7)	1·55(8)	1·75(6)	2·32(15)	1·56(6)
Sr	1·38(3)	1·84(3)	1·61(4)	1·61(13)	1·81(3)	1·71(4)	1·96(4)	2·69(14)	1·52(5)
Be	0·13(4)	0·12(4)	0·11(3)	0·18(5)	0·18(5)	0·35(2)	0·36(2)	0·42(3)	0·18(4)
Pb	0·46(25)	0·33(13)	0·44(4)	0·28(14)	0·52(5)	0·69(4)	0·81(5)	0·97(12)	0·47(17)
Th	0·09(2)	0·09(4)	0·09(3)	0·22(4)	0·15(4)	0·42(1)	0·47(1)	0·59(3)	0·14(4)
U	0·21(3)	0·37(5)	0·31(4)	0·38(6)	0·43(5)	0·62(3)	0·76(2)	0·82(4)	0·31(5)
Hf	0·05(1)	0·04(2)	0·04(2)	0·10(3)	0·07(3)	0·20(1)	0·22(1)	0·20(1)	0·08(3)
Zr	0·07(2)	0·06(3)	0·06(3)	0·12(3)	0·09(3)	0·26(1)	0·28(1)	0·26(1)	0·11(4)
Nb	0·39(4)	0·44(6)	0·37(5)	0·50(6)	0·52(6)	0·63(2)	0·73(2)	0·67(4)	0·62(7)
Ta	0·18(8)	0·18(7)	0·18(4)	0·31(10)	0·26(7)	0·41(3)	0·45(3)	0·34(13)	0·33(9)
Mo	5·8(5)	8·46(9)	6·8(4)	5·1(4)	5·9(6)	3·73(28)	4·70(27)	4·8(4)	8·7(5)
La	0·47(3)	0·62(5)	0·58(3)	0·90(7)	0·73(5)	1·20(3)	1·38(3)	2·15(18)	0·56(4)
Ce	0·4(3)	0·51(4)	0·48(3)	0·79(8)	0·63(5)	1·08(3)	1·24(2)	1·86(12)	0·49(5)
Pr	0·39(3)	0·50(4)	0·47(3)	0·76(7)	0·61(5)	1·06(2)	1·23(3)	1·85(13)	0·48(5)
Nd	0·39(3)	0·49(5)	0·46(3)	0·75(7)	0·61(4)	1·06(3)	1·19(3)	1·77(12)	0·48(4)
Sm	0·35(3)	0·44(4)	0·42(3)	0·69(7)	0·56(5)	0·98(3)	1·12(4)	1·66(10)	0·44(5)
Eu	0·44(3)	0·42(5)	0·41(3)	0·82(7)	0·55(5)	0·97(2)	1·09(2)	1·61(9)	0·58(4)
Gd	0·35(4)	0·43(5)	0·42(4)	0·67(7)	0·54(5)	0·97(4)	1·13(3)	1·59(9)	0·43(5)
Tb	0·32(3)	0·38(5)	0·37(3)	0·61(6)	0·50(5)	0·91(2)	1·05(2)	1·55(11)	0·40(5)
Dy	0·30(3)	0·36(5)	0·35(3)	0·59(7)	0·47(5)	0·88(3)	1·00(3)	1·45(10)	0·38(5)
Er	0·28(3)	0·32(5)	0·32(4)	0·54(6)	0·43(5)	0·83(3)	0·94(2)	1·33(8)	0·35(5)
Yb	0·23(3)	0·27(5)	0·27(4)	0·47(6)	0·36(5)	0·75(2)	0·84(2)	1·17(8)	0·31(5)
Lu	0·23(3)	0·26(5)	0·26(4)	0·45(6)	0·36(5)	0·73(2)	0·84(2)	1·18(7)	0·30(5)
Y	0·32(3)	0·37(5)	0·37(4)	0·50(5)	0·49(5)	0·92(3)	1·03(2)	1·50(10)	0·39(5)
Sc	0·14(3)	0·14(4)	0·13(4)	0·24(5)	0·21(5)	0·49(1)	0·53(1)	0·66(4)	0·20(5)
V	1·13(6)	2·04(17)	1·63(10)	0·96(9)	1·74(12)	1·24(7)	1·49(6)	1·49(8)	1·47(5)
Cr	0·29(5)	0·22(10)	0·12(4)	0·31(6)	0·21(5)	0·47(1)	0·51(2)	0·69(15)	0·30(7)
Mn	0·37(2)	0·44(4)	0·41(3)	0·56(5)	0·54(5)	0·81(3)	0·92(3)	1·13(5)	0·46(4)
Co	0·30(6)	0·31(4)	0·30(3)	0·46(6)	0·40(4)	0·65(3)	0·74(2)	0·87(5)	0·34(6)
Cu	n.a.	1·55(11)	1·20(9)	1·41(15)	1·53(12)	n.a.	0·79(15)	0·71(24)	1·51(12)
Zn	0·20(6)	0·17(3)	0·15(5)	0·28(12)	0·20(3)	0·44(3)	0·52(4)	0·60(3)	0·28(7)
Ga	0·38(2)	0·06(2)	0·05(2)	0·48(5)	0·08(3)	0·19(1)	0·20(1)	0·18(1)	0·38(6)
Ge	0·37(8)	0·17(3)	0·13(3)	0·65(9)	0·22(4)	0·36(2)	0·35(2)	0·37(3)	0·48(5)
Partition coefficient ratios									
D (Zr/Hf)	1·35(4)	1·48(33)	1·37(6)	1·36(5)	1·34(6)	1·27(4)	1·28(4)	1·31(3)	1·34(5)
D (Nb/Ta)	2·4(10)	2·76(143)	2·2(4)	2·00(5)	2·0(3)	1·55(13)	1·61(11)	2·0(8)	2·0(5)
D (La/Lu)	2·03(23)	2·48(38)	2·3(3)	1·99(13)	2·06(15)	1·64(3)	1·65(2)	1·82(5)	2·00(30)

D values of major element except for P_2O_5 and TiO_2 are calculated from EPMA. n.a., not analysed.

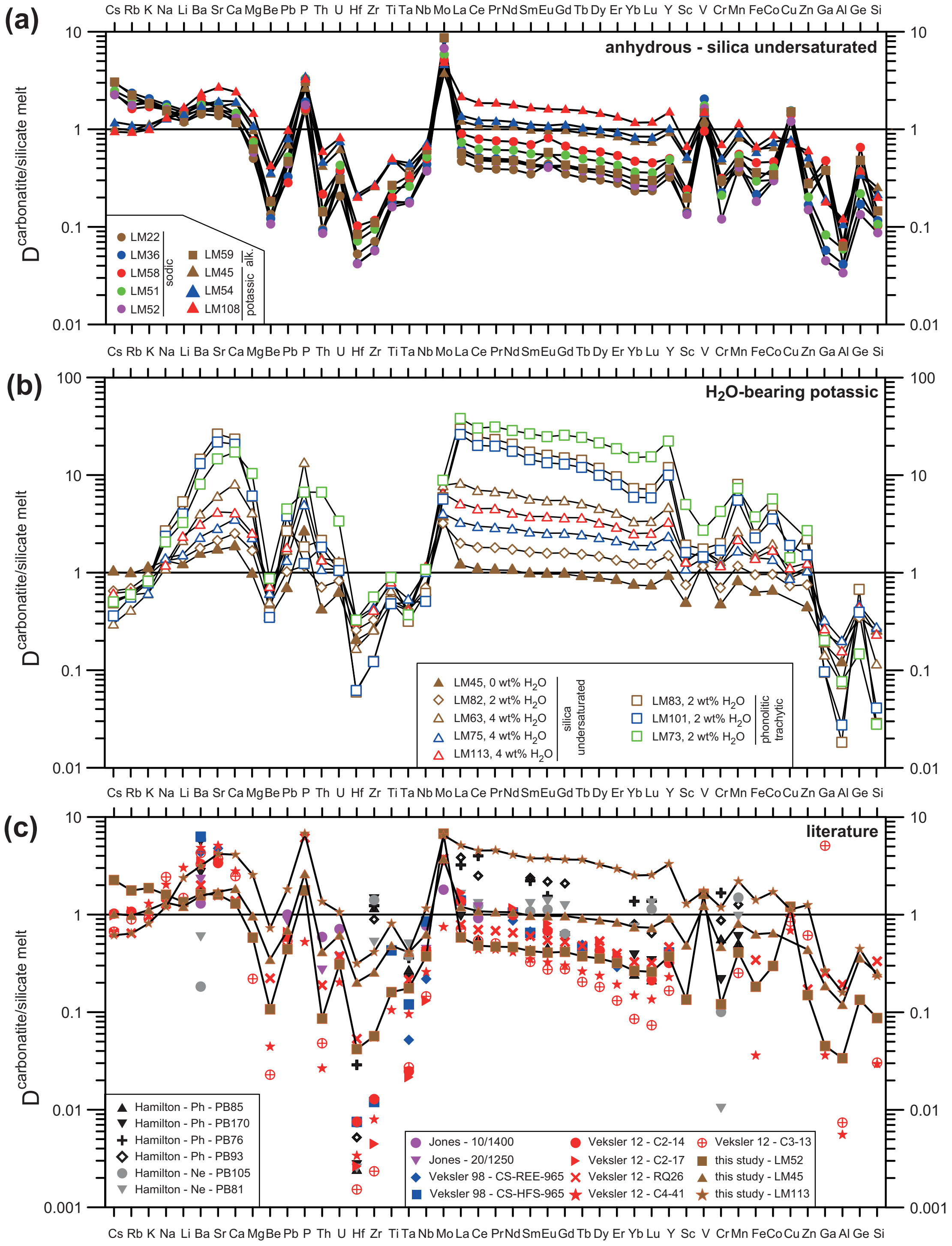

Fig. 6. Partition coefficients $D^{\text{carbonatite/silicate melt}}$ grouped into alkali, alkaline earth, high field strength elements (HFSE), rare earth elements (REE), third row transition metals (TM) and common network formers (Al, Ga, Si, Ge). (a) Partition coefficients for the anhydrous systems. The D^{REE} form a linear trend; D^{Eu} deviates from this linear trend only for the reducing experiments with graphite (LM22, LM58, LM59; $f_{O_2} = \text{IW} \pm 0{\cdot}5$). (b) Partition coefficients for the H_2O-bearing systems show the same patterns as the anhydrous ones (except for the alkalis and alkaline earths) but shifted towards the carbonatite melt. For the highly polymerized Si-rich melts, which result in the widest miscibility gap, the partitioning becomes stronger. (c) Partition coefficients from Hamilton *et al.* (1989), Jones *et al.* (1995), and Veksler *et al.* (1998, 2012) compared with three experiments from this study. Patterns compare well with those from our anhydrous systems. Partition coefficients for Zr, Hf (and other HFSE) overlap, but those of Veksler *et al.* (1998, 2012) are up to one order of magnitude lower than ours. The high partition coefficients determined by Hamilton *et al.* (1989) for H_2O-bearing systems are within the range of our H_2O-bearing systems.

The silica-undersaturated potassic systems reveal the following changes in partitioning behaviour with H_2O content increasing from 0 to 4 wt %: most *D* values increase by a factor of ~2 with addition of 2 wt % H_2O (LM82) and by a factor of 3–7 with addition of 4 wt % H_2O (LM75, LM113, LM63). Moreover, an increase in silicate melt polymerization from an NBO/T of 1–1·5 to 0·25–0·12 correlates well with an increase of D^{REE} and more generally of most partition coefficients at both 2 and 4 wt % H_2O. In other words, the less bridging oxygen is present in the silicate melt, the stronger most trace elements partition into the carbonatite melt. This is best illustrated with the D^{REE} and $D^{alkaline\ earth\ elements}$ vs NBO/T (Fig. 9). The *D* values of the alkali elements Cs–Na show an opposite behaviour (Fig. 7d) and slightly decrease with increasing polymerization ($D^{Cs} = 0{\cdot}3$–$0{\cdot}65$).

The partition coefficients for the REE show the largest difference in comparison with the anhydrous systems: the dry systems have a narrow range in partition coefficients ($D^{La} = 0{\cdot}47$–$2{\cdot}2$) whereas the H_2O-bearing ones have the REE strongly partitioning into the carbonatite melt with $D^{La} = 2{\cdot}0$–38. Concomitantly, $D^{La/Lu}$ increases from 1·3 to 4·5, yielding a steeper negative slope of the D^{REE} patterns with increasing H_2O content and silicate melt polymerization (Figs 6b and 7c, d). With respect to the anhydrous system, P and Mo (Fig. 8d) have similar ranges of partition coefficients in the H_2O-bearing systems ($D^P = 1{\cdot}1$–$13{\cdot}5$, $D^{Mo} = 3{\cdot}2$–$8{\cdot}9$), leading to higher REE and in part Ba to Ca partition coefficients than those of Mo (Fig. 6b). As in the dry systems, the other high field strength elements Hf, Zr, Ti, Nb, Ta (Fig. 8c) and Sc preferentially partition into the silicate melt, with Zr and Hf, having the lowest *D*

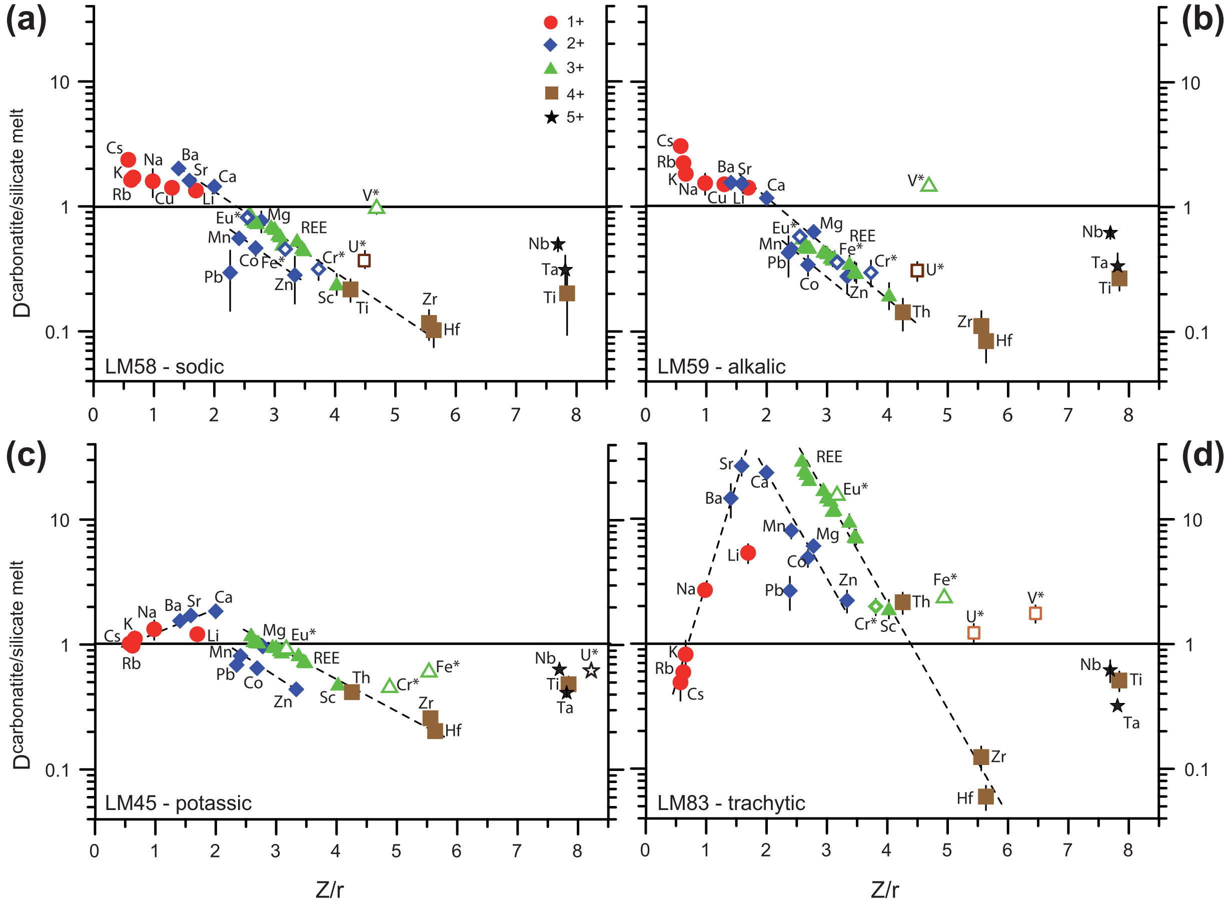

Fig. 7. Partition coefficients vs ionic potential (charge/ionic radius; radii from Shannon, 1976) as a proxy for the bond strength of network-modifier cations (Hudon & Baker, 2002). For the multi-valent (open symbols) or variably coordinated cations, average ionic potentials are used (details are given in the Electronic Appendix). The dashed lines represent trend lines for given cation groups. (a) LM58 from the sodic dry system with graphite leading to an f_{O2} of IW ± 0·5; (b) LM59 from the alkalic dry system containing graphite, $f_{O2} \sim$ IW ± 0·5; (c) LM45 from the potassic dry system at an f_{O2} just below HM; (d) LM83 from the H_2O-bearing trachytic system at a f_{O2} near QFM. *D* values of alkali and alkaline earth elements Ba–Ca for the sodic and alkalic systems (a) and (b) decrease with increasing ionic potential in contrast to the potassic systems, where they increase with ionic potential. The partition coefficients of the REE form a linear trend that extends into the partition coefficients of the tetravalent HFSE Th, Zr, Hf, suggesting that their relative partitioning behaviour between the carbonatite and silicate melt is mainly governed by ionic potential. Similarly, the divalent third row transition metals and Pb form a parallel trend. Oxidized U does not fall on any trend but lies towards the Ti–Ta–Nb cluster.

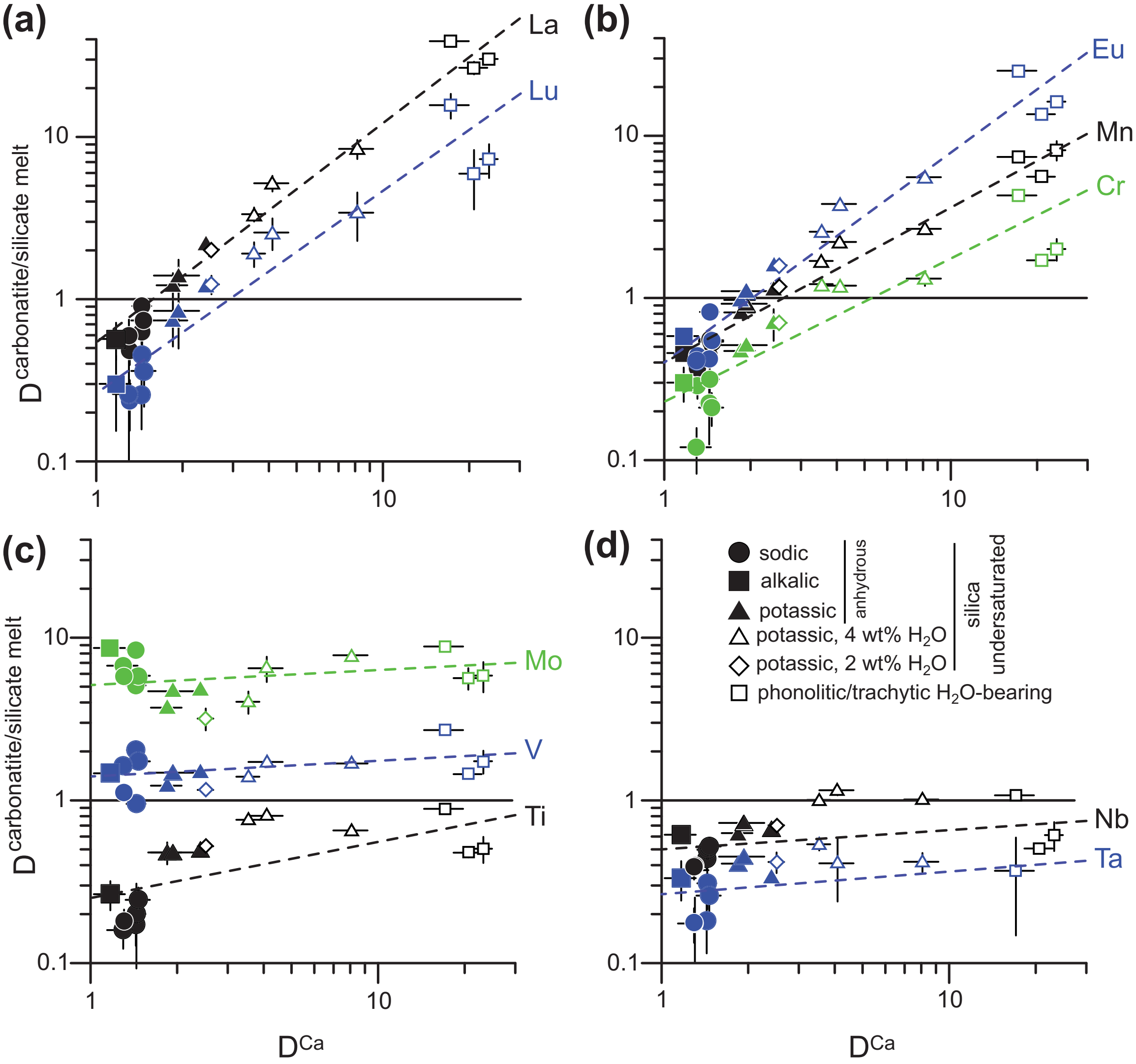

Fig. 8. (a) D^{Ca} vs D^{La} and D^{Lu} and (b) D^{Ca} vs D^{Eu}, D^{Mn} and D^{Cr}, all showing positive correlations indicating that Ca is a good proxy for the magnitude of partitioning for most network-modifier cations. (c) D^{Ca} vs D^{Mo}, D^{V} and D^{Ti} and (d) D^{Ca} vs D^{Nb} and D^{Ta} show much less variation, possibly indicating a structural environment that is significantly different (as known for Mo; see text). The chemical system is coded by symbol shape as indicated in the legend; colors refer to different elements.

values ($D^{Zr}=0{\cdot}12$–$0{\cdot}56$, $D^{Hf}=0{\cdot}06$–$0{\cdot}34$). In contrast to the anhydrous systems, Th and U become mostly moderately compatible in the carbonatite melt ($D^{Th}=0{\cdot}7$–$2{\cdot}1$ and $D^{U}=0{\cdot}8$–$1{\cdot}3$) with increasing H_2O and SiO_2 contents of the silicate melt.The highest partition coefficients of U and Th are determined for the most polymerized silicate melt (LM73, $D^{Th}=6{\cdot}7$; $D^{U}=3{\cdot}4$; Fig. 6b). The fractionation of the geochemical pairs Zr/Hf and Nb/Ta varies in the range $D^{Zr/Hf}=1{\cdot}3$–$2{\cdot}1$ and $D^{Nb/Ta}=1{\cdot}7$–$3{\cdot}0$, which is slightly higher than for the anhydrous systems (Tables 8 and 9; Fig. 10c and d). Moreover, with an increasing width of the miscibility gap or molar ratio of $(Si+Ti+Al)/(Si+Ti+Al+Fe+Mg+Ca+Na+K)$ in the silicate melt, the Zr/Hf ratio also increases (Fig. 10a and b), indicating that inter-element fractionation also increases with the width of the miscibility gap. Positive correlations also exist between $D^{La/Lu}$ and $D^{Zr/Hf}$ as well as $D^{Nb/Ta}$ (Fig. 10c and d).

In contrast to the anhydrous systems, the third row transition metals Cr, Mn, Fe, Co, Cu and Zn generally partition into the H_2O-bearing carbonatite melts, with D values ranging from 1·4 to 8 (Fig. 8b). Only in experiment LM82, which has the lower bulk H_2O content and the lowest silicate melt polymerization of this series, do these transition metals show, in part, an affinity for the silicate melt ($D=0{\cdot}7$–$1{\cdot}2$). Of the third row transition metals, only V always partitions into the carbonatite melt, with $D^{V}=1{\cdot}0$–$2{\cdot}0$ for the dry and 1·2–2·7 for the H_2O-bearing systems (Fig. 8d).

Table 9: Partition coefficients for the H_2O-bearing systems

Experiment:	LM82	LM75	LM113	LM63	LM73	LM83	LM101
Starting material:	KF6	KF5	KF8	KF5	ThS3B	ThS4	ThS4
P (GPa)/*T* (°C):	1·7/1200	1·7/1150	1·7/1150	1·7/1150	3/1160	3/1160	3/1160
Major elements							
SiO_2	0·26(2)	0·28(4)	0·24(5)	0·12(2)	0·03(2)	0·03(1)	0·04(2)
TiO_2	0·53(1)	0·76(4)	0·81(3)	0·66(1)	0·89(4)	0·51(9)	0·48(3)
Al_2O_3	0·18(2)	0·20(3)	0·16(4)	0·07(2)	0·08(2)	0·02(1)	0·03(1)
FeO	0·95(10)	1·41(12)	1·41(24)	1·5(6)	3·7(3)	2·45(21)	2·3(3)
MgO	1·68(8)	2·29(15)	2·55(26)	4·1(12)	10·4(19)	6·1(5)	6·1(8)
CaO	2·52(16)	3·6(3)	4·1(6)	8·1(11)	17·0(27)	23·4(17)	20·7(23)
Na_2O	1·32(16)	1·41(25)	1·2(4)	1·1(3)	2·1(4)	2·68(25)	2·4(4)
K_2O	0·93(8)	0·62(8)	0·81(10)	0·61(8)	0·82(49)	0·82(24)	0·78(31)
P_2O_5	1·17(9)	5·0(4)	6·8(3)	13·5(8)	5·56(17)	1·29(18)	1·05(9)
Trace elements							
Cs	0·65(6)	0·52(4)	0·61(5)	0·30(2)	0·50(3)	0·49(14)	0·36(3)
Rb	0·69(5)	0·59(2)	0·64(4)	0·41(2)	0·60(3)	0·59(5)	0·56(5)
Li	1·42(16)	1·53(10)	2·4(4)	2·14(25)	3·26(27)	5·3(9)	4·0(3)
Ba	1·78(12)	2·31(13)	3·15(8)	4·01(14)	8·07(25)	15(4)	13·1(3)
Sr	2·14(4)	2·85(5)	4·19(8)	6·09(11)	14·65(25)	26·0(4)	21·8(6)
Be	0·46(5)	0·62(4)	0·73(7)	0·50(4)	0·87(6)	0·39(7)	0·35(3)
Pb	1·02(11)	1·34(13)	1·81(5)	1·70(29)	4·5(4)	2·7(8)	3·8(4)
Th	0·71(7)	1·08(14)	1·4(3)	1·40(5)	6·67(24)	2·1(4)	1·83(18)
U	0·83(7)	1·09(26)	1·1(4)	1·31(7)	3·38(15)	1·24(21)	1·05(9)
Hf	0·26(1)	0·34(1)	0·31(2)	0·17(1)	0·33(1)	0·06(1)	0·06(1)
Zr	0·33(2)	0·44(2)	0·41(3)	0·26(1)	0·56(2)	0·12(3)	0·12(1)
Nb	0·70(1)	1·01(6)	1·16(8)	1·01(4)	1·08(5)	0·61(12)	0·51(2)
Ta	0·42(6)	0·54(5)	0·41(17)	0·42(6)	0·37(22)	0·32(9)	b.d.
Mo	3·2(5)	4·1(6)	6·5(12)	7·8(6)	8·9(5)	5·9(12)	5·7(9)
La	2·00(6)	3·30(10)	5·10(14)	8·30(12)	38·0(13)	29·6(25)	26·1(5)
Ce	1·81(5)	2·99(11)	4·53(10)	6·98(15)	33(9)	24·6(14)	20·1(4)
Pr	1·80(4)	2·91(8)	4·55(10)	6·79(11)	31·2(10)	23·2(13)	19·8(4)
Nd	1·73(4)	2·83(7)	4·10(9)	6·46(19)	28·6(15)	20·7(10)	17·5(5)
Sm	1·63(4)	2·62(6)	3·77(7)	5·70(6)	26·5(10)	17·2(13)	14·4(5)
Eu	1·58(5)	2·54(5)	3·76(11)	5·48(11)	24·7(6)	16·0(10)	13·4(4)
Gd	1·59(6)	2·54(5)	3·66(11)	5·49(13)	25·6(8)	15·0(13)	12·92(28)
Tb	1·54(4)	2·46(5)	3·65(12)	5·11(8)	24·3(4)	14·2(13)	11·99(26)
Dy	1·47(6)	2·30(5)	3·25(9)	4·57(9)	21·4(8)	11·7(12)	9·9(3)
Er	1·34(5)	2·13(5)	2·94(12)	4·08(9)	18·6(5)	9·6(12)	7·97(22)
Yb	1·23(5)	1·90(6)	2·51(12)	3·34(11)	15·13(27)	7·3(9)	5·93(17)
Lu	1·22(5)	1·89(6)	2·54(14)	3·37(5)	15·4(3)	7·2(10)	5·84(17)
Y	1·50(5)	2·36(5)	3·0(10)	4·67(6)	22·3(5)	11·9(14)	9·98(26)
Sc	0·75(2)	1·10(4)	1·29(7)	1·33(4)	4·99(6)	1·9(3)	1·61(4)
V	1·17(4)	1·40(7)	1·73(11)	1·69(7)	2·71(10)	1·75(28)	1·46(8)
Cr	0·70(4)	1·21(8)	1·18(7)	1·31(13)	4·24(10)	1·99(30)	1·69(7)
Mn	1·17(5)	1·68(6)	2·19(6)	2·64(8)	7·30(19)	8·0(11)	5·52(12)
Co	0·96(3)	1·37(5)	1·71(3)	1·97(9)	5·69(21)	4·9(8)	3·55(15)
Cu	0·73(15)	0·88(27)	1·13(27)	0·94(30)	1·4(4)	b.d.	1·91(51)
Zn	0·75(7)	1·05(6)	1·25(6)	1·13(6)	2·7(4)	2·2(5)	1·52(15)
Ga	0·24(1)	0·33(9)	0·27(1)	0·14(1)	0·20(1)	0·10(1)	0·10(1)
Ge	0·35(2)	0·47(4)	0·45(1)	0·45(3)	0·15(1)	0·7(2)	0·39(3)
Partition coefficient ratios							
D (Zr/Hf)	1·27(3)	1·30(2)	1·31(2)	1·54(2)	1·72(5)	2·07(7)	1·98(4)
D (Nb/Ta)	1·69(24)	1·87(20)	2·7(11)	2·40(31)	3·0(15)	1·9(7)	–
D (La/Lu)	1·64(5)	1·75(7)	2·01(9)	2·47(4)	2·47(7)	4·0(8)	4·47(9)

D values of major element except for P_2O_5 and TiO_2 are calculated from EPMA. b.d., below detection limit.

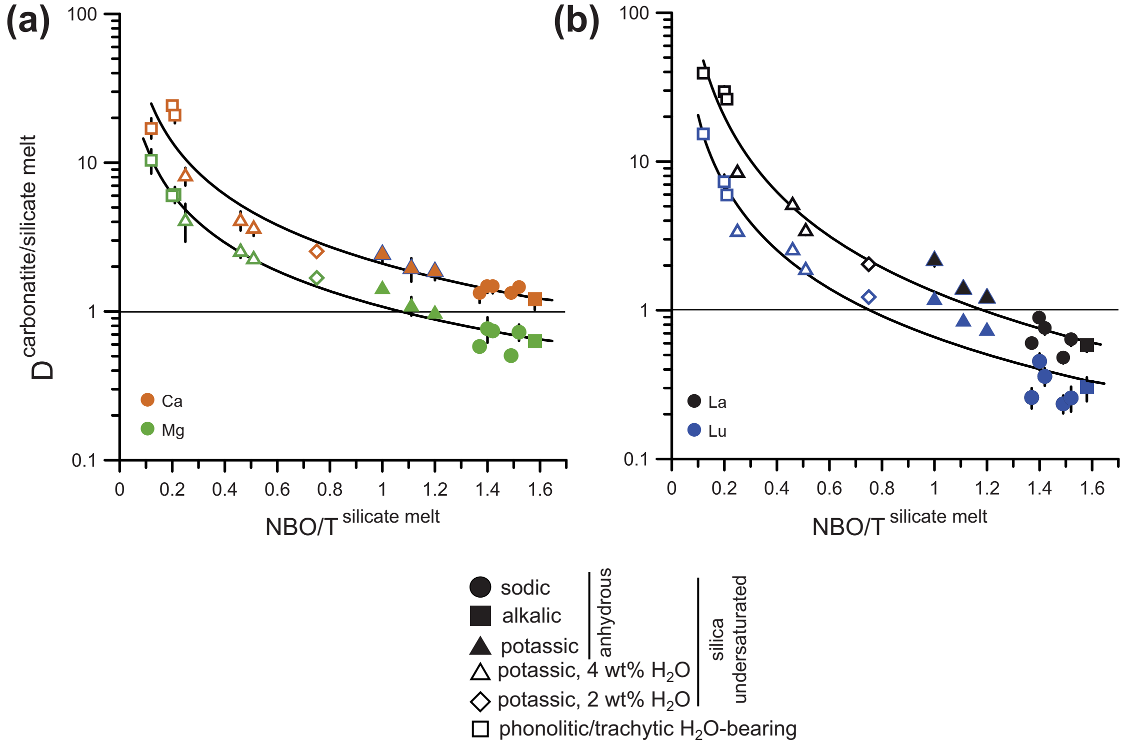

Fig. 9. Effect of melt polymerization on partition coefficients, illustrated by (a) NBO/T vs D^{Ca} and D^{Mg}, and (b) NBO/T vs D^{La} and D^{Lu}. Increasing polymerization renders most network-modifier cations increasingly incompatible with the silicate melt.

Finally, the amphoteric elements Be, Al, Ga, Si and Ge always partition into the silicate melt. The major element Al has the lowest distribution coefficient of all measured elements ($D^{Al} = 0{\cdot}02$–$0{\cdot}20$), followed by Si ($D^{Si} = 0{\cdot}03$–$0{\cdot}28$).

DISCUSSION

Major element distribution in the conjugate liquids

Distribution coefficients for the major elements as a function of miscibility gap width (expressed by D^{Ca}) are given in Fig. 11. The smooth trends of these distribution coefficients with the width of the miscibility gap probably reflect the limited range of temperature and pressure investigated in this study. Nevertheless, two types of behaviour are evident. D^{Mg} (in fact all alkaline earth, also D^{Sr} and D^{Ba}) and D^{Fe} correlate well with D^{Ca}, underlining the similar structural role of these elements in each melt type. In contrast, D^{Al} and D^{Si} and also D^{Na} and D^{K} deviate less from unity with increasing D^{Ca} or width of the miscibility gap in the anhydrous systems, whereas they increase in magnitude with increasing width of the miscibility gap in the H_2O-bearing experiments (except D^{K}, which is near unity). Hence, the hydrous systems behave as expected, but the behaviour of, in particular, Al and Si in the anhydrous systems leads to a peculiar minimum difference in Al, Si and Na concentrations between the conjugate silicate and carbonatite melts at a D^{Ca} of ~3. The reason for this behaviour, and also whether this minimum is simply due to the fact that at higher D^{Ca} all experiments had 2–4 wt % H_2O present, remains unclear. To further understand this topic, the structural role of alkalis and silicate melt network formers in complex carbonatite melts would need to be understood.

The absence of immiscibility in alkali-poor systems

In this study we have attempted to reproduce the liquid immiscibility reported by Novella & Keshav (2010) in an alkali-free CaO–MgO–Al_2O_3–SiO_2–CO_2 system, and that reported by Dasgupta *et al.* (2006) in an alkali-poor basaltic bulk composition. The aim was to understand the variation of partition coefficients as a function of alkali content. Nevertheless, at the reported run conditions, liquid immiscibility was not reproduced for the CaO–MgO–Al_2O_3–SiO_2–CO_2 system but a homogeneous liquid resulted. For the basaltic system, alkali contents were also increased but the result remained a single silicate liquid mostly coexisting with merwinite, monticellite or carbonates.

In fact, neither Novella & Keshav (2010) nor Dasgupta *et al.* (2006) observed two coexisting melts in direct contact. The evidence for liquid immiscibility remains

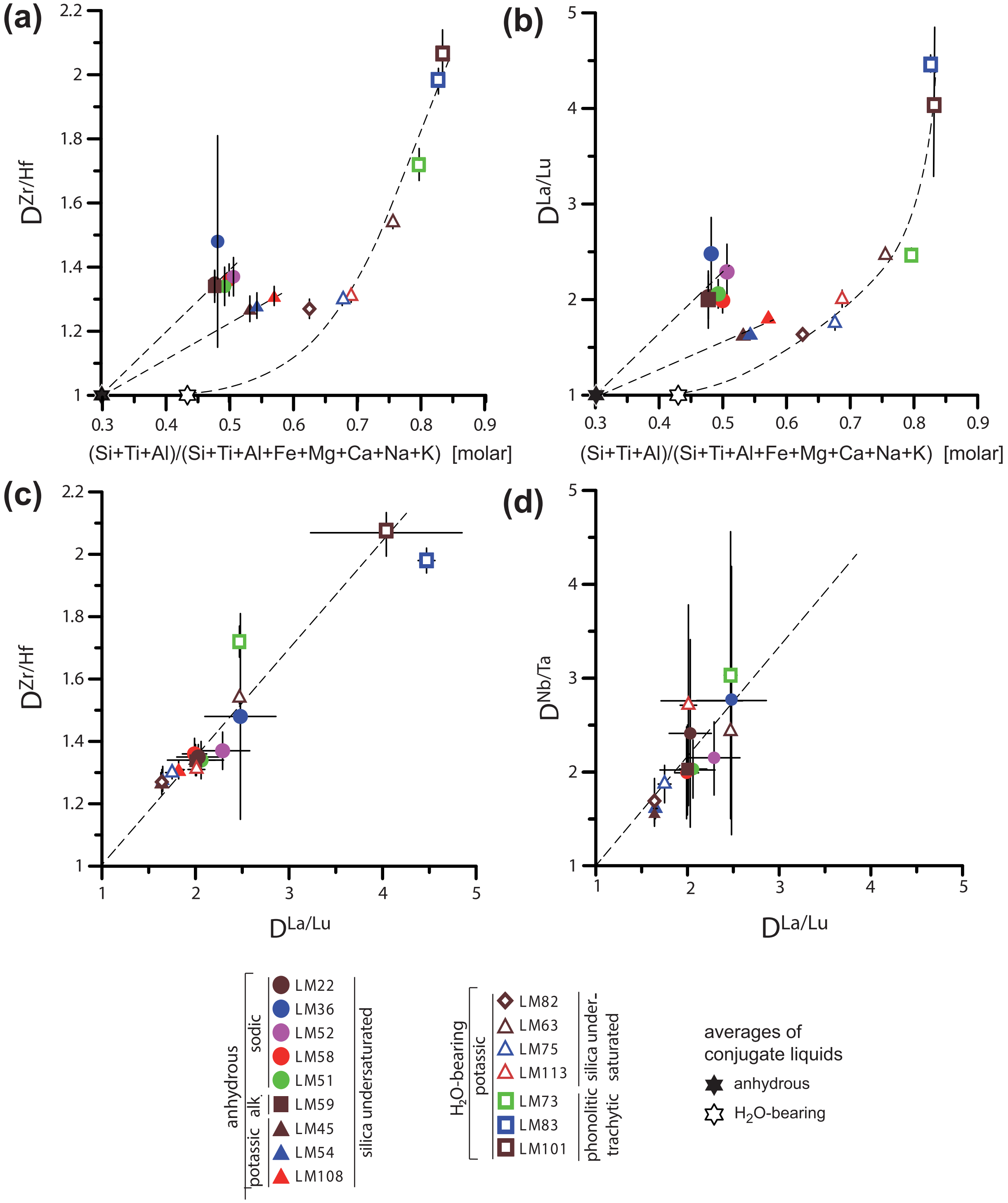

Fig. 10. Inter-element fractionation of HFSE and REE. (a, b) The fractionation of the geochemical pairs Zr and Hf and of the REE follows different trends in the different systems as a function of the width of the miscibility gap [expressed by the molar fraction of network forming cations (Si + Ti + Al)/(Si + Ti + Al + Fe + Mg + Ca + Na + K)]. $D^{La/Lu}$ and $D^{Zr/Hf}$ need to become unity at the consulate or critical point of the miscibility gap, which is approximated by the geometric middle of the gaps (as indicated in Fig. 4a and b). (c, d) Fractionation of Zr/Hf and Nb/Ta correlates with the fractionation of the REE; that is, $D^{La/Lu}$, $D^{Zr/Hf}$ and $D^{Nb/Ta}$ correlate positively among each other. For anhydrous compositions Zr/Hf fractionation is limited, whereas for H_2O-bearing systems, fractionation rises strongly with increasing width of the miscibility gap.

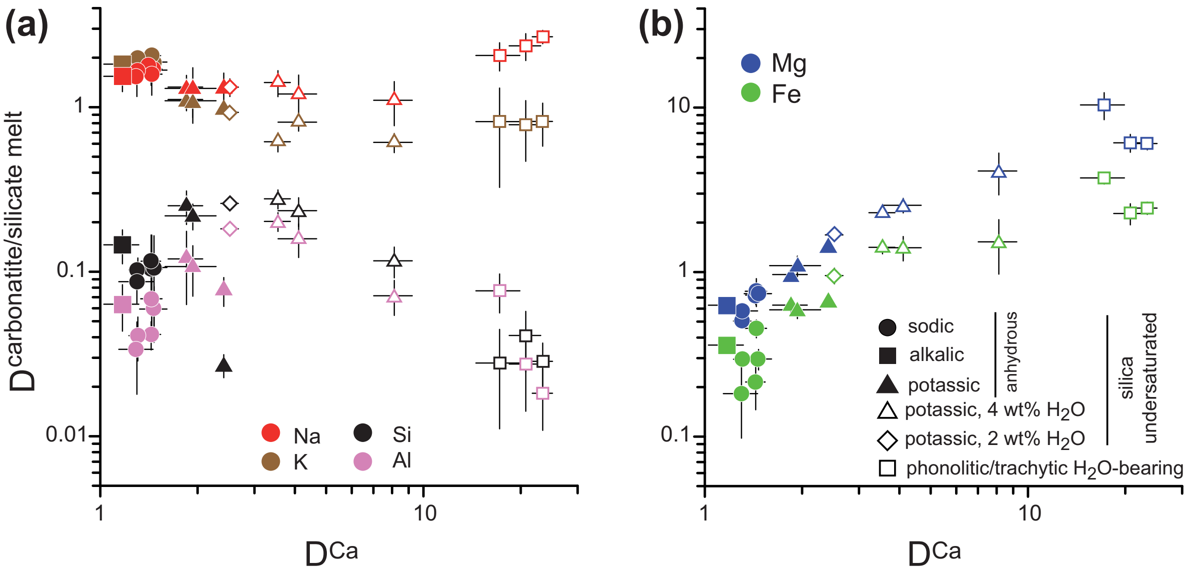

Fig. 11. Major element distribution coefficients as a function of D^{Ca}, which approximates the width of the miscibility gap. (a) Si, Al, K and Na. It should be noted that the minimal difference between the conjugate melts occurs at an intermediate D^{Ca} of ~3, but that the two limbs are composed of anhydrous and H_2O-bearing experiments respectively. (For discussion see text.) (b) Mg and Fe. The good correlations between D^{Ca}, D^{Mg} and D^{Fe} underline the similar structural roles of these elements in the melts of this study.

circumstantial; that is, a carbonate-rich quench between crystals in the crystal-rich portion of the capsule is interpreted as carbonatite melt, whereas the silicate melt is mostly identified in melt pools or is well separated into a crystal-free area of the capsule. As the reported melt compositions at the given experimental conditions do not yield liquid immiscibility, we conclude that the interstitial quench material does not represent a carbonatite melt. Most probably, quenching a CO_2-rich silicate melt within a silicate crystal aggregate yields quench growth rims on the silicates and a more sparitic interstitial quench mostly composed of carbonates. Reintegrating only the latter quench material does not lead to true melt compositions. Hence, we suggest abandoning reintegration of melt compositions from quench crystals that reach directly from one equilibrium crystal to the next. Instead, clear interfaces between the (quenched) liquids are necessary to demonstrate two-liquid immiscibility.

We also attempted to reproduce liquid immiscibility as reported by Thomsen & Schmidt (2008) during the melting of a carbonated quartz-saturated sediment to investigate the influence of silica saturation on partition coefficients. Texturally, the carbonate melt of Thomsen & Schmidt formed droplets in the silicate melt. Nevertheless, the reported carbonate melt compositions turned out to be alkali-deficient with respect to the true immiscible melts. In fact, the Thomsen & Schmidt (2008) carbonatite droplets were heavily wrinkled and ≤20 μm in size. Despite careful dry polishing and the use of defocused low-current beams during analysis, the reported K_2O concentrations amount to half of the true concentrations. We suggest that quenching of the H_2O-bearing carbonatites in the study of Thomsen & Schmidt (2008) led to either K_2O-rich H_2O-bearing fluids (explaining the voids in the wrinkles) or phases such as K(OH) that are unrecoverable upon polishing and result in significant alkali losses upon opening and preparation of the sample charges.

Comparison with previously determined carbonatite/silicate melt partition coefficients

Previous studies have determined partition coefficients for anhydrous or H_2O-poor systems for immiscible phonolite (or nephelinite) carbonatite liquids at 0·1–0·36 GPa (Hamilton *et al.*, 1989), for sodic systems at 0·7–2 GPa (Jones *et al.*, 1995), and for silica-undersaturated alkalic and haplogranitic systems at <0·1 GPa (Veksler *et al.*, 1998, 2012). Selected compositions are plotted in Fig. 6c. Most of these results compare well with our anhydrous systems. Nevertheless, partition coefficients for Lu ($D^{Lu} = 0·23$), Hf ($D^{Hf} = 0·003$) and some HFSE from Veksler *et al.* (2012) are up to one order of magnitude lower in comparison with our data.

The partition coefficients determined by Hamilton *et al.* (1989) at 0·08–0·6 GPa are in part higher than for other anhydrous systems as shown in Fig. 6c, but within the range of our H_2O-bearing systems. Hamilton *et al.* (1989) had 0·8–1·4 wt % H_2O present in their starting materials and obtained silicate melts with 34·3–52·5 wt % SiO_2 and 11·8–19·5 wt % Al_2O_3. Our results generally confirm the interpretation of Hamilton *et al.* (1989) that increased silicate melt polymerization yields higher *D* values. Nevertheless, the $D^{\mathrm{Zr/Hf}}$ of 42·8–668 resulting from a very low D^{Hf} of 0·00021–0·029 in the study by Hamilton *et al.* (1989) compares poorly with the $D^{\mathrm{Zr/Hf}} = 1{\cdot}1$–$2{\cdot}4$ of this study and that of Veksler *et al.* (2012). Such a strong fractionation of Zr/Hf seems unrealistic and is probably an analytical artefact resulting from the instrumental neutron activation analysis technique employed on melt separates by Hamilton *et al.* (1989) when LA-ICP-MS was not yet readily available. Some of the partition coefficients of Hamilton *et al.* for Cr also compare poorly with all other available studies.

Veksler *et al.* (2012) performed two experiments with 10·7 and 11·3 wt % H_2O for haplogranitic and Oldoinyo Lengai type compositions (RQ-21 and RQ26). The haplogranite in experiment RQ-21 has SiO_2 and Al_2O_3 contents comparable with those of the LM63 silicate melt, whereas RQ26 compares well with LM82. However, most partition coefficients from Veksler *et al.* (2012) are significantly lower than in our comparable experiments; for example, $D^{\mathrm{La}} = 1{\cdot}36$ and 8·3 for RQ-21 and LM63, respectively, and $D^{\mathrm{La}} = 0{\cdot}79$ and 2·0 for RQ26 and LM82, respectively.

Wendlandt & Harrison (1979) investigated the partitioning of Ce, Sm, and Tm in an albite–K_2CO_3 system at 0·5–2 GPa and concluded that LREE partition by a factor of 2–3 into the carbonatite melt and HREE by factors of 5–8. This finding is dissimilar to results from more complex systems where REE partition coefficients always decrease with increasing field strength or atomic number. At the time of their study, Wendlandt & Harrison had to determine trace element ratios by radiographic methods, which may have resulted in significant analytical artefacts.

Parameters controlling the partitioning of trace elements

The effects of miscibility gap width and of silicate melt polymerization

The relatively narrow range of partition coefficient patterns in the anhydrous systems can be explained by relatively similar widths of the carbonatite–silicate melt miscibility gap (Figs 2, 3a and 4a). In fact, our experiments indicate a flat-topped miscibility gap, the width of which does not strongly increase with temperature or varying bulk composition, but which suddenly opens within 20–30°C. Such a shape would be analogous to the two-silicate melt miscibility gap in the leucite–fayalite–quartz system (Roedder, 1978).

Partition coefficients should converge towards unity with decreasing width of the miscibility gap, and in fact experiment LM45, with partition coefficients closest to unity, has the narrowest miscibility gap. Partition coefficients for the alkalic system (LM59) and the sodic systems deviate more strongly from unity owing to wider miscibility gaps. This type of behavior is consistent with a miscibility gap width of the potassic experiments increasing from LM45 to LM54 to LM113 (Fig. 4a). The partitioning of the alkalis and alkaline earth elements is in fact dominated by the immiscibility gap width. The line connecting Cs–Rb–K–Na–Li–Ba–Sr increases in slope with increasing miscibility gap width, as best expressed by the variation of $D^{\mathrm{Rb/Sr}}$ or $D^{\mathrm{Cs/Sr}}$ (Fig. 12) with D^{Ca} and, in fact, rotates more or less around K (see also Fig. 6).

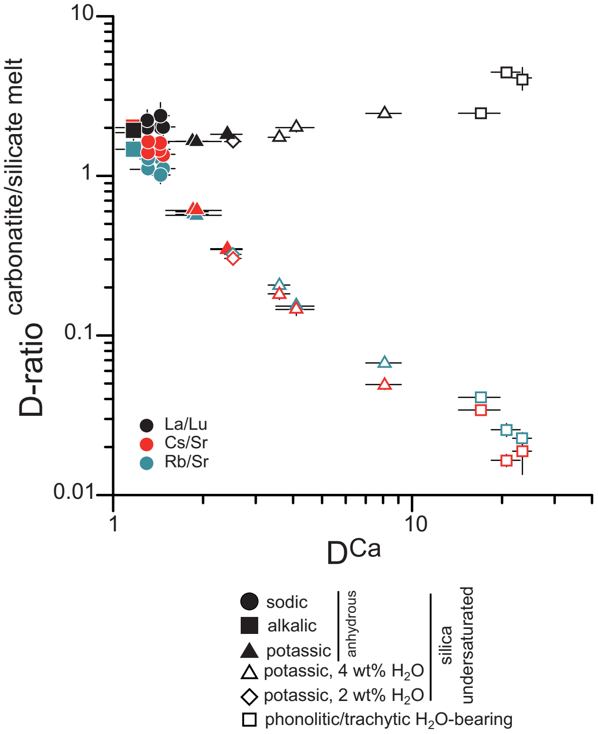

Fig. 12. D^{Ca} vs $D^{\mathrm{Cs/Sr}}$, $D^{\mathrm{Rb/Sr}}$ and $D^{\mathrm{La/Lu}}$. D^{Ca} approximates the miscibility gap width. $D^{\mathrm{Cs/Sr}}$ or $\mathrm{D}^{\mathrm{Rb/Sr}}$ yield the slope of the line D^{Cs}–D^{Rb}–D^{K}–D^{Na}–D^{Li}–D^{Ba}–D^{Sr}, which increases strongly with increasing miscibility gap width (see also Fig. 6a and b). In contrast, while D^{La} and D^{Lu} increase by two orders of magnitude (Fig. 8a), $D^{\mathrm{La/Lu}}$ varies little; the REE pattern simply shifts with miscibility gap width.

Nevertheless, a second type of behavior is observed and it is not only the miscibility gap width that governs the magnitude of trace element partitioning. Schmidt *et al.* (2006), for silicate–silicate melt immiscibility, indicated that the increasing polymerization of melts on the granitic limb of the two-silicate melt miscibility gap renders trace elements more incompatible with this melt and favours partitioning into the depolymerized conjugate gabbroic melt. The NBO/T values for the silicate melts of our study decrease from the sodic to the potassic anhydrous systems (from 1·6 to 1·1; Fig. 9) and further within the H_2O-bearing systems (from 0·75 to 0·12). For many trace elements, the general effect of decreasing NBO/T in the silicate melt (correlating well with D^{Ca} or the miscibility gap width) is not a general increase in the magnitude or spread of partitioning, but a shift of the partitioning patterns towards the carbonatite melt. In other words, with increasing silicate melt polymerization, trace elements should become increasingly incompatible with this melt. This is best illustrated by the increase of REE partition coefficients by almost two orders of magnitude with NBO/T, crossing the unity line (Fig. 9); that is, a behaviour that cannot be explained by a correlation with the miscibility gap width. At the same time $D^{La/Lu}$ increases by only a factor of three (Fig. 12); that is, the REE are simply shifted by two orders of magnitude with increasing polymerization in the silicate melt, from slightly compatible in the silicate melt to strongly partitioning into the carbonatite melt.

General features of the H_2O-bearing systems

As a first-order observation, addition of water increases the width of the miscibility gap (Figs 2 and 3b), and the silicate melt becomes richer in silica and alumina but poorer in calcium, magnesium and iron, leading to an increase in polymerization (Table 5; Fig. 9). Similar to partitioning between two silicate melts (Schmidt *et al.*, 2006), the increasingly polymerized silicate melts reject most trace elements in favor of the carbonatite melt, resulting in an increase of carbonatite/silicate melt partition coefficients. The highest partition coefficients are obtained for the silica and/or alumina-rich phonolitic and trachytic H_2O-bearing systems, with a D^{La} of 38 (Fig. 6b). The variations of SiO_2 and Al_2O_3 in our chemical systems lead to the lowest NBO/T and thus the highest polymerization in the phonolitic melt of LM73, which only has the third highest SiO_2 content (of 55·4 wt % compared with the trachytic melts with ~68 wt % in experiments LM83 and LM101). This experiment, in fact, has the highest trace element partition coefficients, demonstrating that melt polymerization and not SiO_2 content is the dominant chemical parameter.

It appears that the 2–4 wt % bulk H_2O contents in our experiments have a stronger effect on miscibility gap width and on partitioning than the 10·7–11·3 wt % H_2O in the experiments of Veksler *et al.* (2012; experiments RQ-21 and RQ26 at 0·1 GPa). The silicate melt of RQ-21 has SiO_2 and CaO contents comparable with our experiment LM63, but a higher NBO/T (LM63 = 0·25, RQ-21 = 0·9). RQ26 compares well in SiO_2, Al_2O_3 and CaO contents with our experiment LM82, although NBO/T differs (LM82 = 0·75, RQ26 = 1·0). Thus, the partition coefficients $D^{La} = 1{\cdot}36$ and 0·79 for RQ-21 and RQ-26 are much lower than for LM63 and LM82 which have $D^{La} = 8{\cdot}3$ and 2·0. Although Veksler *et al.* (2012) added 11 wt % H_2O, the confining pressure (0·1 GPa) was probably too low to dissolve large amounts of water in the silicate melt, thus resulting in only a small increase of partition coefficients. Nevertheless, Veksler *et al.* (2012) observed order of magnitude effects on Zr, Hf, Al and Si but not on the REE as in this study. Veksler *et al.* (2012) speculated that H_2O could lead to the formation of hydroxide species and increase the basicity of the H_2O-bearing carbonatite melts by hydrolysis reactions, which would increase the solubility of REE.

In summary, addition of H_2O increases the width of the miscibility gap as long as the melts do not saturate in volatiles. H_2O causes network formers such as SiO_2, TiO_2 and Al_2O_3 to partition more strongly into the silicate melt, whereas network modifiers such as Ca, Mg and Fe partition more into the carbonatite melt. This effect leads to a more polymerized silicate melt, which in turn leads to a large effect on element partitioning. With a wider miscibility gap, the fractionation of chemical pairs also increases.

The effect of bulk composition, volatile content, pressure, and oxygen fugacity

For anhydrous systems with depolymerized silicate melts, bulk composition has little influence on partition coefficients. Instead, the addition of H_2O results in a miscibility gap shape (in composition space) where bulk composition plays a more important role. The network-formers Si and Al are not well accommodated in the carbonatite melt; an increase in bulk SiO_2 leads mainly to a concentration of SiO_2 in the silicate melt. Figure 13 shows the variation of the width of the carbonatite–silicate melt miscibility gap in $(SiO_2 + TiO_2 + Al_2O_3)–(Ca,Mg,Fe)O–(Na,K)_2O$ space projected from CO_2 (+ H_2O) (after Hamilton *et al.*, 1979; Lee & Wyllie, 1997). The data from our study can be divided into to four groups (in bulk composition–pressure–temperature): dry sodic + alkali at 1240–1260°C, 1 GPa; dry potassic at 1220°C, 1·7 GPa; H_2O-bearing potassic with silica-undersaturated silicate melts at 1150°C, 1·7 GPa; H_2O-bearing potassic with silica-rich silicate melts at 1160°C, 3 GPa. Our melt compositions compare reasonably well with those of Brooker & Kjarsgaard (2011) for the $Na_2O–CaO–Al_2O_3–SiO_2–CO_2$ system and with compositions derived from natural bulk compositions. Nevertheless, there are large differences in the miscibility gaps drawn from the experiments in the complex system and those from the NCASC system as summarized by Brooker & Kjarsgard (2011). In general, K partitions less into the carbonatite than Na; consequently, two-melt tie-lines in K-rich systems have less steep slopes in $(SiO_2 + TiO_2 + Al_2O_3)–(Ca,Mg,Fe)O–(Na,K)_2O$ space (Fig. 13). This effect seems to be amplified by the addition of H_2O. Changing the bulk composition by addition of SiO_2 (and Al_2O_3) causes the silicate melt to polymerize and hence move away from the (Ca,Mg,Fe,Mn)O corner. The effects of bulk composition appear to be much stronger than the effects of pressure variation in this study (i.e. 1–3 GPa), and our data cannot be directly employed to constrain the evolution of the miscibility gap width with pressure.

Freestone & Hamilton (1980) and Hamilton *et al.* (1989) concluded that lower temperatures increase element partitioning and that an increase in pressure (within a crustal pressure range) has the same effect. They suggested that the miscibility gap width could principally be used to estimate the pressure and temperature conditions of

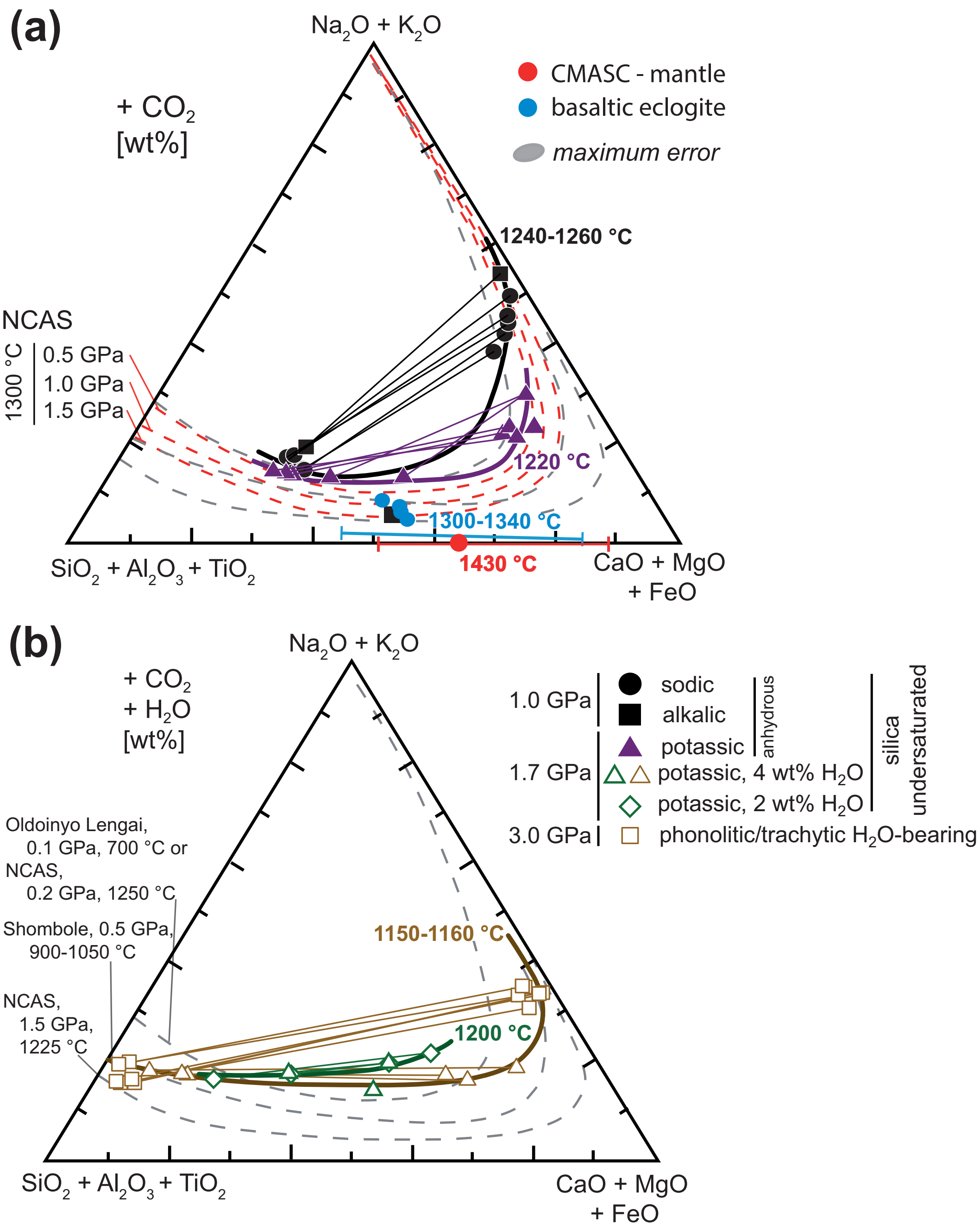

Fig. 13. Variations in the carbonatite–silicate melt miscibility gap in $(SiO_2 + Al_2O_3 + TiO_2)$–(Ca,Mg,Fe)O–$(Na,K)_2O$ space projected from CO_2 (+ H_2O) in wt % (after Hamilton *et al.*, 1979; Lee & Wyllie, 1997). The data from our study are derived from four types of bulk systems (in bulk composition–pressure–temperature): dry sodic or alkaline at 1240–1260°C, 1 GPa; dry potassic at 1220°C, 1·7 GPa; H_2O-bearing potassic silica-undersaturated at 1150–1200°C, 1·7 GPa; H_2O-bearing potassic and silica-saturated melts at 1160°C, 3 GPa. Our miscibility gaps are compared with those of Brooker & Kjarsgaard (2011) for the Na_2O–CaO–Al_2O_3–SiO_2–CO_2 system (red dashed lines) and with natural systems [grey dashed lines; Oldoinyo Lengai compositions from Kjaarsgard *et al.* (1995); Shombole compositions from Kjarsgaard & Peterson (1991)]. It should be noted that all miscibility gaps are only partly defined. Melt compositions of immiscible liquid pairs close to the critical point of the miscibility gap that were not sufficiently well separated for LA-ICP-MS analyses and single melt compositions are also plotted (these analyses are given in the Electronic Appendix). The blue and red lines show the postulated miscibility gaps of Dasgupta *et al.* (2006) and Novella & Keshav (2010) for a quartz-undersaturated basaltic eclogite and a CaO–MgO–Al_2O_3–SiO_2–CO_2 peridotite model system. Experiments with bulk compositions exactly in the middle of the proposed miscibility gaps yielded single liquids for the basaltic eclogite system coexisting with numerous silicate phases.

immiscibility. However, this method is of little use because H_2O, which is not conserved in natural carbonatites, also influences the width of the miscibility gap to a point where its width decreases with temperature; for example, experiment LM82, performed at 1200°C, has a narrower gap than LM63 at 1150°C (Fig. 4b). Furthermore, there is no direct experimental evidence for immiscibility at lower alkali contents, and in particular not for almost alkali-free, natural calcio- and dolomite–carbonatite compositons.

Similar to mineral–melt trace element partition coefficients, pressure itself has little direct effect on trace element melt/melt partitioning, as can be shown by comparing our partition coefficients for the anhydrous systems at 1–1·7 GPa with those of Veksler *et al.* (1998, 2012) at $\leq$0·1 GPa (Fig. 6). Nevertheless, pressure has an indirect effect, as the solubility of volatiles increases with pressure; thus, more volatiles are required to increase the miscibility gap width as indicated by Brooker (1998).

The effect of oxygen fugacity on element partitioning is relatively minor, as indicated by our results from experiments with varied Fe^{2+}/Fe^{3+} ratios. At reducing conditions Eu has higher partition coefficients compared with its neighboring elements Sm and Gd, whereas V, U and Mo do not show much change.

The partitioning behaviour of the different element groups

In this section we discuss the partitioning behaviour of single elements or element groups as presented in Figs 6 and 7. We follow previous studies that analysed the systematics of liquid immiscibility and consolute temperatures (Hudon & Baker, 2002) as well as of partition coefficients (e.g. Veksler, 2004; Veksler *et al.*, 2006, 2012; Schmidt *et al.*, 2006) in terms of ionic potential. This characterizes the quality of a bond; cations with high ionic potential generally form more covalent bonds than cations with low ionic potential, which form bonds of more ionic character (Huheey & Keiter 1993).

Ionic potential, being defined as cationic charge/ionic radius, obviously depends on oxidation state and coordination number. Under the oxygen fugacities of our experiments (~IW, ~QFM and just below HM), Cr, Eu, Fe, Mo, U and V may have multiple valence states and we have estimated their average oxidation states. Near IW, Cr has about 60% Cr^{2+} and 40% Cr^{3+} (Berry *et al.*, 2006), Eu has about 38% Eu^{2+} and 62% Eu^{3+} (Cicconi *et al.* 2012), Fe is almost completely divalent, Mo has 15% Mo^{4+} and 85% Mo^{6+} (O'Neill & Eggins, 2002), V is dominantly trivalent (Karner *et al.*, 2008), and U is U^{4+} (Schreiber, 1983). At oxygen fugacities around QFM, Cr is about half Cr^{2+} and half Cr^{3+} (Berry *et al.*, 2006), all Eu is trivalent (Cicconi *et al.*, 2012), Fe has about 60% Fe^{3+}, Mo is dominantly hexavalent, V has 20% V^{3+} and 80% V^{4+} (Karner *et al.*, 2008), and U has about 55% U^{4+} and 45% U^{5+} (Schreiber, 1983). For the oxidizing experiments with f_{O2} values close to HM, Cr is dominantly Cr^{3+} (Berry *et al.*, 2006), Eu is trivalent (Cicconi *et al.*, 2012), Fe has about 80% Fe^{3+}, Mo is dominantly hexavalent, V is dominantly V^{5+} (Karner *et al.*, 2008), and U has about 70% U^{5+} and 30% U^{6+} (Schreiber, 1983). From these valence states, their appropriate coordination numbers and ionic radii (Shannon, 1976) we calculate average ionic potentials. Similarly, for the REE and third row transition metals with multiple coordination numbers, we calculate average ionic potentials (details are given in the Electronic Appendix).

A general feature of the *D* vs ionic potential plots is an excellent overall correlation for (1) the alkali elements Cs–Na together with the alkaline earths Ba–Ca, (2) the divalent third row transition metals, and (3) the trivalent cations together with the tetravalent HFSE Th, Zr and Hf. Higher ionic potential cations do not follow particular trends: Ti, Nb and Ta have similar partition coefficients at similar ionic potentials; V and U^{5+} have generally higher partition coefficients than the trend defined by the REE and Th, Hf and Zr. On the other hand, Mo and P are not simply bound to non-bridging oxygens, and Be, Al, Si, Ga and Ge are network-formers that certainly have a very different structural role in silicate and carbonatite melts and are treated separately.

Last but not least, it should be emphasized that the coordination numbers above are based on the silicate glass literature and all arguments below can address only the silicate melt contribution. The structure of carbonatite melts is poorly constrained. Initially, carbonatite melts were considered as unpolymerized ionic liquids (Treiman, 1989) but infrared and Raman spectroscopy measurements have shown (Genge *et al.*, 1995; Williams & Knittle, 2003) that there are two different varieties of carbonate groups: an undisrupted symmetric carbonate group and highly asymmetric carbonate units with single C–O bonds forming bridges to metal cations.

Alkali and alkaline earth elements

The VIII- to VI-fold coordinated alkalis Cs, Rb, K and Na and alkaline earths Ba, Sr and Ca show a strong correlation in *D* vs Z/r space, which is negative in the sodic and alkaline systems (Fig. 7a and b) and positive in the potassic systems (Fig. 7c and d; *D* vs Z/r plots for all experiments are given in the Electronic Appendix). As already pointed out by Veksler *et al.* (2012), the IV-fold coordinated element Li and the dominantly V-fold coordinated Mg have amphoteric character. They fall below these trends.

The negative *D* vs Z/r trends for the (anhydrous) sodic and alkalic systems and the positive ones for the (anhydrous and H_2O-bearing) potassic systems (Fig. 7a–c) are perfectly reproducible in all six and 10 experiments, respectively. Similar to the potassic systems, the (anhydrous and H_2O-bearing) alkalic natrocarbonatite–nephelinite systems of Veksler *et al.* (2012) show coherently positive *D* vs Z/r correlations. Unfortunately, the reason for this behavior remains somewhat unclear. We note that the silicate melts of the sodic and alkaline systems of our study are the least polymerized (NBO/T = 1·37–1·58), whereas our potassic silicate melts and the alkaline melts of Veksler *et al.* (2012) are more polymerized (NBO/T = 0·12–1·20 and 0·55–1·0, respectively; see also Fig. 9). We further speculate that the different coordination numbers of K and Na in silicate melts (which may have some corresponding structural difference in the carbonatite melts) contribute to this behavior. The currently available information indicates that this behaviour depends on the K/Na ratio and H_2O content of the bulk system. Interestingly, the potassic granite–Fe-gabbro immiscibility experiments of Schmidt *et al.* (2006) also show a strong positive trend of D vs Z/r for the alkali and alkaline earth elements.

The alkaline earth Be is a special case: in silicate melts it is uniquely IV-fold coordinated (Sen *et al.*, 2008) and acts as a network-forming cation (Sen & Yu, 2005). Thus, Be cannot be included in a single group with the other network-modifying alkaline earths. Similar to Al, Si, Ga and Ge, Be partitions strongly into the silicate melt.

Rare earth elements

The LREE and Ca have similar partition coefficients in all experiments (Figs 6 and 7) and all D^{REE} and D^{Ca} correlate positively (Fig. 8a and b). The REE replace Ca in silicates and carbonates, and an analogous substitution is likely also in the melts. The REE (which by definition include Sc and Y) define a linear trend in D vs ionic potential space (Fig. 7), and the degree of fractionation (i.e. the slope of this trend) increases with the width of the miscibility gap (Fig. 4). Thus, both the addition of water and a higher degree of silicate melt polymerization result in increased partition coefficients for D^{La} up to 38 and an increase in the slope of D vs Z/r for the REE.

In silicate melts, the LREE are VIII-fold coordinated, gradually decreasing to a VI- and V-fold coordination for the HREE (Ponader & Brown, 1989). The partitioning of Ca is most similar to that of La (Figs 6a, b and 8a); that is, the REE with the most similar ionic potential (but not the same coordination number), underlining the crucial role of ionic potential in the partitioning behaviour.

As discussed above, a positive D^{Eu} anomaly in comparison with the neighbouring D^{Sm} and D^{Gd} is observed in the three experiments that had graphite added, which resulted in a calculated 38% of the Eu being divalent and an almost quantitative reduction of Fe^{2+} to Fe^0 at an oxygen fugacity near IW (Fig. 6a). Its in part divalent character renders Eu more similar to Ca in these experiments and hence more compatible in the carbonatite melt. A lack of a D^{Eu} anomaly in the more oxidizing experiments is consistent with the results of Cicconi *et al.* (2012), who suggested that Eu in the silicate melt is essentially trivalent at $f_{O2} \geq$ QFM.

Strong partitioning of REE into the carbonatite melt ($D^{REE} = 5·8–38·0$) occurs only in hydrous compositions when carbonatites unmix from evolved silica-rich alkaline melts (Figs 6b and 7d). We thus speculate that upon hydrous carbonatite crystallization, the consequent saturation in fluids leads to hydrothermal systems concentrating REE in secondary deposits.

High field strength elements

The high field strength elements Th, Zr, Hf, Ti, U, Nb and Ta have $D < 1$ under anhydrous conditions. Of the HFSE, Hf partitions most strongly into the silicate melt in both the anhydrous ($D^{Hf} = 0·2–0·04$) and H_2O-bearing systems ($D^{Hf} = 0·3–0·04$). We note that the REE and the tetravalent HFSE Th, Zr and Hf form a linear trend in D vs ionic potential space, again suggesting that their partitioning between the carbonatite and silicate melts is mainly governed by ionic potential (Fig. 7).

Nevertheless, the D values of Ti, Nb and Ta form a cluster at higher ionic potential (7·1–7·8 Å^{-1}). When U becomes more oxidized D^U is further away from the linear trend defined above but moves towards the Ti–Ta–Nb cluster (Fig. 7c). Th and U belong to the group of elements in which partitioning is shifted from slightly compatible in the silicate melt to compatible in the carbonatite melt with increasing melt polymerization.

An interesting aspect of carbonatite/silicate melt trace element fractionation are the strong differences in partitioning observed for the geochemical pairs Zr–Hf ($D^{Zr/Hf} = 1·3–2·1$) and Nb–Ta ($D^{Nb/Ta} = 1·6–3·0$; Fig. 10c and d). This degree of fractionation is much higher than for silicate or oxide mineral/silicate melt equilibria for minerals potentially involved in crystal–liquid fractionation or partial melting (e.g. amphibole: Tiepolo *et al.*, 2007; rutile: Schmidt *et al.*, 2004; Klemme *et al.*, 2005; titanite, John *et al.*, 2011) and for two-silicate melt equilibria (Schmidt *et al.*, 2006). The degree of Zr/Hf and Nb/Ta fractionation increases with miscibility gap width, which correlates positively with $D^{Zr/Hf}$, $D^{Nb/Ta}$ and also $D^{La/Lu}$ (Fig. 10c and d). The most likely explanation for the strong relative partitioning of Nb vs Ta and Zr vs Hf is different complexation and/or coordination in the carbonatite melt, a topic that needs further investigation. Similar fractionation of Nb/Ta and Zr/Hf was observed by Veksler *et al.* (1998, 2012), who suggested an increasing role of the electronic structure with increasing Z/r.

Third row transition metals V to Zn

In the anhydrous systems, the transition metals V, Cr, Mn, Fe, Co, Cu and Zn have D <1, except for V and Cu ($D = 0·8–2$) and Mn in experiment LM108. In the H_2O-bearing systems, D values of these transition metals vary between 0·7 and 6, with the highest partition coefficients for Cr and Co. In general, the partitioning behavior of V, Cr, Mn, Fe, Co and Zn is similar to that of calcium

(Fig. 8b and d): the silica-rich systems have the highest partition coefficients (D for LM73 > LM101 > LM83), whereas for the silica-undersaturated system, partitioning decreases in the following order: LM63 > LM75 > LM82. The behavior of Cu is less clear owing to the large errors on the calculated D values. As mentioned above, oxygen fugacity variations between IW and HM do not strongly influence the partitioning behavior of the multi-valent transition metals.

Molybdenum and phosphorus

Molybdenum has the highest partition coefficients ($D^{\mathrm{Mo}} = 3{\cdot}7$–$8{\cdot}7$) and P the second highest ($D^{\mathrm{P}} = 1{\cdot}5$–$3{\cdot}5$; Table 8) in the anhydrous systems. Galoisy *et al.* (2000) showed by EXAFS that the second nearest neighbour of Mo^{6+} in silicate melts is never Si. Mo^{6+} leads to the formation of isolated large clusters with alkali and alkaline earth elements that have no direct connection to the silicate network. Apparently, such a coordination environment renders Mo relatively incompatible with silicate melts and explains its strong preference for the carbonatite melt.

The structural interpretation of silicate–phosphate interaction in silicate melts (Mysen & Cody, 2001) is that isolated PO_4 and P_2O_7 complexes occur together with PO_4 groups linked to the silicate network by 1–4 oxygen bridges. Mysen & Cody (2001) indicated that isolated phosphate complexes are charge balanced with alkali or alkaline earth elements as well as Al-bearing phosphate complexes. Cody *et al.* (2001) concluded that in peralkaline melts, phosphate species become more polymerized and silicate species less polymerized with increasing temperature. An increase in phosphate polymerization leads to self-existing phosphate clusters and chains, which separate from the silicate melt and stabilize in the carbonatite melt.

Network formers

The network formers Si and Al have among the highest preference to partition into the silicate melt ($D^{\mathrm{Si}} = 0{\cdot}03$–$0{\cdot}28$, $D^{\mathrm{Al}} = 0{\cdot}02$–$0{\cdot}20$). They are mostly tetrahedrally coordinated, as are Ge and Ga, which substitute for Si and Al (Fleet *et al.*, 1984). Also, their high ionic potential indicates covalent bonding, underlining again the importance of ionic potential for the partitioning between silicate and carbonatite melts.

CONCLUSIONS AND OUTLOOK

General trends for the different element groups are similar for all anhydrous bulk systems. Alkali and alkaline earth elements partition mostly into the carbonatite melt, leading to alkali contents of carbonatites similar to or higher than those of the conjugate silicate melts. The narrow scattering of the partition coefficients in the anhydrous systems can be explained by comparable widths of the miscibility gaps. Our data compare well with the results of Veksler *et al.* (1998, 2012), obtained at $\leq 0{\cdot}1$ GPa, indicating that pressure has only a minor indirect influence on trace element partitioning and that compositional differences in anhydrous bulk systems have little influence on the miscibility gap width and on partition coefficients.

Except for the alkalis and alkaline earths, partition coefficients for the H_2O-bearing systems have very similar patterns to the anhydrous systems but D values are up to an order of magnitude higher. Addition of H_2O increases the miscibility gap width, resulting in higher partition coefficients. Increased polymerization of the silicate melt leads to a shift of trace element partitioning towards the carbonatite melt, as trace elements become increasingly incompatible with silicate melt polymerization. Therefore, $SiO_2 + Al_2O_3 + H_2O$-rich systems result in a one order of magnitude stronger partitioning in favor of the carbonatite melt than dry, silica-undersaturated ones.

In principle, our partition coefficients can be used to test whether natural magmatic silicate rock–carbonatite pairs represent conjugate melts. Unfortunately, this procedure is not straightforward, as most carbonatites do not represent true melt compositions but are heavily modified during the late or post-magmatic stage and have lost most of their alkalis. A very careful evaluation of the original carbonatite melt composition is necessary. We have applied our data on the kamafugitic silicate melt–carbonatite pairs of the Italian ultrapotassic suite (Martin *et al.*, 2012), demonstrating that the reconstructed carbonatite compositions could be conjugate to certain of the Italian kamafugitic melts.

For all bulk compositions, the systematics of the partitioning behaviour of elements with low to moderate ionic potential can be rationalized, employing ionic potential as a simple measure of bond strength. Elements with high ionic potential seem to be governed by their particular coordination environment.

The high partition coefficients for the REE in the H_2O-bearing polymerized systems indicate that H_2O-rich carbonatites from more evolved alkaline igneous complexes are more prone to form REE deposits than dry ones, as D^{REE} are higher (in favor of carbonatite melts). Furthermore, secondary remobilization and REE concentration could occur through expulsion of magmatic H_2O-bearing fluids upon final crystallization.

As carbonatites may contain substantial amounts of other anionic species (e.g. fluorine or sulfur), systematic studies of carbonatite/silicate melt element partitioning in increasingly complex systems are needed. Furthermore, it would be highly desirable to investigate the structure of alkali-rich carbonatitic liquids in anhydrous and H_2O-bearing systems by *in situ* spectroscopy to understand element partitioning in carbonatite melts.

ACKNOWLEDGEMENTS

We thank K. Hametner for help with the LA-ICP-MS analysis; P. Ulmer, D. Grassi, E. Reusser and J. Connolly for discussion; L. Zehnder for synthesis of the trace element mix; B. Zürcher for maintenance of the centrifuge; W. Malfait for help with Raman spectroscopy. We also thank B. Kjarsgaard, I. Veksler and M. Walter for their thoughtful reviews that helped to improve the paper.

FUNDING

This work was supported by ETH-grant number TH-24 07-03.

SUPPLEMENTARY DATA

Supplementary data for this paper are available at *Journal of Petrology* online.

REFERENCES

Beccaluva, L., Coltorti, M., Di Girolamo, P., Melluso, L., Milani, L., Morra, V. & Siena, F. (2002). Petrogenesis and evolution of Mt. Vulture alkaline volcanism (Southern Italy). *Mineralogy and Petrology* **74**, 277–297.

Berry, A. J., Neill, H. S., Scott, D. R., Foran, G. J. & Shelley, J. M. G. (2006). The effect of composition on Cr^{2+}/Cr^{3+} in silicate melts. *American Mineralogist* **91(11–12)**, 1901–1908.

Bohlen, S. R., Boettcher, A. L., Dollase, W. A. & Essene, E. J. (1980). The effect of manganese on olivine–quartz–orthopyroxene stability. *Earth and Planetary Science Letters* **47(1)**, 11–20.

Bose, K. & Ganguly, J. (1995). Quartz–coesite transition revisited—reversed experimental determination at 500–1200°c and retrieved thermochemical properties. *American Mineralogist* **80(3–4)**, 231–238.

Brey, G. P., Bulatov, V. K., Girnis, A. V. & Lahaye, Y. (2008). Experimental melting of carbonated peridotite at 610 GPa. *Journal of Petrology* **49(4)**, 797–821.

Brey, G. P., Bulatov, V. K. & Girnis, A. V. (2011). Melting of K-rich carbonated peridotite at 6–10 GPa and the stability of K-phases in the upper mantle. *Chemical Geology* **281**, 333–342.

Brooker, R. A. (1998). The effect of CO_2 saturation on immiscibility between silicate and carbonate liquids: an experimental study. *Journal of Petrology* **39(11–12)**, 1905–1915.

Brooker, R. A. & Kjarsgaard, B. A. (2011). Silicate–carbonate liquid immiscibility and phase relations in the system SiO_2–Na_2O–Al_2O_3–CaO–CO_2 at 0·1–2·5 GPa with applications to carbonatite genesis. *Journal of Petrology* **52(7–8)**, 1281–1305.

Brooker, R. A., Kohn, S. C., Holloway, J. R. & McMillan, P. F. (2001). Structural controls on the solubility of CO_2 in silicate melts. Part I: bulk solubility data. *Chemical Geology* **174(1–3)**, 225–239.

Cicconi, M. R., Giuli, G., Paris, E., Ertel-Ingrisch, W., Ulmer, P. & Dingwell, D. B. (2012). Europium oxidation state and local structure in silicate glasses. *American Mineralogist* **97(5–6)**, 918–929.

Clague, D. A. & Frey, F. A. (1982). Petrology and trace-element geochemistry of the Honolulu Volcanics, Oahu—implications for the oceanic mantle below Hawaii. *Journal of Petrology* **23(3)**, 447–504.

Cody, G. D., Mysen, B., Saghi-Szabo, G. & Tossell, J. A. (2001). Silicate–phosphate interactions in silicate glasses and melts: I. A multinuclear (Al-27, Si-29, P-31) MAS NMR and *ab initio* chemical shielding (P-31) study of phosphorus speciation in silicate glasses. *Geochimica et Cosmochimica Acta* **65(14)**, 2395–2411.

D'Orazio, M., Innocenti, F., Tonarini, S. & Doglioni, C. (2007). Carbonatites in a subduction system: The Pleistocene alvikites from Mt. Vulture (southern Italy). *Lithos* **98**, 313–334.

Dalton, J. A. & Wood, B. J. (1993). The compositions of primary carbonate melts and their evolution through wallrock reaction in the mantle. *Earth and Planetary Science Letters* **119(4)**, 511–525.

Dasgupta, R., Hirschmann, M. M. & Stalker, K. (2006). Immiscible transition from carbonate-rich to silicate-rich melts in the 3 GPa melting interval of eclogite plus CO_2 and genesis of silica-undersaturated ocean island lavas. *Journal of Petrology* **47(4)**, 647–671.

Dasgupta, R., Hirschmann, M. M., McDonough, W. F., Spiegelman, M. & Withers, A. C. (2009). Trace element partitioning between garnet lherzolite and carbonatite at 6·6 and 8·6 GPa with applications to the geochemistry of the mantle and of mantle-derived melts. *Chemical Geology* **262(1–2)**, 57–77.

Falloon, T. J. & Green, D. H. (1989). The solidus of carbonated, fertile peridotite. *Earth and Planetary Science Letters* **94(3–4)**, 364–370.

Fleet, M. E., Herzberg, C. T., Henderson, G. S., Crozier, E. D., Osborne, M. D. & Scarfe, C. M. (1984). Coordination of Fe, Ga and Ge in high-pressure glasses by Mössbauer, Raman and X-ray absorption-spectroscopy, and geological implications. *Geochimica et Cosmochimica Acta* **48(7)**, 1455–1466.

Freestone, I. C. & Hamilton, D. L. (1980). The role of liquid immiscibility in the genesis of carbonatites—an experimental-study. *Contributions to Mineralogy and Petrology* **73(2)**, 105–117.

Galoisy, L., Cormier, L., Rossano, S., Ramos, A., Calas, G., Gaskell, P. & Le Grand, M. (2000). Cationic ordering in oxide glasses: the example of transition elements. *Mineralogical Magazine* **64(3)**, 409–424.

Genge, M. J., Jones, A. P. & Price, G. D. (1995). An infrared and Raman-study of carbonate glasses—implications for the structure of carbonatite magmas. *Geochimica et Cosmochimica Acta* **59(5)**, 927–937.

Grassi, D. & Schmidt, M. W. (2011*a*). Melting of carbonated pelites at 8–13 GPa: generating K-rich carbonatites for mantle metasomatism. *Contributions to Mineralogy and Petrology* **162(1)**, 169–191.

Grassi, D. & Schmidt, M. W. (2011*b*). The melting of carbonated pelites from 70 to 700 km depth. *Journal of Petrology* **52(4)**, 765–789.

Guzmics, T., Mitchell, R. H., Berkesi, M. & Szabo, C. (2009). Carbonatite melt inclusions in coexisting magnetite, apatite and monticellite from Kerimasi carbonatite, Tanzania. *Geochimica et Cosmochimica Acta* **73(13)**, A483–A483.

Guzmics, T., Mitchell, R. H., Szabo, C., Berkesi, M., Milke, R. & Ratter, K. (2012). Liquid immiscibility between silicate, carbonate and sulfide melts in melt inclusions hosted in co-precipitated minerals from Kerimasi volcano (Tanzania): evolution of carbonated nephelinitic magma. *Contributions to Mineralogy and Petrology* **164**, 101–122.

Hamilton, D. L., Freestone, I. C., Dawson, J. B. & Donaldson, C. H. (1979). Origin of carbonatites by liquid immiscibility. *Nature* **279(5708)**, 52–54.

Hamilton, D. L., Bedson, P. & Esson, J. (1989). The behaviour of trace elements in the evolution of carbonatites. In: Bell, K. (ed.) *Carbonatites: Genesis and Evolution*. London: Unwin Hyman, pp. 405–427.

Hammouda, T., Moine, B. N., Devidal, J. L. & Vincent, C. (2009). Trace element partitioning during partial melting of carbonated eclogites. *Physics of the Earth and Planetary Interiors* **174(1–4)**, 60–69.

Harmer, R. E. & Gittins, J. (1998). The case for primary, mantle-derived carbonatite magma. *Journal of Petrology* **39(11–12)**, 1895–1903.

Huang, W. L. & Wyllie, P. J. (1974). Liquidus relationships between carbonates and silicates in parts of system CaO–MgO–SiO$_2$–CO$_2$–H$_2$O at 30 Kb. *Transactions of the American Geophysical Union* **55(4)**, 479–480.

Hudon, P. & Baker, D. R. (2002). The nature of phase separation in binary oxide melts and glasses. I. Silicate systems. *Journal of Non-Crystalline Solids* **303(3)**, 299–345.

Huheey, E. A. & Keiter, R. L. (1993). *Inorganic Chemistry: Principles of Structure and Reactivity.* New York: Harper Collins.

John, T., Klemd, R., Klemme, S., Pfaender, J. A., Hoffmann, J. E. & Gao, J. (2011). Nb–Ta fractionation by partial melting at the titanite–rutile transition. *Contributions to Mineralogy and Petrology* **161(1)**, 35–45.

Jones, J. H., Walker, D., Pickett, D. A., Murrell, M. T. & Beattie, P. (1995). Experimental investigations of the partitioning of Nb, Mo, Ba, Ce, Pb, Ra, Th, Pa, and U between immiscible carbonate and silicate liquids. *Geochimica et Cosmochimica Acta* **59(7)**, 1307–1320.

Karner, J. M., Papike, J. J., Sutton, S. R., Shearer, C. K., Burger, P., McKay, G. & Le, L. (2008). Valence state partitioning of V between pyroxene–melt: Effects of pyroxene and melt composition, and direct determination of V valence states by XANES. Application to Martian basalt QUE 94201 composition. *Meteoritics and Planetary Science* **43(8)**, 1275–1285.

Kjarsgaard, B. & Peterson, T. (1991). Nephelinite–carbonatite liquid immiscibility at Shombole volcano, East Africa—petrographic and experimental evidence. *Mineralogy and Petrology* **43**, 293–314.

Kjarsgaard, B. A., Hamilton, D. L. & Peterson, T. D. (1995). Peralkaline nephelinite/carbonatite liquid immiscibility: comparison of phase compositions in experiments and natural lavas from Oldoinyo Lengai. In: Bell, K. & Keller, J. (eds) *Carbonatite Volcanism. Oldoinyo Lengai and Petrogenesis of Natrocarbonatites*. Berlin: Springer, pp. 163–190.

Klemme, S., Prowatke, S., Hametner, K. & Gunther, D. (2005). Partitioning of trace elements between rutile and silicate melts: Implications for subduction zones. *Geochimica et Cosmochimica Acta* **69**, 2361–2371.

Kress, V. C. & Carmichael, I. S. E. (1991). The compressibility of silicate liquids containing Fe$_2$O$_3$ and the effect of composition, temperature, oxygen fugacity and pressure on their redox states. *Contributions to Mineralogy and Petrology* **108(1–2)**, 82–92.

Lee, W. J. & Wyllie, P. J. (1997). Liquid immiscibility between nephelinite and carbonatite from 1·0 to 2·5 GPa compared with mantle melt compositions. *Contributions to Mineralogy and Petrology* **127(1–2)**, 1–16.

Longerich, H. P., Jackson, S. E. & Gunther, D. (1996). Laser ablation inductively coupled plasma mass spectrometric transient signal data acquisition and analyte concentration calculation. *Journal of Analytical Atomic Spectrometry* **11(9)**, 899–904.

Martin, L. H. J., Schmidt, M. W., Mattsson, H. B., Ulmer, P., Hametner, K. & Guenther, D. (2012). Element partitioning between immiscible carbonatite–kamafugite melts with application to the Italian ultrapotassic suite. *Chemical Geology* **320–321**, 96–112.

Mourão, C., Mata, J., Doucelance, R., Madeira, J., da Silveira, A. B., Silva, L. C. & Moreira, M. (2010). Quaternary extrusive calciocarbonatite volcanism on Brava Island (Cape Verde): A nephelinite–carbonatite immiscibility product. *Journal of African Earth Sciences* **56(2–3)**, 59–74.

Mysen, B. O. & Cody, G. D. (2001). Silicate–phosphate interactions in silicate glasses and melts: II. Quantitative, high-temperature structure of P-bearing alkali aluminosilicate melts. *Geochimica et Cosmochimica Acta* **65(14)**, 2413–2431.

Nielsen, T. F. D. & Veksler, I. V. (2002). Is natrocarbonatite a cognate fluid condensate? *Contributions to Mineralogy and Petrology* **142(4)**, 425–435.

Novella, D. & Keshav, S. (2010). Silicate melt–carbonatite liquid immiscibility reconsidered in the system CaO–MgO–Al$_2$O$_3$ at 2–3 GPa. In: *EMPG XIII, Toulouse, Conference Abstracts*.

O'Neill, H. S. C. & Eggins, S. M. (2002). The effect of melt composition on trace element partitioning: an experimental investigation of the activity coefficients of FeO, NiO, CoO, MoO$_2$ and MoO$_3$ in silicate melts. *Chemical Geology* **186(1–2)**, 151–181.

Papale, P., Moretti, R. & Barbato, D. (2006). The compositional dependence of the saturation surface of H$_2$O + CO$_2$ fluids in silicate melts. *Chemical Geology* **229(1–3)**, 78–95.

Peccerillo, A. (2005). *Plio-Quaternary Volcanism in Italy.* Heidelberg: Springer, 365 p.

Ponader, C. W. & Brown, G. E. (1989). Rare-earth elements in silicate glass melt systems. 1. Effects of composition on the coordination environments of La, Gd, and Yb. *Geochimica et Cosmochimica Acta* **53(11)**, 2893–2903.

Roedder, E. (1978). Silicate liquid immiscibility in magmas and in the system K$_2$O-FeO-Al$_2$O$_3$-SiO$_2$: An example of serendipity. *Geochimica et Cosmochimica Acta* **42**, 1597–1617.

Rosatelli, G., Wall, F., Stoppa, F. & Brilli, M. (2010). Geochemical distinctions between igneous carbonate, calcite cements, and limestone xenoliths (Polino carbonatite, Italy): spatially resolved LAICPMS analyses. *Contributions to Mineralogy and Petrology* **160(5)**, 645–661.

Schmidt, M. W., Dardon, A., Chazot, G. & Vannucci, R. (2004). The dependence of Nb and Ta rutile–melt partitioning on melt composition and Nb/Ta fractionation during subduction processes. *Earth and Planetary Science Letters* **226**, 415–432.

Schmidt, M. W., Connolly, J. A. D., Gunther, D. & Bogaerts, M. (2006). Element partitioning: The role of melt structure and composition. *Science* **312(5780)**, 1646–1650.

Schreiber, H. D. (1983). The chemistry of uranium in glass-forming aluminosilicate melts. *Journal of the Less-Common Metals* **91(1)**, 129–147.

Sen, S. & Yu, P. (2005). Observation of a stuffed unmodified network in beryllium silicate glasses with multinuclear NMR spectroscopy. *Physical Review B* **72(13)**, 132203-1–4.

Sen, S., Yu, P., Klyuev, V. P. & Pevzner, B. Z. (2008). Atomic structure of beryllium boroaluminate glasses: A multi-nuclear NMR spectroscopic study. *Journal of Non-Crystalline Solids* **354(33)**, 4005–4011.

Shannon, R. D. (1976). Revised effective ionic-radii and systematic studies of interatomic distances in halides and chalcogenides. *Acta Crystallographica Section A* **32(SEP1)**, 751–767.

Stoppa, F. & Cundari, A. (1998). Origin and multiple crystallization of the kamafugite–carbonatite association: the San Venanzo Pian di Celle occurrence (Umbria, Italy). *Mineralogical Magazine* **62(2)**, 273–289.

Stoppa, F. & Prinicipe, C. (1997). Eruption style and petrology of a new carbonatitic suite from the Mt. Vulture (Southern Italy): The Monticchio lake formation. *Journal of volcanology and geothermal research* **80(1–2)**, 251–265.

Thomsen, T. B. & Schmidt, M. W. (2008). Melting of carbonated pelites at 2·5–5·0 GPa, silicate–carbonatite liquid immiscibility, and potassium–carbon metasomatism of the mantle. *Earth and Planetary Science Letters* **267(1–2)**, 17–31.

Tiepolo, M., Oberti, R. & Zanetti, A. (2007). Trace-element partitioning between amphibole and silicate melt. In: Hawthorne, F. C., Oberti, R., Della Ventura, G. & Mottana, A. (eds) *Amphiboles: crystal chemistry, occurence, and health issues.* Mineralogical Society of

America and Geochemical Society, Reviews in Mineralogy and Geochemistry **67**, 417–452.

Treiman, A. H. (1989). Carbonatite magma: properties and processes. In: Bell, K. (ed.) *Carbonatites: Genesis and Evolution*. London: Unwin & Hyman, pp. 89–104.

Ulmer, P. & Sweeney, R. J. (2002). Generation and differentiation of group II kimberlites: Constraints from a high-pressure experimental study to 10 GPa. *Geochimica et Cosmochimica Acta* **66(12)**, 2139–2153.

Veksler, I. V. (2004). Liquid immiscibility and its role at the magmatic–hydrothermal transition: a summary of experimental studies. *Chemical Geology* **210(1–4)**, 7–31.

Veksler, I. V., Petibon, C., Jenner, G. A., Dorfman, A. M. & Dingwell, D. B. (1998). Trace element partitioning in immiscible silicate–carbonate liquid systems: An initial experimental study using a centrifuge autoclave. *Journal of Petrology* **39(11–12)**, 2095–2104.

Veksler, I. V., Dorfman, A. M., Danyushevsky, L. V., Jakobsen, J. K. & Dingwell, D. B. (2006). Immiscible silicate liquid partition coefficients: implications for crystal–melt element partitioning and basalt petrogenesis. *Contributions to Mineralogy and Petrology* **152(6)**, 685–702.

Veksler, I. V., Dorfman, A. M., Dulski, P., Kamenetsky, V. S., Danyushevsky, L. V., Jeffries, T. & Dingwell, D. B. (2012). Partitioning of elements between silicate melt and immiscible fluoride, chloride, carbonate, phosphate and sulfate melts, with implications to the origin of natrocarbonatite. *Geochimica et Cosmochimica Acta* **79**, 20–40.

Wallace, M. E. & Green, D. H. (1988). An experimental determination of primary carbonatite magma composition. *Nature* **335(6188)**, 343–346.

Watkinson, D. H. & Wyllie, P. J. (1971). Experimental study of composition join $NaAlSiO_4$-$CaCO_3$-H_2O and genesis of alkali rock-carbonatite complexes. *Journal of Petrology* **12(2)**, 357–378.

Wendlandt, R. F. & Harrison, W. J. (1979). Rare-earth partitioning between immiscible carbonate and silicate liquids and CO_2 vapor—results and implications for the formation of light rare earth-enriched rocks. *Contributions to Mineralogy and Petrology* **69(4)**, 409–419.

Williams, Q. & Knittle, E. (2003). Structural complexity in carbonatite liquid at high pressures. *Geophysical Research Letters* **30(1)**, doi:10.1029/2001GL013876.

Woolley, A. R. & Kjarsgaard, B. A. (2008). *Carbonatite Occurrences of the World: Map and Database*. Geological Survey of Canada.